

INFLUENCE OF INERT GASES ON HEAT AND MASS TRANSFER IN
NEXT-GENERATION NUCLEAR REACTORS

A Dissertation
presented to
the Faculty of the Graduate School
at the University of Missouri

In Partial Fulfillment
of the Requirements for the Degree
Doctor of Philosophy

by
ABU RAFI MOHAMMAD IASIR
Dr. Karl Hammond, Dissertation Supervisor
MAY 2021

© Copyright by Abu Rafi Mohammad Iasir 2021

All Rights Reserved

The undersigned, appointed by the dean of the Graduate School, have examined
the dissertation entitled

INFLUENCE OF INERT GASES ON HEAT AND MASS TRANSFER IN
NEXT-GENERATION NUCLEAR REACTORS

presented by Abu Rafi Mohammad Iasir,
a candidate for the degree of Doctor of Philosophy,
and hereby certify that, in their opinion, it is worthy of acceptance.

Professor Karl Hammond, chair

Professor Scott Kovaleski, member

Professor Robert Winholtz, member

Professor Nickie Peters, member

To my parents Ismail and Halima

*"Do you think that I know what I am doing?
That for one breath or half-breath I belong to myself?
As much as a pen knows what it's writing,
Or the ball can guess where it's going next."*

—Rumi

ACKNOWLEDGMENTS

It is my pleasure to thank my supervisor, Dr. Karl Hammond, whose expertise was invaluable in this research. His guidance and assistance throughout my PhD helped me to grow as a researcher. My sincere thanks to my PhD committee, Dr. Scott Kovaleski, Dr. Robert Winholtz, and Dr. Nickie Peters.

I am very grateful to a few wonderful people with whom I shared our lab: Amir Mofrad, Andrea Saltos, Brandon Laufer, Luke Kruse, Jiasen Guo, and Zhuocen Yang. I know I learned more from these people than I will ever realize. Their patience, insight, and, most importantly, camaraderie and humor helped to make the long days and challenging time more enjoyable. I'd also like to thank Dr. Mosa, Dr. Sadia Akhtar, Tahmid Hasan and Shawmy Khan for their generosity and help. Many thanks to my friends David Winjum, Saumil Dharia, Rachel Dickie, Payel Sen, and Murat Yildirm. We have lived through a very interesting time and shared so many memories. Special thanks to Joe Strnad and his family. My life at Mizzou would be a very different one without them.

Finally, my sincere gratitude to my family for their continuous love and support. I am grateful to my sisters Sadia, Tahera, Ayesha and my brother Javed. You remind me to appreciate life and the value of family. Over the last seven years, I've missed many family events, but you've found a way to include me every time from eight thousand miles away. Last, but most important, my mother, Halima, and my father, Ismail, who always knew when to call me and tell me right the thing. Their unwavering love, pride, and motivation have shaped who I am today.

TABLE OF CONTENTS

ACKNOWLEDGMENTS	ii
LIST OF TABLES	vi
LIST OF FIGURES	viii
LIST OF SYMBOLS	xi
ABSTRACT	xiii
Chapter	
1. INTRODUCTION	1
1.1 Metallic Uranium and Alloys	3
1.2 Fission Gas	8
References	9
2. BACKGROUND	13
2.1 Electronic Structure Calculations	13
2.1.1 The Many-Body Hamiltonian	13
2.1.2 Hartree–Fock Approach	17
2.1.3 Density Functional Theory	20
2.1.4 Kohn–Sham Equations	24
2.1.5 Kohn–Sham Problem for an Isolated Atom	25
2.1.6 Pseudopotentials	27
2.1.7 Basic Phillips–Kleinman Construction	27
2.1.8 Norm-Conserving Pseudopotentials	31
2.1.9 Ultrasoft Pseudopotentials (US)	32
2.1.10 Projector Augmented Wave Method (PAW)	32
References	34

3. ESTIMATION OF EFFECTIVE THERMAL CONDUCTIVITY IN U-10Mo FUELS WITH DISTRIBUTED XENON GAS BUBBLES	35
3.1 Introduction.....	35
3.2 Methods	39
3.2.1 Effective Thermal Conductivity Calculation	44
3.3 Results and Discussion	44
3.3.1 Effect of Xenon Gas Bubbles on the Thermal Conductivity	44
3.3.2 Effect of Xenon Pressure on the Overall Thermal Conductivity	49
3.3.3 Effect of Bubble Arrangement on Thermal Conductivity.....	49
3.4 Conclusions	54
References	56
4. PSEUDOPOTENTIAL FOR PLANE-WAVE DENSITY FUNCTIONAL THEORY STUDIES OF METALLIC URANIUM	60
4.1 Introduction.....	60
4.2 Computational Details	63
4.3 Results.....	65
4.3.1 α -Uranium.....	65
4.3.2 γ -U: Crystal Structure and Elastic Moduli	70
4.3.3 Body-Centered Tetragonal Uranium	72
4.3.4 Face-Centered Cubic Uranium	73
4.3.5 Electronic Density of States	76
4.4 Conclusion	76
Appendix: Elastic Parameter Calculation of α -uranium	79
Appendix: Elastic Parameter Calculation for γ -uranium.....	85
References	89
5. XENON MOBILITY IN BCC-URANIUM AND URANIUM-MOLYBDENUM ALLOYS.....	92
5.1 Introduction.....	92
5.2 Theory	95
5.3 Methodology	98
5.4 Results and Discussion	99

5.4.1	Vacancy Formation and Impurity–Vacancy Binding Energies	99
5.4.2	Xenon and Molybdenum Diffusion	101
5.5	Conclusions	106
	References	107
6.	HELIUM IMPURITIES AND INTERACTION WITH LITHIUM	113
6.1	Introduction	113
6.2	Methodology	114
6.3	Results and Discussion	115
	References	123
7.	CONCLUSIONS AND FUTURE WORK	126
 Appendix		
A.	ATOMIC UNITS	130
B.	ORTHOGONAL PLANE WAVE	133
C.	PROJECTOR AUGMENTED WAVE	137
D.	FINITE ELEMENT METHOD IN MOOSE	143
E.	INPUT FILES	145
BIBLIOGRAPHY		169
VITA		186

LIST OF TABLES

Table	Page
4.1 Parameters used to generate the pseudopotential in atompaw	65
4.2 Ground-state properties and elastic moduli of α -uranium from present work, compared with the PAW pseudopotential calculations of Beeler	69
4.3 Equilibrium lattice parameters, volume per atom, and elastic moduli of γ -uranium.	71
4.4 The optimized lattice parameters (\AA), volume per atom (\AA^3) and elastic moduli of bct uranium.	72
4.5 The equilibrium lattice parameter, volume per atom, and elastic moduli of fcc uranium.	73
5.1 Probability of having different numbers of molybdenum atoms in the nearest-neighbor (NN) location for a bcc uranium–molybdenum alloy.	98
5.2 Vacancy formation energy (eV) of γ -uranium compared with previously-published results.	100
5.3 Solute–vacancy binding energies in γ -uranium for various solutes near a vacancy	101
5.4 Xenon migration energy (E_m) for different configurations.	102
6.1 Calculated vacancy formation energy E_f^\square , vacancy migration energy E_m^\square , and various split-dumbbell and self-interstitial formation energies in lithium	117
6.2 Formation energies (E_f), binding energies (E_b), and migration energies (E_m , all in eV) for helium located at octahedral or tetrahedral interstitial sites as well as substitutional sites	118

6.3 Formation energies (E_f) of He–He split dumbbells bound to a vacancy.....	118
6.4 Binding energy of n helium atoms to a vacancy.	121

LIST OF FIGURES

Figure	Page
1.1 Orthorhombic crystal structure of α -uranium.	4
1.2 Uranium–aluminum phase diagram	5
1.3 Uranium–molybdenum phase diagram	6
2.1 Schematic representation of the self-consistent loop solution of Kohn–Sham equations.	26
2.2 Radial distribution function of hydrogenic 1s, 2s, and 3s, electrons	28
2.3 Schematic of the replacement of the all-electron wavefunction and core potentials by a pseudo-wavefunction and pseudopotential.	28
3.1 (a) Discretized domain of intra-granular xenon bubbles inside a U-10Mo matrix; (b) Example two-dimensional bubble distribution used for intra-granular xenon gas, consisting of bubbles with 3.1, 3.6, 3.75, and 4.0 nm diameters, consistent with the work of Miller and coworkers	40
3.2 (a) SEM image of the fission gas bubbles along the grain boundaries from Miller used for FEM calculations (b) Geometry created based on the grain boundary fission gas image in (a) (c) FEM mesh with grain boundary fission gas of the region between the dotted line in (b).	41
3.3 (a) Thermal conductivity of xenon as a function of pressure and temperature based on the measurements of Rabinovich et al.	42
3.4 Comparison between the thermal conductivity of U-10Mo (from Kaufmann) to the effective thermal conductivity of U-10Mo with intra-granular xenon bubbles of different diameters as arranged in Figure 3.1b.	45

3.5 Comparison of the calculated effective thermal conductivity of U-10Mo with intra-granular xenon bubble (radius 1.55 nm, 10% porosity) with the Maxwell–Eucken and Hashin–Shtrikman models	47
3.6 Comparison between the thermal conductivity of bubble-free U-10Mo with that of U-10Mo that has xenon bubbles decorating the grain boundaries according to the distribution in Figure 3.2	48
3.7 Overall thermal conductivity of U-10Mo using the thermal conductivity of xenon at two extremes of pressure (1 bar and 1000 bar), compared to that of pure (bubble-free) U-10Mo	50
3.8 Different bubble arrangements in which the area of each bubble and the number of bubbles are the same	51
3.9 Comparison of the calculated thermal conductivity of different bubble arrangements (constant bubble area and diameter corresponding to Fig. 3.8).	52
3.10 Different bubble arrangements where the area is the same but the bubbles have different diameters. (a) 20 bubbles, (b) 25 bubbles, (c) 32 bubbles, (d) 38 bubbles.	53
3.11 Comparison of thermal conductivity between different bubble diameters at constant total bubble area with bubble-free U-10Mo. Bubble arrangements are shown in Figure 3.10	54
4.1 Energy vs. volume curve for three different phases of uranium.....	66
4.2 (a) Calculated total energy as a function of volume for α -uranium. (b) Calculated total energy as a function of the positional parameter y for α -uranium.	68
4.3 Total electronic densities of states of α , γ , bct, and fcc uranium near the Fermi level.	74
4.4 The partial electronic densities of states of α , γ , bct, and fcc uranium near the Fermi level.	75
4.5 Changes in the strain energy as a function of strain using distortion matrix D_1 (4.3), D_2 (4.4), and D_3 (4.5).	82

4.6 Changes in the strain energy as a function of strain using distortion matrix D_4 (4.7), D_5 (4.8), and D_6 (4.9).....	83
4.7 Changes in the strain energy as a function of strain using distortion matrix D_7 (4.11), D_8 (4.12), and D_9 (4.13).	84
4.8 Energy as a function of lattice parameter for γ -uranium	86
4.9 Changes in the strain energy as a function of strain (δ) for monoclinic distortions of γ -uranium	87
4.10 Changes in the strain energy as a function of strain (δ) for orthorhombic distortions of γ -uranium	88
5.1 Diagram of a xenon jump from the center site to a nearest-neighbor vacancy in γ -uranium.	104
5.2 The three sets of symmetrically-inequivalent hops of xenon from the center with two molybdenum atoms in the nearest-neighbor shell.....	104
5.3 The three sets of symmetrically-distinct hops from the center site with three molybdenum atoms in the nearest-neighbor shell	105
6.1 Helium–helium dumbbells in different orientations in the bcc lithium unit cell.	116
6.2 Tetrahedral (○) and octahedral (□) sites in a bcc crystal	120
6.3 Binding energy of n helium atoms to a vacancy for $n \in [1, 8]$	121

LIST OF SYMBOLS

ℓ	azimuthal quantum number
λ	the effective thermal conductivity of the fuel
\mathcal{H}	many-body Hamiltonian
Ψ	wavefunction
ψ_{AE}	all-electron wavefunction
ψ_{ps}	pseudo-wavefunction
v^{EX}	exchange potential
\mathbf{R}_a	position of a^{th} nucleus
\mathbf{r}_j	position of j^{th} electron
D	diffusion coefficient
D_0	pre-exponential factor for diffusion coefficient
$E_{\text{U}_{N-1}}^{\square_1}$	energy of a system with a vacancy
E_f^{\square}	vacancy formation energy
$E_{\text{U}_{N-2}}^{X_1 \square_1}$	energy of a system with a solute and a adjacent vacancy
$E_{\text{U}_{N-1}}^{X_1}$	energy of a system with a solute
E_b	binding energy
$E_b^{X-\square}$	binding energy of a solute to a vacancy
$E_f^{\text{He}-\square-\text{He}}$	helium–helium dumbbell formation energy around a vacancy
E_f^{oct}	helium formation energy in a octahedral position
E_f^{subs}	helium formation energy in a substitutional position
E_f^{tetr}	helium formation energy in a tetrahedral position

E_m	migration energy
E_{U_N}	energy of a system of N uranium atoms
$E_{\text{Heisolated}}$	energy of an isolated helium atom
E_{xc}	exchange-correlation energy
K	thermal conductivity
m	spin quantum number
m_e	mass of a single electron
M_i	molar mass
N	number of atoms in a supercell
N	number of electrons
n	principle quantum number
P_I	momentum of the I^{th} nucleus
Q_{IS}	vibrational partition function of the initial state
Q_{TS}	vibrational partition function of transition state
r_{core}	core radius
r_{PAW}	augmentation radius
r_{shape}	shape function cutoff
V_{ext}	external potential
x_i	mole fraction
x_{Mo}	mole fraction of molybdenum
x_{Xe}	mole fraction of xenon
Z_a	charge of a^{th} nucleus

INFLUENCE OF INERT GASES ON HEAT AND MASS TRANSFER IN NEXT-GENERATION NUCLEAR REACTORS

Abu Rafi Mohammad Iasir

Dr. Karl Hammond, Dissertation Supervisor

ABSTRACT

Inert gases cause some unique challenges in nuclear fuel development. In this dissertation, we study the impact of inert gases on the transport behavior in next-generation fission and fusion reactors. Uranium–molybdenum alloys are potential nuclear fuels that can replace highly-enriched uranium fuel in research and test reactors around the world. Developing a uranium fuel with low enrichment is an important step towards preventing nuclear proliferation and promoting the peaceful use of nuclear energy. We look into how fission gas (*i.e.*, krypton and xenon) impacts the transport properties of U–Mo alloys. We start with an analysis of the impact of fission gas on the overall thermal conductivity of U–Mo. We find that the presence of fission gas inside the fuel significantly reduces the overall thermal conductivity. We then discuss the electronic structure of uranium using density functional theory (DFT) and introduce a new pseudopotential for uranium. This pseudopotential is then used to examine xenon migration in U–Mo alloys. Our results show that the presence of molybdenum in nearest-neighbor lattice positions increases the migration energy of xenon relative to pure γ -uranium, meaning molybdenum impedes fission gas transport. Finally, we study the interaction of helium with lithium, which is a potential plasma-facing material for fusion reactors, using DFT. We find that helium behaves very differently in lithium than it does in other bcc materials. Our studies show that helium has very low migration energies inside lithium, indicating high mobility.

CHAPTER 1

INTRODUCTION

Since the discovery of fission in 1938, the world has experienced the impact of nuclear power on modern society. The primary fuel for fission is ^{235}U . Naturally-occurring uranium consists of a combination of different isotopes: about 99.3% ^{238}U (wt%), 0.7% ^{235}U , and trace amounts of ^{234}U . Uranium can be “enriched” in the ^{235}U isotope by using various complicated processes that mainly use the difference in mass and other physical properties. A typical power generating reactor requires less than 5% uranium enrichment. Research reactors which require higher neutron fluxes, need a higher percentage of uranium enrichment. The neutron produced by a research reactor can be used for neutron scattering, testing and analysis of materials, production of radioisotopes, and training. Research and test reactors are also referred as non-power reactors. The enrichment, or weight fraction of ^{235}U , specifies the key factors of any uranium content, both in terms of research reactor fuel performance and in nuclear weapons. Above a certain enrichment, the fissile material can be turned into explosive devices. As a result, low-enriched uranium (LEU) and high-enriched uranium (HEU) have been introduced. Historically, this limit has been set at an enrichment of 20% [1, 2].

Using HEU in research reactors leads to a series of unavoidable and apparent proliferation¹ risks that are related to diversion and theft of the fissile material [4]. HEU can be used to make nuclear explosives, such as the one used on Hiroshima

¹“proliferation” in the context of nuclear energy is defined as “the spread of nuclear weapons and technologies and the materials to make them” [3].

by the United States in World War II. That weapon, code named “Little Boy,” contained about 50 kilograms of ^{235}U with an average enrichment of about 80% [5]. The neutron production in 60 kg of metallic enriched uranium (from both fission and (α, n) reactions on oxygen) is about 100 per second. This production rate and combined with a neutron reflector can be made into a highly-enriched uranium weapon. Although there is disagreement about the likelihood of a rogue nation acquiring the necessary technical capabilities to make a nuclear weapon with an implosion design, there is little argument that it is much easier to design a so-called gun-type weapon that could work without being tested.

Proliferation concerns about HEU resulted in a global effort, led by the USA, to eliminate civilian uses of HEU in research and test reactors. One of the important HEU reduction programs is known as the Reduced Enrichment for Research and Test Reactors (RERTR) program. The RERTR program was initiated in the USA in the late 1970s to develop new nuclear fuels to replace high-enriched uranium (HEU) [6, 7]. The RERTR program is now managed by the U. S. National Nuclear Security Administration’s (NNSA) Office of Material Management and Minimization [8]. The development of low-enrichment uranium (LEU) fuels for high-performance reactors is an important nonproliferation initiative.

The RERTR initiative has completed a total of 69 reactor conversions to use LEU fuel, and 26 HEU-based reactor facilities have been verified to have been shut down [9]. The conversion of six domestic high-performance research reactors² that still use high-enriched uranium fuel is yet to be achieved. Due to their unique operating conditions, converting these six reactors will not be easy, and a plethora of nuclear engineering challenges are associated with their conversion. These

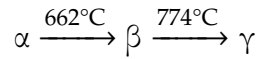
²The Advance Test Reactor (ATR) at Idaho National Laboratory (INL), Idaho; the Advanced Test Reactor Critical (ATRC) Assembly at INL, Idaho; the High Flux Isotope Reactor (HFIR) at Oak Ridge National Laboratory (ORNL), Tennessee; the Massachusetts Institute of Technology Reactor (MITR), Massachusetts; the National Bureau of Standards Reactor (NBSR) in Gaithersburg, Maryland; and the University of Missouri Research Reactor (MURR) in Columbia, Missouri.

conversion processes may take longer time periods, but developing a new LEU fuel is essential to ensure better performance and while limiting nuclear proliferation. The timeline for the conversion is currently estimated to be 10–16 years [10–12].

Research reactors operate at relatively low peak fuel temperatures, but they are required to meet fuel performance requirements at high burnup. A typical peak fuel centerline temperature in a research reactor is around 250°C [13]. For a research reactor, fission densities are usually in the range of 3×10^{21} to 6×10^{21} fissions/cm³. In some cases, peak fuel fission density exceeds 7×10^{21} fissions/cm³, requiring a higher density of ²³⁵U atoms. Consequently, one of the main requirements of LEU fuels is increased uranium density, such as that found in metallic uranium, to offset the decrease in ²³⁵U enrichment.

1.1 Metallic Uranium and Alloys

Uranium, an actinide, has three allotropic forms at atmospheric pressure:



The orthorhombic (α -phase), stable from below room temperature to 662°C; tetragonal (β -phase), stable from 662 to 774°C; and body-centered cubic (γ -phase), stable from 772°C to the melting point, 1132 °C [12]. Metallic uranium at standard temperature is thought to have sufficient density (19.05 ± 0.02 g/cm³). α -Uranium belongs to the orthorhombic system, in which the three axes are mutually perpendicular ($\mathbf{a} \perp \mathbf{b} \perp \mathbf{c}$) but are unequal length ($a \neq b \neq c$) (Fig. 1.1). This orientation of crystal is considered *anisotropic*. A great deal of work has gone into studying the properties of α -uranium. Different heat treatment, corrosion, grain size analysis, mechanical and elastic property studies, and post irradiation analysis indicate that α -uranium is a poor candidate to be considered as a nuclear fuel [14–16].

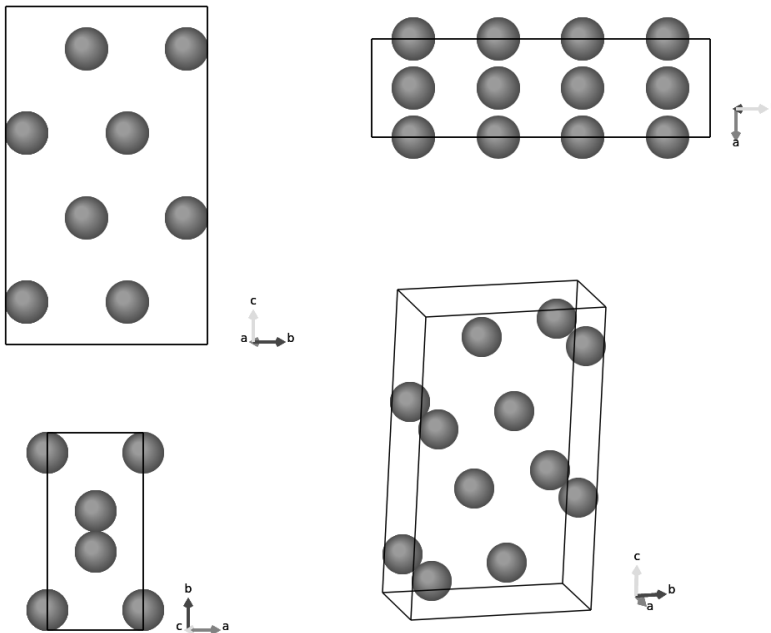


Figure 1.1. Orthorhombic crystal structure of α -uranium.

Alloying uranium to obtain certain properties was extensively studied in the early stages of nuclear fuel development. Some of the reasons were (1) to achieve a finer grain size, (2) to improve mechanical properties, (3) to improve corrosion resistance, and (4) to increase irradiation performance. Aluminum is the material of choice for many components of low-temperature research reactors. The irradiation behavior of aluminum at low temperature ($< 100^\circ\text{C}$) shows favorable behavior, which retains significant ductility and metallic property [17]. The uranium–aluminum system has three intermetallic compounds (Fig. 1.2): UAl_2 , UAl_3 and UAl_4 . UAl_2 solidifies at 1615°C ; UAl_3 forms at 1355°C by a peritectic reaction between the solid phase UAl_2 and a liquid phase of Al–60wt%U. UAl_4 forms at 740°C by a peritectic reaction between the solid phase UAl_3 and a liquid composition of Al–18wt%U. Uranium–aluminum alloys in which the matrix is either primarily

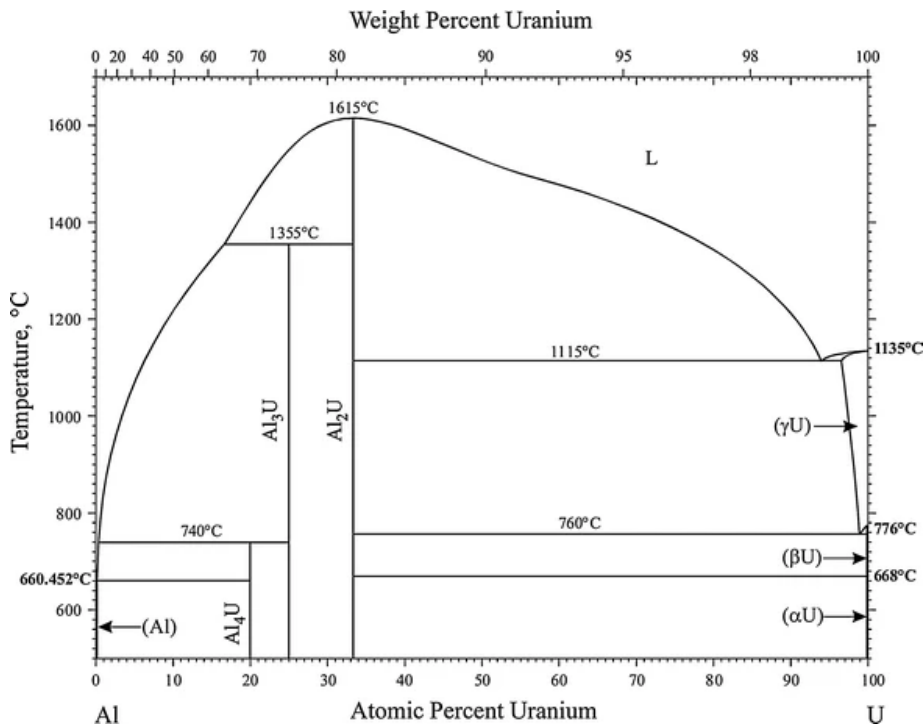


Figure 1.2. Uranium–aluminum phase diagram. Reprinted with permission from Springer Nature: H. Okamoto [19], © 2012.

aluminum or $\text{Al}+\text{UAl}_4$ eutectic are widely being used as research reactor fuel. This type of fuel is called a *dispersion*³ fuel.

Uranium–aluminum alloys can have densities as high as $4.522 \text{ gU}/\text{cm}^3$ [20], but for LEU the required density exceeds $8.5 \text{ gU}/\text{cm}^3$ [21]. There are only a few fuel phases with both a high uranium density and stable irradiation properties. The two types of fuels that meet the density requirements are γ -stable uranium and U_6Me (Me = transition metal). U_6Me fuels showed very poor irradiation performance at low fission density ($3 \times 10^{21} \text{ fissions}/\text{cm}^3$) [22–24]. The γ phase of uranium can be stabilized by alloying it with suitable elements. Several transition metals stabilize γ -uranium. Elements such as molybdenum (Mo), niobium (Nb), titanium (Ti), and zirconium (Zr) have been tried as alloying elements because of their solubility in

³A dispersion fuel is one in which the fissile material is contained as a compound dispersed in a nonfissile matrix [18].

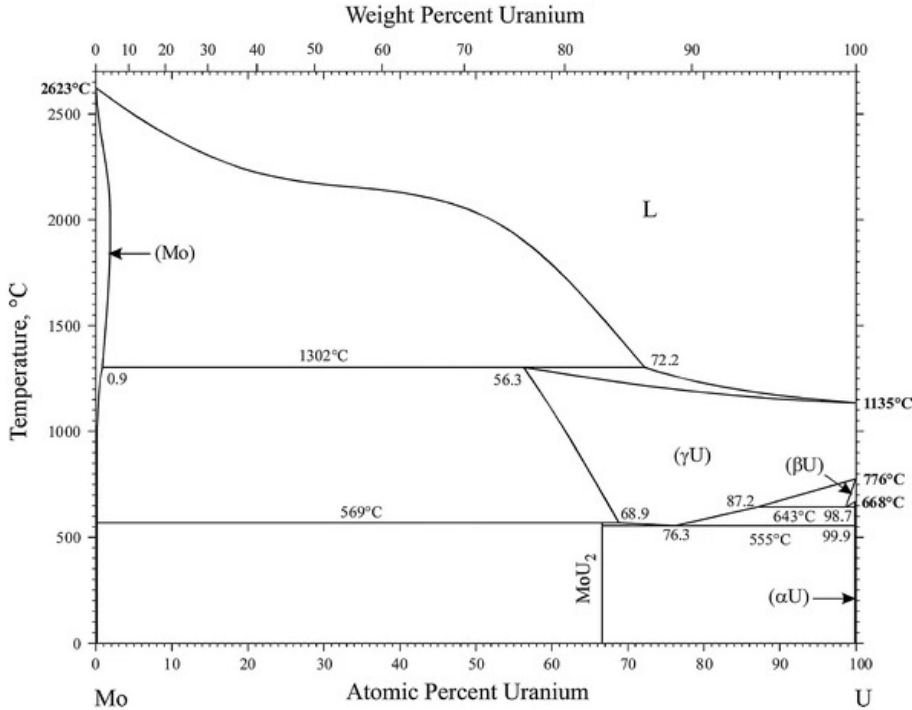


Figure 1.3. Uranium–molybdenum phase diagram. Reprinted with permission from Springer Nature: H. Okamoto [32], © 2012.

γ -uranium [25–27]. The U–Mo phase diagram (Fig. 1.3) has a eutectoid at 11.1 wt% Mo and 555°C. If the U–Mo γ phase contains more than 5 to 7 wt% Mo, the γ phase can be retained at room temperature by rapid cooling [28, 29]. To take advantage of this, uranium alloyed with 10 wt% molybdenum (U-10Mo) is currently being developed as a potential high-density LEU fuel for high-performance research reactors [13, 30, 31].

Before the current interest in U–Mo metallic fuels, some early nuclear reactors used metallic fuels because of the combination of high uranium density and metallic properties. The Godiva IV pulsed reactors at Los Alamos (initially known as *Lady Godiva*) used U–Mo alloys, which date back to 1960 [33]. The Fast Burst Reactor (FBR) at White Sands, the Army Pulsed Radiation Facility (Aberdeen, MD), and the Sandia Pulsed Reactor II also used U–Mo alloys [33–35]. All of these reactors

utilized the γ -phase of uranium, but because of their short irradiation time, the impacts of fuel burnup were minimal [36]. Outside USA, the Dounreay Fast Reactor in the U.K. used a number of metal-fuel-based designs, which includes U-9.1Mo (9.1 wt% Mo) and U-7Mo clad in niobium [37]. The highly alloyed fuel cracked more, even though the U-9.1Mo fuel swelled slightly less than U-7Mo [38].

The primary concern with γ -uranium alloys is to ensure that the fuel remains in the γ phase during reactor operation. A series of experiments was performed to map the fission rate and temperature dependence of the γ phase's stability [39]. Two types of U–Mo alloy fuels have been designed and tested. One is monolithic fuel, in which a thin layer of U–Mo foil is bonded to aluminum cladding. The other is a dispersion fuel, in which U–Mo fuel particles are dispersed in an aluminum matrix.

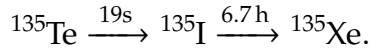
For five decades, dispersion fuels have powered many test and research reactors worldwide. The manufacturing process and operating conditions are well-known for these types of fuels. High-burnup testing of dispersion fuels showed a pattern of breakaway swelling⁴ behavior at intermediate burnup. Post-irradiation examinations of U–Mo dispersion fuel revealed that this phenomenon is related to the formation of a ternary aluminide phase. Reaction between the U–Mo fuel kernels and aluminum cladding occurs during irradiation and forms a ternary $[(U\text{-Mo})\text{Al}_x]$ phase, which releases fission gas at the boundary between the interaction phase and the aluminum matrix [40–43]. These gas bubbles have a tendency to aggregate into the gas pockets, which weakens the fuel meat by exerting internal pressure. The result is mechanical failure and an increase in fuel volume. To eliminate the fuel–matrix interaction, a ‘monolithic’ U–Mo fuel was suggested. In monolithic fuels, a zirconium foil is used as a diffusion barrier between the fuel and the cladding (aluminum) to prevent diffusion of molybdenum into the cladding [41].

⁴*Breakaway* is defined as “the limiting exposure, beyond which there will be a marked increase in the rate of swelling as a function of burnup” [44].

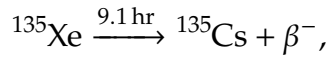
1.2 Fission Gas

The behavior of fission gas—xenon and krypton—has perplexed and fascinated both experimentalists and theorists more than many processes that simultaneously occur in a nuclear fuel elements during irradiation. These inert gases are insoluble in the fuel matrix, causing them to form small gas bubbles. If the gas is released from the fuel, the pressure within the cladding rises, which ultimately results in failure. If the fission gases are retained in the fuel, however, they almost always precipitate as bubbles and cause swelling in the fuel matrix. Swelling adversely impacts the fuel's efficiency. It also impacts the thermal conductivity of the fuel, thereby disrupting the heat extraction from the fuel. One particular xenon isotope, ^{135}Xe also has a large neutron absorption cross section, which can lead to a reactor “poisoning.” As a result, the basic aspects of inert gas behavior are commonly studied for fuel such as UO_2 .

Xenon is produced directly from fission: 0.3% of fission products are ^{135}Xe . It is also produced by the decay of ^{135}I via the reaction



^{135}I constitutes almost 6.1% of fission products. Thus, 95% of total xenon production is due to the decay of iodine. Xenon is removed from the fuel by beta decay



or by neutron absorption:



In U–Mo fuel, fission gas forms bubbles both inside the grain and on grain boundaries. Inside the grains, fission gas forms a gas bubble superlattice [45, 46].

This dissertation investigates how fission gas (xenon and krypton) impacts the transport properties of U–Mo fuel. Chapter 2 summarizes the theoretical methods used in this work. In Chapter 3, we discuss the reduction of thermal conductivity in U–Mo alloys due to the presence of fission gas. In Chapter 4, we introduce a new pseudopotential for metallic uranium to study its properties using density functional theory (DFT). In Chapter 5, we look into the diffusion mechanism of xenon in γ -uranium and U–Mo alloys. In Chapter 6, we discuss the interaction of helium with a potential plasma-facing material for fusion, lithium, using DFT. We discuss conclusions and potential future work in Chapter 7.

References

1. A. Glaser, in *The 27th International Meeting on Reduced Enrichment for Research and Test Reactors (RERTR)* (Boston, Massachusetts, 2005).
2. IAEA, *Management of High Enriched Uranium for Peaceful Purposes: Status and Trends*, TECDOC Series No. 1452 (International Atomic Energy Agency, Vienna, 2005).
3. A. H. Montgomery and S. D. Sagan, J. Conflict Resolut. **53**, 302 (2009).
4. W. H. Donnelly, Energy Policy **8**, 335 (1980).
5. R. Serber, *The Los Alamos Primer: The First Lectures on How to Build an Atomic Bomb* (University of California Press, 1992).
6. A. Travelli, *Current Status of the RERTR Program*, Tech. Rep. CONF-801144-9/DE83017214 (Argonne National Laboratory, Illinois (USA), 1980).
7. J. L. Snelgrove, G. L. Hofman, M. K. Meyer, C. L. Trybus, and T. C. Wienczek, Nucl. Eng. Des. **178**, 119 (1997).
8. D. E. Burkes, I. J. Schwerdt, T. K. Huber, H. Breitkreutz, C. Reiter, W. Petry, J. L. Schultheiss, A. M. Casella, A. J. Casella, E. C. Buck, K. N. Pool, P. J. MacFarlan, M. K. Edwards, and F. N. Smith, J. Nucl. Mater. **547**, 152823 (2021).

9. E. Wilson, A. Bergeron, J. Stillman, T. Heltemes, D. Jaluvka, and L. Jamison, in *Proceedings of the 2017 European Research Reactor Conference* (RRFM Rotterdam, Netherlands, 2017).
10. National Academies of Sciences, Engineering, and Medicine, *Reducing the Use of Highly Enriched Uranium in Civilian Research Reactors* (National Academies Press, Washington, DC, 2016) pp. 12–19.
11. National Research Council, *Progress, Challenges, and Opportunities for Converting U.S. and Russian Research Reactors: A Workshop Report* (National Academies Press, Washington, DC, 2012).
12. A. R. Kaufmann, *Nuclear Reactor Fuel Elements: Metallurgy and Fabrication* (Interscience Publishers, New York, 1962).
13. M. K. Meyer, J. Gan, J. F. Jue, D. D. Keiser, E. Perez, A. Robinson, D. M. Wachs, N. Woolstenhulme, G. L. Hofman, and Y. S. Kim, *Nucl. Eng. Technol.* **46**, 169 (2014).
14. S. Pugh, *J. Nucl. Mater.* **4**, 177 (1961).
15. B. Loomis and D. Pracht, *Swelling of Uranium and Uranium Alloys on Postirradiation Annealing*, Tech. Rep. ANL-6532 (Argonne National Laboratory, Argonne, Illinois, USA, 1962).
16. H. H. Chiswik, A. E. Dwight, L. T. Lloyd, M. V. Nevitt, and S. T. Zegler, *Advances in the Physical Metallurgy of Uranium and its Alloys*, Tech. Rep. A/-CONF.15/P/713 (Argonne National Laboratory, Lemont, Illinois, USA, 1958).
17. K. Farrell, Performance of Aluminum in Research Reactors, in *Comprehensive Nuclear Materials*, Vol. 5, edited by R. J. Konings (Elsevier, Oxford, 2012) Chap. 5, pp. 143–187.
18. D. W. White, A. P. Beard, and A. H. Willis, *Irradiation Behavior of Dispersion Fuels*, Tech. Rep. KAPL-1909; KAPL-P-1849 (Knolls Atomic Power Laboratory, Schenectady, New York (USA), 1957).
19. H. Okamoto, *J. Phase Equilib. Diff.* **33**, 489 (2012).
20. H. A. Saller, R. F. Dickerson, F. A. Rough, E. L. Foster, A. A. Bauer, and J. R. Lulay, *A Study of Aluminum-Uranium Alloys*, Tech. Rep. BMI-1066 (Battelle Memorial Institute, Columbus, Ohio (USA), 1956).
21. L. Sannen, S. van den Berghe, and A. Leenaers, in *6th Forum on New Materials - Part B, Advances in Science and Technology*, Vol. 94 (Trans Tech Publications Ltd, 2014) pp. 43–54.
22. M. K. Meyer, T. C. Wienczek, S. L. Hayes, and G. L. Hofman, *J. Nucl. Mater.* **278**, 358 (2000).

23. G. L. Hofman, R. F. Domagala, and G. L. Copeland, *J. Nucl. Mater.* **150**, 238 (1987).
24. S. van den Berghe, A. Leenaers, E. Koonen, and L. Sannen, in *Advances in Science and Technology*, Vol. 73 (Trans Tech Publications Ltd, 2011) pp. 78–90.
25. G. Donzé and G. Cabane, *J. Nucl. Mater.* **1**, 364 (1959).
26. F. Giraud-Heraud and J. Guillaumin, *Acta Metall.* **21**, 1243 (1973).
27. D. A. Lopes, T. A. G. Restivo, and A. F. Padilha, *J. Nucl. Mater.* **440**, 304 (2013).
28. H. A. Saller, F. Rough, and A. Bauer, *Transformation Kinetics of Uranium-Molybdenum Alloys*, Tech. Rep. BMI-957 (Battelle Memorial Instite, Columbus, Ohio (USA), 1954).
29. W. A. Bostrom and E. K. Halteman, *The Metastable Gamma Phase in Uranium Base Molybdenum Alloys*, Tech. Rep. WAPD-T-415 (Westinghouse Electric Corporation, Bettis Plant, Pittsburgh (USA), 1956).
30. R. Prabhakaran, *JOM* **69**, 2529 (2017).
31. W. Williams, A. Robinson, and B. Rabin, *JOM* **69**, 2546 (2017).
32. H. Okamoto, *J. Phase Equilib. Diff.* **33**, 497 (2012).
33. T. F. Wimett, *Fast Burst Reactors in the USA*, Tech. Rep. LA-DC-6786; SM-62/53; CONF-650 (Los Alamos Scientific Laboratory, Los Alamos, New Mexico (USA), 1965).
34. J. Mihalczo, *Static and Dynamic Measurements with the Army Pulse Radiation Facility Reactor.*, Tech. Rep. ORNL-TM-2330 (Oak Ridge National Laboratory, Tennessee (USA), 1969).
35. L. Bonzon and J. Snyder, *Sandia Pulsed Reactor II (SPR II): Experimenter's Manual*, Tech. Rep. SLA-73-551 (Sandia Laboratories, Albuquerque, New Mexico(USA), 1973).
36. J. A. Horak, J. A. Reuscher, and D. J. Sasmor, *Operating Experience with Uranium–Molybdenum Fuel in Pulsed Reactors*, Tech. Rep. SLA-73-5559; CONF-730801-5 (Sandia Laboratories, Albuquerque, New Mexico(USA), 1973).
37. R. Matthews, J. Phillips, K. Henry, R. Allardice, D. Donaldson, and H. Tilbe, *Performance and operation of the Dounreay fast reactor*, Tech. Rep. A/CONF.28/P/130 (United Kingdom Atomic Energy Authority, Caithness, Scotland (United Kingdom), 1964).
38. S. A. Cottrell, E. Edmonds, P. Higginson, and W. Oldfield, *Development and Performance of Dounreay Fast Reactor Metal Fuel*, Tech. Rep. A/CONF.28/P/150 (United Kingdom Atomic Energy Authority. Industrial Group. Dounreay, 1964).

39. IAEA, *Development Status of Metallic, Dispersion and Non-Oxide Advanced and Alternative Fuels for Power and Research Reactors*, TECDOC Series No. 1374 (International Atomic Energy Agency, Vienna, 2003).
40. A. Leenaers, S. Van den Berghe, E. Koonen, C. Jarousse, F. Huet, M. Trotabas, M. Boyard, S. Guillot, L. Sannen, and M. Verwerft, *J. Nucl. Mater.* **335**, 39 (2004).
41. J.-F. Jue, D. D. Keiser, C. R. Breckenridge, G. A. Moore, and M. K. Meyer, *J. Nucl. Mater.* **448**, 250 (2014).
42. S. Van den Berghe, W. Van Renterghem, and A. Leenaers, *J. Nucl. Mater.* **375**, 340 (2008).
43. D. Olander, *J. Nucl. Mater.* **383**, 201 (2009).
44. A. Guay, *Uranium Swelling in N-Reactor (PT-NR-4, Sup. A, Report No. 1)*, Tech. Rep. RL-NRD-550 (General Electric, Hanford Atomic Products, Richland, Washington (USA), 1965).
45. B. D. Miller, J. Gan, J. Madden, J.-F. Jue, A. Robinson, and D. D. Keiser, *J. Nucl. Mater.* **424**, 38 (2012).
46. J. Gan, D. D. Keiser, D. M. Wachs, A. B. Robinson, B. D. Miller, and T. R. Allen, *J. Nucl. Mater.* **396**, 234 (2010).

CHAPTER 2

BACKGROUND

2.1 Electronic Structure Calculations

Electronic structure methods have become an essential tool in materials science over the last three decades. Any relevant physical property of real materials can, in principle, be described by the laws of quantum mechanics. The foundation of these methods is the approximate solution of the many-body Schrödinger equation. Given the positions of the atomic nuclei and the total number of electrons in the system, the energy and other properties can be approximated. The ability to obtain a solution that is good enough requires an efficient description of the electronic system and considerable computational power.

2.1.1 The Many-Body Hamiltonian

The quantum theory of electrons and nuclei controls the characteristics of matter over wide ranges of temperature and pressure. One of the most fundamental qualities of solids is that they have a variety of properties that result from the collective behavior of atoms. Electrical conductivity as well as magnetism arise as collective properties of the atoms in the solid. The wavefunction of the solid can be described by the Schrödinger equation,

$$\mathcal{H} |\Psi(t)\rangle = i\hbar \frac{\partial}{\partial t} |\Psi(t)\rangle, \quad (2.1)$$

where \mathcal{H} is the Hamiltonian operator. If the Hamiltonian is time-independent, the Schrödinger equation can be simplified. For time-dependent problems, the wavefunction can be broken into the product of a time-dependent part and a time-independent part, the latter of which depends on the positions of the electrons and nuclei. The solution of the time-dependent Schrödinger equation is of the following form:¹

$$|\Psi(\mathbf{r}, t)\rangle = e^{-iEt/\hbar} |\psi(\mathbf{r})\rangle \quad (2.2)$$

The time-dependent part is trivial. The time-independent part obeys the time-dependent Schrödinger equation,

$$\mathcal{H} |\psi_j\rangle = E_j |\psi_j\rangle, \quad (2.3)$$

where the Hamiltonian operator represents the total energy of the particles:

$$\begin{aligned} \mathcal{H} &= - \sum_j \frac{\hbar^2}{2m_e} \nabla_j^2 - \sum_a \frac{\hbar^2}{2M_a} \nabla_a^2 \\ &\quad - \sum_{j,a} \frac{Z_a e^2}{|\mathbf{r}_j - \mathbf{R}_a|} + \frac{1}{2} \sum_{j,k}^{j \neq k} \frac{e^2}{|\mathbf{r}_j - \mathbf{r}_k|} + \frac{1}{2} \sum_{a,b}^{a \neq b} \frac{Z_a Z_b e^2}{|\mathbf{R}_a - \mathbf{R}_b|} \\ \mathcal{H} &\stackrel{\text{(atomic unit)}}{=} - \sum_j \frac{1}{2} \nabla_j^2 - \sum_a \frac{1}{2\tilde{M}_a} \nabla_a^2 \\ &\quad - \sum_{j,a} \frac{Z_a}{|\mathbf{r}_j - \mathbf{R}_a|} + \frac{1}{2} \sum_{j,k}^{j \neq k} \frac{1}{|\mathbf{r}_j - \mathbf{r}_k|} + \frac{1}{2} \sum_{a,b}^{a \neq b} \frac{Z_a Z_b}{|\mathbf{R}_a - \mathbf{R}_b|} \\ &= T_e + T_N + V_{Ne}(\mathbf{r}, \mathbf{R}) + V_{ee}(\mathbf{r}) + V_{NN}(\mathbf{R}) \end{aligned} \quad (2.4)$$

It is convenient to use atomic units (see Appendix A), which will be used for the remainder of the discussion. In these units, the electron mass m_e as well as

¹More precisely, the solution would be written as the superposition $\Psi(\mathbf{r}, t) = \sum_j C_j \psi_j(\mathbf{r}) e^{-iE_j t/\hbar}$, where $\psi_j(\mathbf{r})$ are eigenfunctions of the time-independent Schrödinger equation and C_j are complex coefficients.

the elementary charge e , the reduced Planck constant \hbar , and Coulomb's constant $1/4\pi\epsilon_0$ are unity, leaving $\tilde{M}_a = M_a/m_e$ as the relative atomic mass of the nucleus of atom a . \mathbf{r}_j denotes the position of the j^{th} electron, while \mathbf{R}_a is the position of the nucleus of atom a and Z_a is that nucleus' atomic number. A solution of the time-independent Schrödinger equation (2.3) would be a function dependent on the spatial coordinates of all particles in the system and is, as such, only obtainable for very idealized systems. The Schrödinger equation with the above Hamiltonian is impossible to solve exactly for most of systems of interest. A series of approximations and methods were therefore developed to reduce the complexity of the problem. With the help of Eqn. (2.4) the Schrödinger equation (2.3) becomes

$$[T_e + T_N + V_{Ne}(\mathbf{r}, \mathbf{R}) + V_{ee}(\mathbf{r}) + V_{NN}(\mathbf{R})]\Phi(\mathbf{r}, \mathbf{R}) = E\Phi(\mathbf{r}, \mathbf{R}) \quad (2.5)$$

In order to simplify the equations, the electronic coordinates and spin indices are combined into a vector $\mathbf{r} = (\vec{r}, s)$, and \mathbf{R} denotes the nuclear coordinates. The wavefunction here is a regular function of the atomic positions but a quantum state $|\Phi(\vec{r})\rangle$ in the Hilbert space for the electrons and nuclei, so that $\Phi(\vec{r}) = \langle \vec{r} | \Phi(\mathbf{r}, \mathbf{R}) \rangle$. The nuclear mass exceeds the electron mass by more than three orders of magnitude, and so the electrons and nuclei move on different time scales. Thus, the wavefunction $\Phi(\mathbf{r}, \mathbf{R})$ can be separated into an electronic part $\Psi(\mathbf{r}, \mathbf{R})$ and a nuclear wavefunction $\chi(\mathbf{R})$,

$$\Phi(\mathbf{r}, \mathbf{R}) = \Psi(\mathbf{r}, \mathbf{R})\chi(\mathbf{R}) \quad (2.6)$$

The nuclear wavefunction is much more localized, which is why the Schrödinger equation can be separated into two parts:

$$[T_e + V_{ee}(\mathbf{r}) + V_{Ne}(\mathbf{r}, \mathbf{R})]\Psi(\mathbf{r}, \mathbf{R}) = \epsilon_n(\mathbf{R})\Psi(\mathbf{r}, \mathbf{R}) \quad (2.7)$$

$$[T_N + V_{NN}(\mathbf{R}) + \epsilon_n(\mathbf{R})]\chi(\mathbf{R}) = E\chi(\mathbf{R}) \quad (2.8)$$

The nuclear positions (\mathbf{R}) in the equation (2.7) serves only as a parameter and it is possible to use the *adiabatic* or *Born–Oppenheimer* approximation. On the timescale of the nuclear motion, the electron follow the ions adiabatically. As a further approximation, the quantum effects on the motion of the nuclei are neglected and the time-dependent Schrödinger equation is replaced by Newton's equation of motion;

$$\frac{\partial P_I}{\partial t} = -\nabla_I E_0(\mathbf{R}) \quad (2.9)$$

$$\text{with } E_0(\mathbf{R}) = \epsilon_0(\mathbf{R}) + V_{NN}(\mathbf{R}) \quad (2.10)$$

This refers to so-called *ab-initio* molecular dynamics, where the forces around a nuclei are calculated from the electronic ground state. Here, P_I is the momenta of the nucleus. Equations (2.7) and (2.8) are not generally applicable. However, for several physical systems, the Born–Oppenheimer approximation works and Eqn. (2.7), (2.8) produces meaningful results. In solid state physics, Eqn. (2.8) is usually written in a classical form and Eqn. (2.7) becomes the problem to be solved. It is still a very complicated equation, where the term describing the interaction between electrons would require the knowledge of d^{3N} (d = number of discrete points) variables for a system of N electrons. Such a large number of variables make the problem computationally not tractable and several approximate methods have been developed. Some of the important methods will be discussed in the next of this chapter.

These approximate methods are based on the *independent particle* approximation, in which the Hamiltonian takes the form

$$\mathcal{H} = \sum_j \mathcal{H}_j. \quad (2.11)$$

The electronic wavefunction can be written as the product of single-particle wavefunctions. This leads to a further simplification of the Hamiltonian,

$$\begin{aligned}\mathcal{H} &= -\sum_j^N \frac{1}{2} \nabla_j^2 - \sum_j^N \sum_a^M \frac{Z_a}{|\mathbf{r}_j - \mathbf{R}_a|} + \frac{1}{2} \sum_{j \neq k}^N \sum_k^N \frac{1}{|\mathbf{r}_j - \mathbf{r}_k|} \\ &= T_e + V^{\text{ext}} + \frac{1}{2} \sum_{j \neq k} v_{jk}(|\mathbf{r}_j - \mathbf{r}_k|).\end{aligned}\quad (2.12)$$

2.1.2 Hartree–Fock Approach

A very simple way to write the many-electron wavefunction is as a product of single-particle wavefunctions:

$$\Psi(r_1, r_2, \dots, r_N) = \prod_j^N \psi_j(r_j). \quad (2.13)$$

The Hamiltonian (2.12) is not just a sum of single-particle Hamiltonians: the true wavefunctions cannot be written in the product of the form (2.13). Furthermore, the wavefunction in (2.13) does not have the *antisymmetry* property required for fermions.

The fermionic nature of the electrons imposes the Pauli exclusion principle as an additional constraint. One can achieve an antisymmetric many-body wavefunction by writing the electronic wavefunction as a Slater determinant of single-particle wavefunctions:

$$\Psi(r_1, r_2, \dots, r_N) = \frac{1}{\sqrt{N!}} \begin{vmatrix} \psi_1(\mathbf{r}_1) & \psi_1(\mathbf{r}_2) & \dots & \psi_1(\mathbf{r}_N) \\ \psi_2(\mathbf{r}_1) & \psi_2(\mathbf{r}_2) & \dots & \dots \\ \vdots & & & \ddots \\ \psi_N(\mathbf{r}_1) & \dots & & \psi_N(\mathbf{r}_N) \end{vmatrix}. \quad (2.14)$$

The expectation value of the Hamiltonian (2.12) can be calculated using this wavefunction, which leads to an energy functional that can be minimized variationally (2.15).

$$E \leq E' \equiv \frac{\langle \Psi | \mathcal{H} | \Psi \rangle}{\langle \Psi | \Psi \rangle} \quad (2.15)$$

Here, any state $|\Psi\rangle$ provides an upper bound E' for the exact ground-state energy E . An additional constraint is that the single-particle orbitals are to be normalized. The normalization condition is

$$\langle \psi_i(\mathbf{r}_i) | \psi_j(\mathbf{r}_j) \rangle = \int \psi_i(\mathbf{r})^* \psi_j(\mathbf{r}) d\mathbf{r} = \delta_{ij}. \quad (2.16)$$

The many-particle wavefunction (2.14) and the Hamiltonian (2.12) give the single particle Hartree–Fock² (HF) Equations,

$$\begin{aligned} \mathcal{H}_i^{\text{HF}} \psi_i(\mathbf{r}_i) &= \left[-\frac{\nabla^2}{2} + v^{\text{ext}}(\mathbf{r}_i) + v^{\text{H}}(\mathbf{r}_i) + v^{\text{EX}}(\mathbf{r}_i) \right] \psi_i(\mathbf{r}_i) \\ &= \epsilon_i \psi_i(\mathbf{r}_i) \end{aligned} \quad (2.17)$$

where the kinetic energy term T_e and the external potential V^{ext} are unchanged from Eqn. (2.12) and are divided into the single particle contributions, with $V^{\text{ext}} = \sum_{i=1}^N v^{\text{ext}}(\mathbf{r}_i)$. The third term in Eqn. (2.12), the interaction between the electrons, produces two additional operators v^{H} and v^{EX} . The first term is called the *Hartree potential* and has the following form:

$$\begin{aligned} v^{\text{H}}(\mathbf{r}_i) &= \sum_{j=1}^N \int \frac{|\psi_j(\mathbf{r}_j)|^2}{|\mathbf{r}_i - \mathbf{r}_j|} d\mathbf{r}_j \\ &= \int \frac{n(\mathbf{r}_j)}{|\mathbf{r}_i - \mathbf{r}_j|} d\mathbf{r}_j \end{aligned} \quad (2.18)$$

²From Hartree [1], who first postulated the factorization of the wavefunction in single particle states in 1928, and Fock [2], who redefined the method by including Slater determinant.

where

$$n(\mathbf{r}) = N \int |\Psi^0(\mathbf{r}_1, \dots, \mathbf{r}_N)|^2 d\mathbf{r}_1, \dots, d\mathbf{r}_N. \quad (2.19)$$

The Hartree potential takes account of the mean-field Coulombic interaction between the i^{th} electron and the total electron density $n(\mathbf{r})$ as defined in Eqn (2.18). The second term in Eqn. (2.17) can be written in an integral form,

$$v^{\text{EX}} \psi_i(\mathbf{r}_i) = \sum_{j=1}^N \int \psi_j^*(\mathbf{r}_j) \frac{1}{|\mathbf{r}_i - \mathbf{r}_j|} \psi_j(\mathbf{r}_i) \psi_i(\mathbf{r}_j) d\mathbf{r}_j \quad (2.20)$$

The quantity v^{EX} is known as the *exchange potential* and takes account the anti-symmetric nature of the total wavefunction. When the two particles are the same coordinates, the Hartree and exchange potential cancel each other, which eliminates “self interaction”.

The solutions of the Hartree–Fock equation are the HF orbitals. Since the orbitals are also part of the equation, the problem needs to be solved iteratively until the equation is self-consistent. The exchange operator v^{EX} is usually referred to as a non-local operator, which makes it impossible to carry out full HF calculations for condensed matter system without introducing the local approximation.

Evaluating v^{EX} is already a non-trivial task, but the HF equation approximates the full many-body problem in a way that leaves out important contributions. What is not considered is usually referred to as *correlation* which adds an extra term in Eqn. (2.17). This contribution is small compared to the total energy of the system, but it is crucial for many solid systems. The *correlation* contribution to the total energy mainly takes account of the fact that an electron is screened by others from the interaction with the nuclei and more distant electrons. The HF method usually works for systems in which the particles do not “see” each other. HF performs badly for systems with large number of electrons in metals.

2.1.3 Density Functional Theory

In the Hartree–Fock approach the wavefunction of the many-body problem is solved self-consistently. The electron density $n(\mathbf{r})$ plays a prominent role in self-consistent calculations. This raises the question as to whether there exists an *exact* theory for the ground state electronic system of the density $n(\mathbf{r})$. This question leads to the *density functional theory* (DFT). The simplest and oldest version of the DFT formalism is Thomas–Fermi theory [3, 4].

2.1.3.1 Density

The idea to shift focus from wavefunction ($\Psi(\mathbf{r})$) to density ($n(\mathbf{r})$) to solve many-body Schrödinger equation is very important. For many particle systems the density, $n(\mathbf{r})$, is calculated by the expectation value of the single-particle density operator for the many-body wavefunction,

$$\hat{n}(\mathbf{r}) = \sum_i^N \delta(\mathbf{r} - \mathbf{r}_i). \quad (2.21)$$

The density can be calculated as follows:

$$\begin{aligned} n(\mathbf{r}) &= \langle \Psi | \hat{n}(\mathbf{r}) | \Psi \rangle = \sum_i^N \int \delta(\mathbf{r} - \mathbf{r}_i) |\Psi(\mathbf{r}_1, \dots, \mathbf{r}_N)|^2 d\mathbf{r}_1 d\mathbf{r}_2 \dots d\mathbf{r}_N \\ &= N \int |\Psi(\mathbf{r}, \mathbf{r}_2, \dots, \mathbf{r}_N)|^2 d\mathbf{r}_2 \dots d\mathbf{r}_N \end{aligned} \quad (2.22)$$

where \mathbf{r}_i is the position of the i^{th} electron. Assuming the wavefunction is normalized to unity, the above integration over all spaces yields the total number of electrons,

$$N = \int n(\mathbf{r}) d\mathbf{r} \quad (2.23)$$

2.1.3.2 Energy in Terms of the Density

It is necessary to represent all the energy in terms of density to eliminate wavefunction dependency. This is necessary because the electronic energy needs to be minimized with respect to density to obtain the ground state energy and corresponding electronic density. This is one of the foundations of DFT that was proposed by Hohenberg and Kohn in 1964 [5].

As we have discussed earlier (HF theory), once the wavefunction is obtained by solving the Hamiltonian the observable of other operator can be calculated by calculating the expectation value of the operator. This allows us to calculate the separate energy terms associated to the potential operator given in the Hamiltonian (2.12). For the sake of completeness lets reproduce the Hamiltonian in a simplest form

$$\begin{aligned}\hat{\mathcal{H}}_e &= \hat{T} + \hat{V}_{en} + \hat{V}_{ee} \\ &= -\sum_{j=1}^N \frac{1}{2} \nabla_j^2 - \sum_{j=1}^N \sum_{a=1}^M \frac{Z_a}{|\mathbf{r}_j - \mathbf{R}_a|} + \frac{1}{2} \sum_{j \neq k} \sum_{k=1}^N \frac{1}{|\mathbf{r}_j - \mathbf{r}_k|}\end{aligned}\quad (2.24)$$

Let's assume we have managed to solve the many-body problem and have obtained the wavefunction. The expectation value of the nucleus–electron interaction operator is given by

$$\begin{aligned}\langle \Psi(\mathbf{r}_1, \dots, \mathbf{r}_N) | \hat{V}_{ne} | \psi(\mathbf{r}_1, \dots, \mathbf{r}_N) \rangle &= - \sum_j^N \sum_a^M \Psi^*(\mathbf{r}_1, \dots, \mathbf{r}_N) \frac{Z_a}{|\mathbf{r}_j - \mathbf{R}_a|} \Psi(\mathbf{r}_1, \dots, \mathbf{r}_N) \\ &= E_{ne} = - \sum_a^{M=N} \int n(\mathbf{r}) \frac{Z_a}{|\mathbf{r} - \mathbf{R}_a|} d\mathbf{r} \\ &= \int n(\mathbf{r}) V_{ne}(\mathbf{r}) d\mathbf{r}\end{aligned}\quad (2.25)$$

The equivalent derivation for the electron–electron term is not trivial, because the electron–electron terms require a two-particle density instead of a single-particle

density,

$$E_{ee} = \frac{1}{2} \iint \frac{n^{(2)}(\mathbf{r}, \mathbf{r}')}{|\mathbf{r} - \mathbf{r}'|} d\mathbf{r} d\mathbf{r}', \quad (2.26)$$

where $n^{(2)}$ can be interpreted as the probability of finding an electron at location \mathbf{r} given that a second electron exists at location \mathbf{r}' . Eqn. (2.26) makes the many-particle problem impossible to solve, as it would be required to know the conditional probability $n^{(2)}$ to solve the equation exactly. If the two electrons were completely uncorrelated, then the two-particle density can be written as the product of one-particle densities,

$$n^{(2)} = n(\mathbf{r})n(\mathbf{r}') + \Delta n^{(2)}(\mathbf{r}, \mathbf{r}'), \quad (2.27)$$

where $n^{(2)}$ is a correction term. The electron–electron energy can be written as

$$E_{ee} = \frac{1}{2} \iint \frac{n(\mathbf{r})n(\mathbf{r}')}{|\mathbf{r} - \mathbf{r}'|} d\mathbf{r} d\mathbf{r}' + \Delta E_{ee} \quad (2.28)$$

where the ΔE_{ee} term comes from the correction term in Eqn. (2.27). The kinetic energy operator has a derivative term, which creates a problem in calculating the expectation value. This is because of the derivative, it is not possible to collect the wavefunction and its conjugate as a single norm square,

$$T = -\frac{1}{2} \int \Psi^*(\mathbf{r}_1, \dots, \mathbf{r}_N) \nabla^2 \Psi(\mathbf{r}_1, \dots, \mathbf{r}_N) d\mathbf{r}. \quad (2.29)$$

In order to calculate the kinetic energy, DFT expands the electron density as the sum of squares of single-particle orbitals,

$$n(\mathbf{r}) = \sum_{j=1}^{N_e} |\phi_j(\mathbf{r})|^2. \quad (2.30)$$

These orbitals are called *Kohn–Sham* orbitals. Now the kinetic energy term can be written as single-particle kinetic energy plus a correction,

$$T = -\frac{1}{2} \sum_{j=1}^{N_e} \int \phi_j^*(\mathbf{r}) \nabla^2 \phi_j(\mathbf{r}) d\mathbf{r} + \Delta T. \quad (2.31)$$

The total ground state energy can be written as

$$\begin{aligned} E &= -\frac{1}{2} \sum_{j=1}^{N_e} \int \phi_j^*(\mathbf{r}) \nabla^2 \phi_j(\mathbf{r}) d\mathbf{r} + \int n(\mathbf{r}) V_{ne}(\mathbf{r}) d\mathbf{r} \\ &\quad + \frac{1}{2} \iint \frac{n(\mathbf{r}) n(\mathbf{r}')}{|\mathbf{r} - \mathbf{r}'|} d\mathbf{r} d\mathbf{r}' + \Delta E_{ee} + \Delta T \\ &= -\frac{1}{2} \sum_{j=1}^{N_e} \int \phi_j^*(\mathbf{r}) \nabla^2 \phi_j(\mathbf{r}) d\mathbf{r} + \int n(\mathbf{r}) V_{ne}(\mathbf{r}) d\mathbf{r} \\ &\quad + \frac{1}{2} \iint \frac{n(\mathbf{r}) n(\mathbf{r}')}{|\mathbf{r} - \mathbf{r}'|} d\mathbf{r} d\mathbf{r}' + E_{xc} \end{aligned} \quad (2.32)$$

Here, the two correction terms are replaced with E_{xc} , called the *exchange–correlation* energy. The origin of this term is the difference between N interacting and noninteracting particles. Several well-developed approximations exist for the exchange–correlation energy, and one of them is called the local density approximation (LDA),

$$E_{xc} = \int n(\mathbf{r}) \epsilon_{xc}([n(\mathbf{r})]) d\mathbf{r} \quad (2.33)$$

where ϵ_{xc} is the energy per electron at point \mathbf{r} that depends only on the density $n(\mathbf{r})$. Thus, within the local density approximation, the total energy can be written

$$\begin{aligned} E &= -\frac{1}{2} \sum_{j=1}^{N_e} \int \phi_j^*(\mathbf{r}) \nabla^2 \phi_j(\mathbf{r}) d\mathbf{r} + \int n(\mathbf{r}) V_{ne}(\mathbf{r}) d\mathbf{r} \\ &\quad + \frac{1}{2} \iint \frac{n(\mathbf{r}) n(\mathbf{r}')}{|\mathbf{r} - \mathbf{r}'|} d\mathbf{r} d\mathbf{r}' + \int n(\mathbf{r}) \epsilon_{xc}([n(\mathbf{r})]) d\mathbf{r} \end{aligned} \quad (2.34)$$

The above equation is used to derive to obtain Kohn–Sham (KS) equations, which make DFT applicable in practice. The functional form of the Eqn. (2.34) can be written as follows:

$$E_{\text{KS}}[n] = T_s[n] + \int V_{\text{ext}} n(\mathbf{r}) d\mathbf{r} + E_H[n] + E_{\text{xc}}[n] \quad (2.35)$$

Here, V_{ext} is the external potential due to the nuclei and other external fields.

2.1.4 Kohn–Sham Equations

The previous section addressed the formulation of the KS equation and the idea of self-consistency. In DFT-based calculations, methods are classified based on their representation of the density, potential, and especially KS orbitals. The choice of representation is made to increase computational efficiency while maintaining accuracy. For a particular choice of basis set, the coefficients are the only variable to be determined (density depends on the KS orbitals). The total energy of DFT is thus variational, meaning the solution of the self-consistent KS equations requires one to determine the coefficients on the occupied orbitals that provide a minimum of the total energy.

According to the second theorem of Hohenberg and Kohn, all properties such as kinetic energy are uniquely determined if $n(\mathbf{r})$ is specified. Eqn. (2.34) shows the relationship. To minimize the total energy with respect to the KS orbitals, the variational principle is usually used. While performing the minimization, it is preferable to minimize with respect to $\phi^*(\mathbf{r})$ (both yield the same result). Using the chain rule for functional derivatives, the Eqn. (2.35) becomes:

$$\frac{\delta E}{\delta \phi_i^*(\mathbf{r})} = \frac{\delta T_s}{\delta \phi_i^*(\mathbf{r})} + \left[\frac{\delta E_{\text{ext}}}{\delta n(\mathbf{r})} + \frac{\delta E_H}{\delta n(\mathbf{r})} + \frac{\delta E_{\text{xc}}}{\delta n(\mathbf{r})} \right] \frac{\delta n(\mathbf{r})}{\delta \phi_i^*(\mathbf{r})} = 0 \quad (2.36)$$

The kinetic energy may be differentiated separately with respect to orbital. In the above equation the E_{ei} is replaced with E_{ext} which denotes the potential energy due to nuclei and any other external fields.

$$-\frac{1}{2}\nabla^2\phi_i^*(\mathbf{r}) + \left[V_{\text{ext}}(\mathbf{r}) + \int d(\mathbf{r}') \frac{n(\mathbf{r}')}{|\mathbf{r} - \mathbf{r}'|} + \epsilon_{xc}(n) + n(\mathbf{r}) \frac{\delta\epsilon_{xc}[n]}{\delta n(\mathbf{r})} \right] \phi_i(\mathbf{r}) = \epsilon_i \phi_i(\mathbf{r}) \quad (2.37)$$

Eqn. (2.37) represents the many-particle system in terms of single-particle orbitals. Each of these equations resembles a Schrödinger equation.

$$\left[\hat{T} + V_{\text{eff}} \right] \phi_i(\mathbf{r}) = \epsilon_i \phi_i(\mathbf{r}) \quad (2.38)$$

Here, the V_{eff} is the sum of the V_H , V_{xc} , and V_{ext} , which depends on the density and indirectly depends on the KS orbitals. This equation is solved self-consistently (see Fig. 2.1).

2.1.5 Kohn–Sham Problem for an Isolated Atom

For one-electron atom, the Coulombic potential, $V(\mathbf{r}) = V(r) = -Z/r$ is spherically symmetric, meaning the solution can be split into a radial and an angular part,

$$\psi_{n\ell m}(\mathbf{r}) = \psi_{n\ell}(r)Y_{\ell m}(\theta, \phi) = r^{-1}\phi_{n\ell}(r)Y_{\ell m}(\theta, \phi). \quad (2.39)$$

Here, $Y_{\ell m}(\theta, \phi)$ are normalized spherical harmonics. The wave equation reduces to the radial equation, which is associated with the principle quantum number n ,

$$-\frac{1}{2}\frac{d^2\psi_{n\ell}}{dr^2} + \left[\frac{\ell(\ell+1)}{2r^2} + V_{\text{ext}}(r) - \epsilon_{n\ell} \right] \psi_{n\ell} = 0 \quad (2.40)$$

In the Kohn–Sham approach to the many-particle system, the form of the single-particle equations is identical to the spherically-symmetric Schrödinger equation

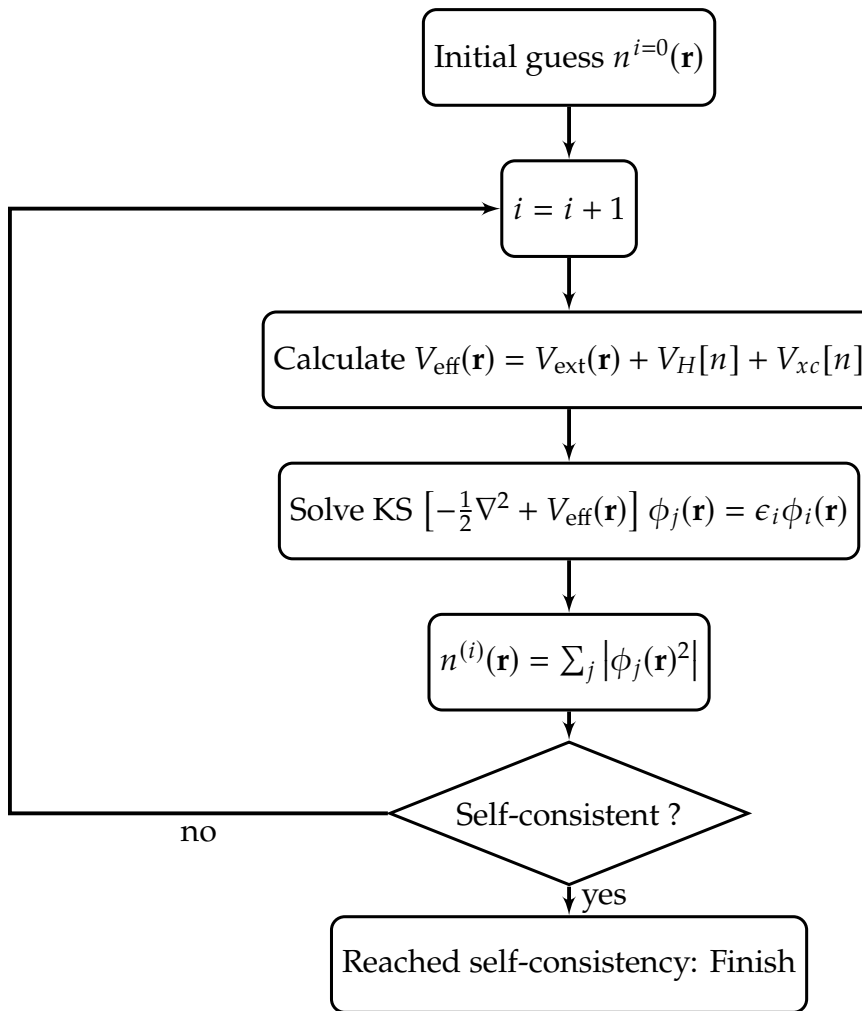


Figure 2.1. Schematic representation of the self-consistent loop solution of Kohn–Sham equations.

with an effective potential V_{eff} replacing the Coulomb potential. The effective potential ($V_{\text{eff}} = V_{\text{ext}}(r) + V_H(r) + V_{xc}(r)$) is spherically symmetric in the Kohn–Sham approach. The independent-particle Kohn–Sham states may be classified by the angular quantum numbers (ℓ, m) , and the one particle equations are analogous to the Schrödinger equation for one-electron atom.

$$-\frac{1}{2} \frac{d^2\psi_{n\ell}}{dr^2} + \left[\frac{\ell(\ell+1)}{2r^2} + V_{\text{eff}}(r) - \epsilon_{n\ell} \right] \psi_{n\ell} = 0 \quad (2.41)$$

2.1.6 Pseudopotentials

In solids, the electrons and nuclei interact strongly through the Coulomb potential. However, according to the Fermi liquid theory (FLT), electronic excitation near the Fermi energy in metals behave as though the electrons were independent particles. This leaves the strong interactions between the core electrons and the nuclei. In most cases, the core electrons are quite strongly bound and do not respond significantly to the motion of the valence electrons. Hence, they can be regarded as essentially fixed. This is the essence of the pseudopotential approximation: the strong core potential is replaced by a pseudopotential, whose shape resembles the potential associated with the all-electron wavefunction outside a certain core radius. In this way both the core states and the nodes (Fig. 2.2) in the valence wavefunctions are removed. For many metals, the pseudowavefunctions can be represented by a much smaller number of plane waves.

2.1.7 Basic Phillips–Kleinman Construction

For a given many-electron Hamiltonian, $\mathcal{H} = \hat{T} + \hat{V}$, where \hat{T} is the kinetic energy operator and \hat{V} is the potential energy operator, the core electron wavefunctions are defined by the time-independent Schrödinger equation,

$$\mathcal{H} |\psi_i\rangle = E_i |\psi_i\rangle \quad (i = 1, \dots, n_{\text{core}}) \quad (2.42)$$

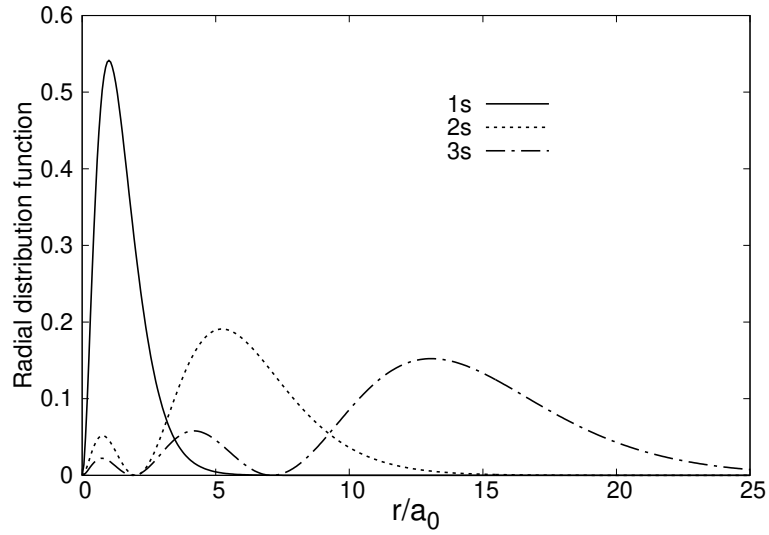


Figure 2.2. Radial distribution function of hydrogenic 1s, 2s and 3s, electron. The electron has a higher kinetic energy near the nucleus.

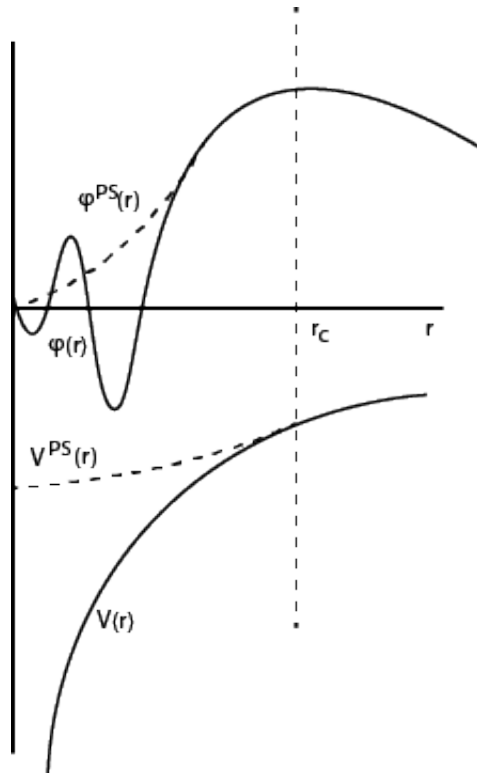


Figure 2.3. Schematic of the replacement of the all-electron wavefunction and core potentials by a pseudo-wavefunction and pseudopotential.

The valence electron wavefunction similarly can be found by the Hamiltonian

$$\mathcal{H} |\psi_v\rangle = E_v |\psi_v\rangle \quad (2.43)$$

The valence electron wavefunctions are orthogonal to the core electron wavefunctions ($\langle \psi_v | \psi_i \rangle = 0$), this orthogonality always has to be preserved, even if the core electrons are not treated explicitly. One way to preserve this orthogonality is to write the valence electron wavefunction in a basis set that is orthogonal to the core electrons. The Gram–Schmidt process can be used. Herring [6] was the first one to use orthogonalized plane waves (OPWs) (Appendix B) as basis for the first quantitative calculations of bands. Using this idea, we can orthogonalize any arbitrary basis set $\{|\chi_n\rangle\}$ to the core electron wavefunctions by defining a new basis set $\{|\varrho_n\rangle\}$ via

$$|\varrho_n\rangle = |\chi_n\rangle - \sum_{i=1}^{n_{\text{core}}} \langle \psi_i | \chi_n \rangle |\psi_i\rangle \quad (2.44)$$

Here each of the new basis set, $\{|\varrho_n\rangle\}$, satisfies $\langle \chi_n | \psi_i \rangle = 0$ for each $|\psi_i\rangle$. Now we can express the valence electron wavefunction as a linear combination of the new basis sets,

$$|\psi_v\rangle = \sum_n C_n |\varrho_n\rangle. \quad (2.45)$$

Inserting Eqn. (2.44) into Eqn. (2.45), the valence electron wavefunction can be expressed in the following way. The orthogonality condition with the core electrons is still valid,

$$|\psi_v\rangle = \sum_n C_n \left[|\chi_n\rangle - \sum_{i=1}^{n_{\text{core}}} |\psi_i\rangle \langle \psi_i | \chi_n \rangle \right] = |\phi\rangle - \hat{\Omega} |\phi\rangle, \quad (2.46)$$

Here, $\hat{\Omega}$ is a projection operator for the core electron wavefunction

$$\hat{\Omega} = \sum_{i=n}^{n_{\text{core}}} |\psi_i\rangle\langle\psi_i| \quad (2.47)$$

and a new wavefunction which is a linear combination of $|\chi_n\rangle$, sometime designated as pseudo-orbital,

$$|\phi\rangle = \sum_n C_n |\chi_n\rangle \quad (2.48)$$

This technique of representing the valence electron wavefunction in preorthogonalized basis set has been studied and used as a computational tool [6]. It took the insight of the Phillips and Kleinman [7]. The new pseudo-orbital satisfies the orthogonality condition, but they also change the Hamiltonian so that the eigenvalues are the same as they would be with the valence electrons. Mathematically, it can be obtained by replacing original valence electron Hamiltonian (Eqn. (2.43)) with the newly obtained pseudo-wavefunction yields

$$\mathcal{H}|\psi_v\rangle = \mathcal{H}\left[|\phi\rangle - \sum_n |\psi_i\rangle\langle\psi_i|\phi\rangle\right] = E_v\left[|\phi\rangle - \sum_n |\psi_i\rangle\langle\psi_i|\phi\rangle\right] \quad (2.49)$$

Rearranging Eqn. (2.49) provides a new effective Hamiltonian,

$$\left[\mathcal{H} + \sum_n^{n_{\text{core}}} (E_v - E_i) |\psi_i\rangle\langle\psi_i|\right] |\phi\rangle = E_v |\phi\rangle \quad (2.50)$$

The above equation has the form of the original valence electron eigenvalue problem (2.43), but with an extra term for orthogonalization. This extra potential ($V_{n\ell} = \sum_n^{n_{\text{core}}} |\psi_i\rangle\langle\psi_i|$), is a non-local operator, and the pseudo-orbital ($|\phi\rangle$) is an eigenstate of the new effective Hamiltonian, $\mathcal{H} + V_{n\ell}$. The new Hamiltonian has an extra potential $V_{n\ell}$, which depends on the angular momentum ℓ due to the spherical symmetry. Because of its spherical symmetry, each angular momentum

(ℓ, m) combination can be treated separately. The dependence on ℓ means that a pseudopotential is a non-local operator, can be written in “semilocal” (SL) form:

$$\hat{V}_{SL} = \sum_{\ell m} |Y_{\ell m}\rangle V_\ell(r) \langle Y_{\ell m}|, \quad (2.51)$$

where $Y_{\ell m}(\theta, \phi) = P_\ell(\cos(\theta))e^{im\phi}$ and P_l is a Legendre polynomial. It is semi-local because it is non local on the angular variables but local in the radial variable.

The sophistication and accuracy of pseudopotentials have evolved considerably since the Phillips–Kleinman construction. This development produces many methods of generating pseudopotentials. All of these methods have the following goals: (1) the pseudopotential should be as soft as possible so that it can allow representation of pseudo-wavefunctions with fewer plane waves; (2) transferability has to be maintained, meaning a generated pseudopotential generated to match certain properties should produce other properties accurately; and (3) the pseudo-charge density should reproduce the valence charge density as accurately as possible.

2.1.8 Norm-Conserving Pseudopotentials

Hamann, Schlüter, and Chiang [8] developed the concept of norm-conservation, which was a first step in fulfilling all the aforementioned requirements. As the exchange–correlation energy of the electronic system depends on the electron density, it is necessary that the real and pseudo wavefunctions be identical outside the core region. In the outer region ($r > r_c$), both functions coincide. Therefore, the total charge density created in the core region ($r < r_c$) must be the same,

$$\int_0^{r_c} \psi_{ae}^*(r)\psi_{ae}(r)dr = \int_0^{r_c} \psi_{ps}^*(r)\psi_{ps}(r)dr \quad (2.52)$$

Where $\psi_{ae}(r)$ is the all-electron wavefunction and ψ_{ps} is the pseudo-wavefunction. The logarithmic derivatives of the real and pseudo-wavefunction and their energy

derivatives agree in the outer region. These types of pseudopotentials are the most transferable because they are able to reproduce the scattering properties of ions in different chemical environments [8]. The downside of norm-conserving pseudopotentials is a higher cutoff radius and thus increased memory and CPU requirements. Troullier and Martins [9] developed a more effective method to generate norm-conserving pseudopotentials for practical calculations.

2.1.9 Ultrasoft Pseudopotentials (US)

The norm conservation requirement necessitates a very high of cutoff energy for the plane-wave basis set. In particular, the tightly-bound orbitals have a substantial fraction of their weight inside the core region of the atom. There are some important cases in which it is impossible to construct a pseudopotential that allows a significant reduction of the cutoff energy. Vanderbilt [10] suggested relaxing the norm conservation criteria in favor of a smoother (*i.e.*, softer) pseudopotential. The resulting ultrasoft pseudopotentials are difficult to construct and require extensive testing [11].

2.1.10 Projector Augmented Wave Method (PAW)

The electronic wavefunctions oscillate wildly near the nuclei (Fig. 2.2) than the valence electrons between the atoms. Expanding the core electrons using plane-wave creates computational challenges. Augmented-wave methods uses the separation of the wavefunctions in two regions to address this issue. The first part is partial wave expansion inside an atom-centered sphere called the augmentation region and a plane wave expansion outside. Both expansions are continuously differentiable at the boundary.

Blöchl [12] suggested that there is a linear transformation from the all-electron to the pseudo-wavefunctions. The transformation is as follows:

$$|\psi\rangle = |\tilde{\psi}\rangle + \sum_i \left(|\phi_i\rangle - |\tilde{\phi}_i\rangle \right) \langle \tilde{p}_i | \tilde{\psi} \rangle \quad (2.53)$$

Here ϕ_i are the partial waves within the augmentation regions and $\langle \tilde{p}_i |$ is a projector that satisfies the condition $\langle \tilde{p}_i | \tilde{\phi}_j \rangle = \delta_{ij}$. The tilde quantities are related to the pseudo representation. Kresse and Joubert [11] showed a connection between PAW and ultrasoft pseudopotential (US-pp) and how the PAW method can be implemented into existing code.

References

1. D. R. Hartree, in *Proc. Camb. Phil. Soc.*, Vol. 24 (Cambridge University Press, 1928) p. 89.
2. V. Fock, *Z. Phys.* **61**, 126 (1930).
3. L. H. Thomas, in *Proc. Camb. Phil. Soc.*, Vol. 23 (Cambridge University Press, 1927) pp. 542–548.
4. E. Fermi, *Rend. Accad. Naz. Lincei* **6**, 602 (1927).
5. P. Hohenberg and W. Kohn, *Phys. Rev.* **136**, B864 (1964).
6. C. Herring, *Phys. Rev.* **57**, 1169 (1940).
7. J. C. Phillips and L. Kleinman, *Phys. Rev.* **116**, 287 (1959).
8. D. R. Hamann, M. Schlüter, and C. Chiang, *Phys. Rev. Lett.* **43**, 1494 (1979).
9. N. Troullier and J. L. Martins, *Phys. Rev. B* **43**, 1993 (1991).
10. D. Vanderbilt, *Phys. Rev. B* **41**, 7892 (1990).
11. G. Kresse and D. Joubert, *Phys. Rev. B* **59**, 1758 (1999).
12. P. E. Blöchl, *Phys. Rev. B* **50**, 17953 (1994).

CHAPTER 3

ESTIMATION OF EFFECTIVE THERMAL CONDUCTIVITY IN U-10Mo FUELS WITH DISTRIBUTED XENON GAS BUBBLES

This chapter was published as an article in the Journal of Nuclear Materials. The authors of that article are A. Rafi M. Iasir and Karl D. Hammond of the University of Missouri and Nickie J. Peters of the University of Missouri Research Reactor Center.

3.1 Introduction

The Reduced Enrichment for Research and Test Reactors (RERTR) [1] program was initiated in the USA in the late 1970s to develop new nuclear fission fuels to replace high-enrichment uranium (HEU). The development of low-enrichment uranium (LEU) fuels for high-performance reactors is an important nonproliferation initiative [1]. One of the main requirements of LEU fuels is increased uranium density, such as that found in metallic uranium, to offset the decrease in ^{235}U enrichment. Metallic uranium is thought to have sufficient density, but the orthorhombic crystal structure of α -uranium and the anisotropic fuel swelling that results make it unattractive as a fuel. Uranium alloys that retain the high-temperature γ -phase, which is body-centered cubic, are more suitable for reactor fuel due to their more isotropic radiation-induced swelling behavior compared with α -uranium [2].

Various uranium alloys have been tested as alternative metallic fuels under reactor operating conditions, including U_6Fe and U_6Mn [3, 4]. Elements such as molybdenum (Mo), niobium (Nb), titanium (Ti), and zirconium (Zr) have also

been tried as alloying elements because of their solubility in γ -uranium [5–7]. Molybdenum stabilizes uranium’s γ -phase at concentrations near the eutectoid point, lowering the phase transition temperature from 776 °C for pure uranium (corresponding to the β – γ allotropic point) to the eutectoid point of 555 °C for 11.1 percent molybdenum in γ -uranium by weight [8, 9]. To take advantage of this, uranium alloyed with 10 wt% molybdenum (U-10Mo) is currently being developed as a potential high-density LEU fuel for high-performance research reactors.

The two major fuel types are U–Mo/Al dispersion fuels (U–Mo grains dispersed in an aluminum matrix) and U–Mo monolithic fuels [10]. Dispersion fuels show poor irradiation performance due to fuel–matrix interaction, which causes break-away swelling behavior at intermediate burnup [11–13]. In monolithic fuels, a zirconium foil is used as a diffusion barrier between the fuel and the cladding (aluminum) to prevent diffusion of molybdenum into the cladding [14].

Thermal conductivity is an important property of any nuclear fuel, since most of the important physical properties are temperature-dependent. In the case of high-performance reactors, fuels must undergo high fission density at relatively low temperatures. For this reason, research reactor fuels are designed for efficient heat rejection. During test operations, Burkes and coworkers [15] observed that the thermal conductivity in monolithic fuels decreased significantly with increased burnup. For a fission density of 3.30×10^{21} fissions/cm³ at 200 °C, thermal conductivity decreased by approximately 30%; at 4.53×10^{21} fissions/cm³, conductivity decreased by 45% [15].

Fission also creates a variety of fission products, which result in gas bubbles, metallic precipitates, and solutes in the fuel matrix [16]. These fission products, in addition to radiation damage in reactor environments, result in complex microstructural evolution that restructures the nuclear fuel over time. Fission gas bubbles are particularly problematic, as they cause changes in thermal conductiv-

ity and swelling of the fuel. In addition, ^{135}Xe is a potent neutron absorber. Solid fission products (e.g., Sr, Y, Zr, La, Ce, and Nd) are also constantly being produced; these elements can form intermetallic alloys, which can increase the volume of the fuel and reduce the thermal diffusivity [17, 18]. These solid fission products also play an important role in the thermal stability of fission gas bubbles [19].

For every four fission events, an average of one inert gas atom (xenon or krypton) is produced. The dominant gaseous species is xenon, accounting for almost 85% of fission gas [20, 21]. Xenon atoms in U–Mo alloy fuels have a strong tendency to precipitate into small bubbles due to their low solubility. The formation and growth of gas bubbles inside irradiated nuclear fuels has technical importance, as bubbles influence the microstructure of the material [22]. Recent TEM and SEM images show that fission bubbles in U–10Mo distribute themselves in both inter-granular and intra-granular formations [23–26]. High-fission-density fuels show randomly-distributed, micrometer-sized fission gas bubbles distributed throughout the grains [25]. Inter-granular bubble density increases with burnup.

Inside the micrometer-sized grains, fission gas forms superlattices [23–25], similar to those seen in ion-irradiated materials [27–36]. Typical bubble sizes are 2–6 nm in diameter, and the distance between the bubbles is typically in the 4–12 nm range. The superlattice usually has the same crystal structure as the host material, but an exception exists: the superlattice in U–10Mo shows a face-centered cubic structure in a body-centered cubic matrix. An ion-irradiated bubble superlattice has a lattice parameter of tens of nanometers [23]; that of fission gas bubbles is typically similar [37]. The superlattice forms in ion-irradiated materials between approximately $0.15T_m$ and $0.35T_m$ [34], which is within the typical anticipated operating range of U–Mo fuels, and the superlattice in U–10Mo can survive temperatures up to approximately 850 °C [37].

The thermal conductivity of a monolithic U–Mo fuel plate is at a maximum prior to irradiation [15]. Inclusions and porosity change the thermal and the electrical conductivity of many materials [38]. Solid fission products usually have minimal impact on overall thermal conductivity, as their conductivities are similar to the conductivity of the fuel. Gases, on the other hand, have much lower thermal conductivity than the matrix, and typically have much lower densities and heat capacities as well. Various models, both empirical and theoretical, have been proposed to describe the changes in conductivity due to gas bubbles. Maxwell [39] was among the first to derive an expression for the effective thermal conductivity of heterogeneous media; his model assumed a uniform distribution of spherical particles in a matrix. A few other empirical models also exist [40–42]; unfortunately, the large diversity of pore shape, pore size, and type of included material inside nuclear fuel make it impossible to describe heat transfer with a single equation. Several theoretical models have been proposed to describe the influence of porosity and inclusions on the thermal conductivity [39, 43–46]. These theoretical models usually assume pores with regular geometric shapes and that the pore arrangement is sufficiently dilute so as to neglect interaction between inclusions.

The microstructure of irradiated nuclear fuels is very complicated due to the lack of consistency between bubbles. The intra-granular gas bubbles are two or three orders of magnitude smaller than the inter-granular gas bubbles [47]. The shapes of the bubbles are also highly variable: the intra-granular gas bubbles are approximately spherical, whereas inter-granular gas bubbles do not have consistent shapes. In this work, we assess contributions to the thermal conductivity of U-10Mo from both inter- and intra-granular gas bubbles. The impact of xenon bubble pressure on the overall thermal conductivity is also estimated. Because fission gas is typically a mixture of krypton and xenon, rather than pure xenon, we include

two comparisons with a krypton–xenon mixture. At the end, we present a study of the influence of different bubble arrangements on the overall thermal conductivity.

3.2 Methods

A finite element model was used to solve the steady-state heat conduction equation in the presence of various microstructures. Two types of microstructures containing xenon gas bubbles were used: a xenon bubble superlattice structure representing intra-granular bubbles, and a grain boundary structure representing inter-granular bubbles. Figure 3.1 shows an example of an intra-granular bubble distribution, while Figure 3.2 shows the inter-granular bubble distribution. In the intra-granular bubble case, xenon gas bubbles were placed in a variety of spatial configurations, including configurations consistent with a gas bubble superlattice. All simulations were performed in a two-dimensional domain. The gas bubble superlattice structure was created based on data from Miller *et al.* [23]. According to Miller *et al.* [23], the bubble size inside the grain boundary superlattice structure is normally distributed. Based on their experimental values, we chose four bubble diameters to create our simulation. Because the superlattice in U-10Mo is FCC, the two-dimensional structure of bubbles was created based on the FCC structure with a 12 nm lattice parameter, which was also taken from Miller *et al.* [23]. The bubble sizes were randomly sampled from this distribution using the discrete values of 3.1, 3.6, 3.75, and 4.0 nm in diameter. The square domain’s dimensions were 80 nm × 80 nm, which results in 85 bubbles with a lattice constant of 12 nm. Triangular elements were used to create the mesh using the Trellis Pro software package [48].

In the inter-granular bubble case, the grain boundary structure of U-10Mo was created based on images from Miller *et al.* [24]. Their SEM (scanning electron micrograph) of a focused ion beam (FIB) cross-section showed fission gas bubbles

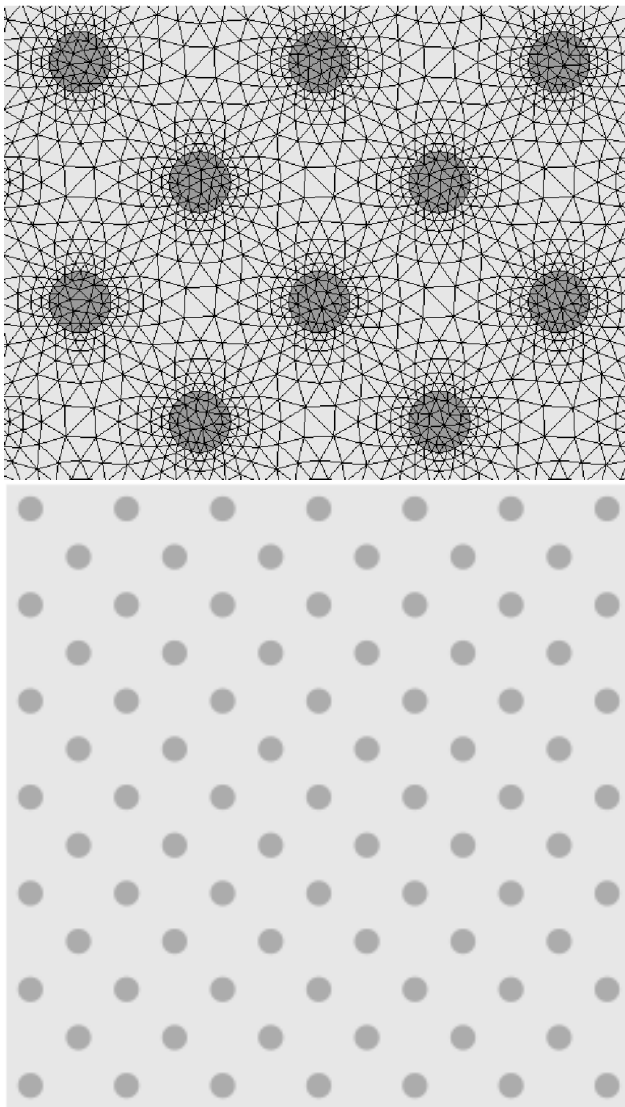


Figure 3.1. (a) Discretized domain of intra-granular xenon bubbles inside a U-10Mo matrix; (b) Example two-dimensional bubble distribution used for intra-granular xenon gas, consisting of bubbles with 3.1, 3.6, 3.75, and 4.0 nm diameters, consistent with the work of Miller and coworkers [23]. The lattice parameter for the gas bubble superlattice is 12.0 nm.

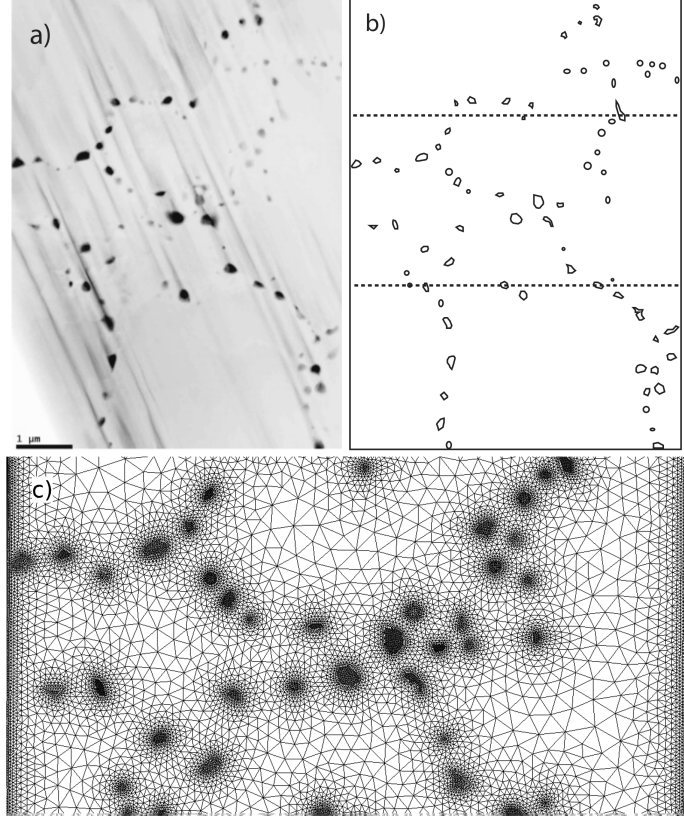


Figure 3.2. (a) SEM image of the fission gas bubbles along the grain boundaries from Miller *et al.* [24] used for FEM calculations (b) Geometry created based on the grain boundary fission gas image in (a) (c) FEM mesh with grain boundary fission gas of the region between the dotted line in (b).

populating the grain boundaries, as shown in Figure 3.2. This domain was also discretized with triangular elements. The top and bottom boundaries of the domain of the FEM domain were assumed to be adiabatic. The left and right boundaries have fixed-temperature boundary conditions applied. This temperature difference drives the heat flow.

The thermal conductivity of U-10Mo was estimated from a linear fit of thermal conductivity as a function of temperature between 298 K and 1073 K from Kaufmann [50]. Burkes *et al.* [51] also provided a linear fit of the U-10Mo thermal conductivity as a function of temperature up to 873 K; their results were in good agreement with Kaufmann's [50]. Xenon conductivity is drawn from the

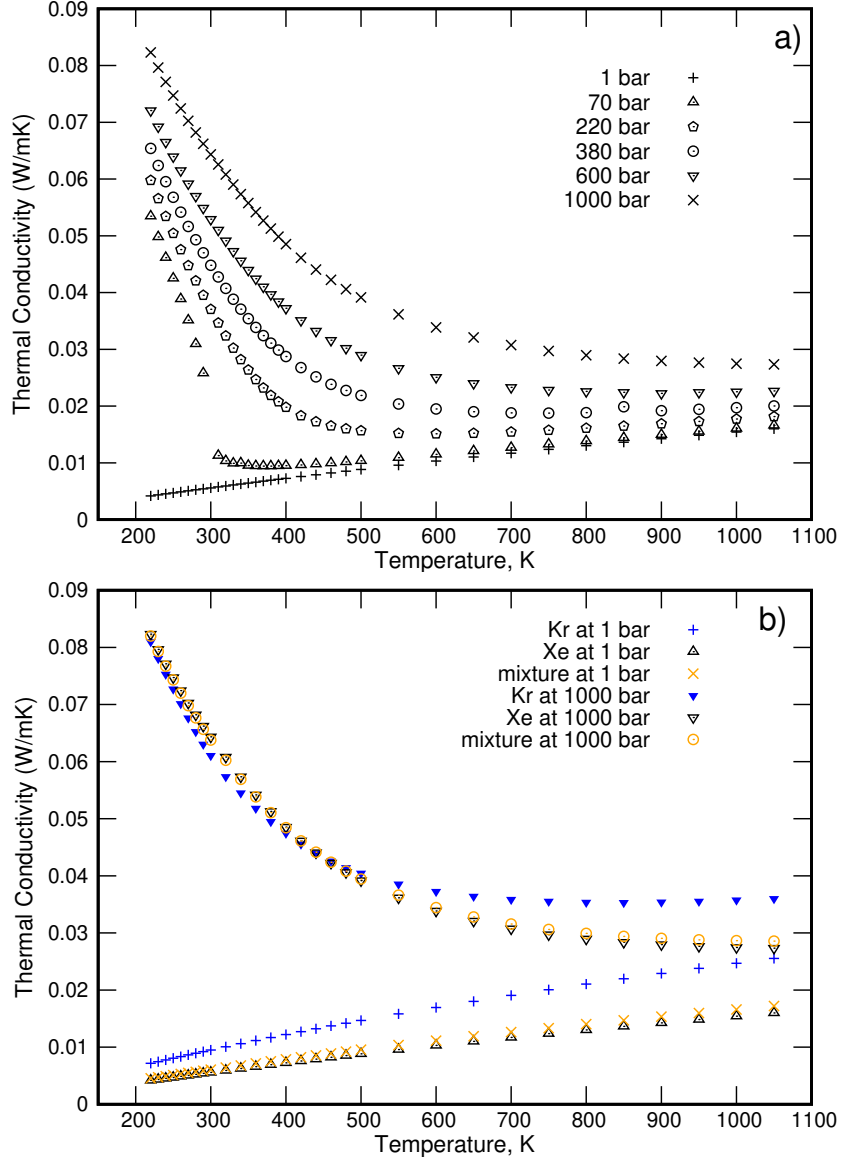


Figure 3.3. (a) Thermal conductivity of xenon as a function of pressure and temperature based on the measurements of Rabinovich et al. [49]. Note that the critical point of xenon is 289.733 K and 58.42 bar; this is why there is such a drastic change in conductivity at low temperature between the 1 bar and 70 bar isobars. (b) Comparison between the thermal conductivities of pure krypton and pure xenon (both at 1 bar and at 1000 bar) with a mixture of 15% krypton and 85% xenon at both 1 bar and 1000 bar. This composition is representative of fission gas.

data of Rabinovich *et al.* [49]; the thermal conductivity of xenon depends on both temperature and pressure, as shown in Figure 3.3. The pressure inside a bubble depends on the radius of the bubble, the surface tension, the magnitude of the Burgers vector, and the shear modulus of the host material [52, 53]. According to Xiao *et al.* [54], the pressure inside a xenon bubble can be as high as 120 kbar. Such high pressures suggest the possibility of forming solid xenon bubbles inside the fuel [55–57]. Unfortunately, thermal conductivity data for xenon above 1000 bar are not available, so we chose two limiting sets of thermal conductivity data: 1 bar and 1000 bar. For each set of data, a polynomial fit (fifth order) was used to interpolate the conductivity over the temperature range. Fission gas is typically a mixture of krypton and xenon, so we ran simulations in which the bubbles were filled with 15% krypton, 85% xenon (molar basis), with conductivity data for krypton from Rabinovich *et al.* [49]. The mixture’s thermal conductivity was calculated using Wilke’s mixing rule [58], which uses the full first-order Chapman–Enskog relation along with Eucken’s relation for the thermal conductivities [59, 60]. Using Wilke’s approach, the mixture’s thermal conductivity is given by

$$K = \sum_i \frac{x_i K_i}{\sum_j x_j \phi_{ij}}, \quad (3.1)$$

where x_i is the mole fraction and K_i is the conductivity of the pure component. The coefficients ϕ_{ij} can be calculated by the following relation [60]:

$$\phi_{ij} = \frac{\left[1 + \left(\frac{\mu_i}{\mu_j} \right)^{1/2} \left(\frac{M_j}{M_i} \right)^{1/4} \right]^2}{\left[8 \left(1 + \frac{M_i}{M_j} \right) \right]^{1/2}}, \quad (3.2)$$

where M_i is the molar mass of the species and μ_i is the viscosity.

3.2.1 Effective Thermal Conductivity Calculation

The temperature in a composite material in the absence of heat sources is described by the heat equation:

$$\nabla \cdot (K\nabla T) = 0, \quad (3.3)$$

where $K(x, y) = \chi_1(x, y)K_1 + \chi_2(x, y)K_2$ is the thermal conductivity tensor, T is the temperature, K_i ($i = 1$ for the matrix and 2 for the bubble) is the thermal conductivity tensor, and $\chi_i(x, y)$ is the indicator function of phase i . The local heat flux can be calculated using the equation

$$q''(x, y) = -K(x, y) \cdot \nabla T(x, y), \quad (3.4)$$

where $q''(x, y)$ is the local heat flux vector and $\nabla T(x, y)$ is the local temperature gradient. The local temperature and heat flux are calculated by solving Equations (3.3) and (3.4). The components of the effective thermal conductivity tensors are calculated via

$$K_{\text{eff}}^x = -q_x'' \left\langle \frac{\partial x}{\partial T} \right\rangle. \quad (3.5)$$

Where q_x'' is the mean heat flux in the x -direction, and $\left\langle \frac{\partial x}{\partial T} \right\rangle$ is the average inverse temperature gradient in the x -direction. The MOOSE Framework [61] was used to solve Equation (3.3) with Dirichlet boundary conditions at $x = 0$ and $x = L$ and Neumann (adiabatic) boundary conditions at $y = 0$ and $y = L$. The effective thermal conductivity was calculated using Equation (3.5).

3.3 Results and Discussion

3.3.1 Effect of Xenon Gas Bubbles on the Thermal Conductivity

We examined two broad categories of bubbles: inter-granular bubbles (*i.e.*, bubbles that collect at grain boundaries) and intra-granular bubbles. The intra-

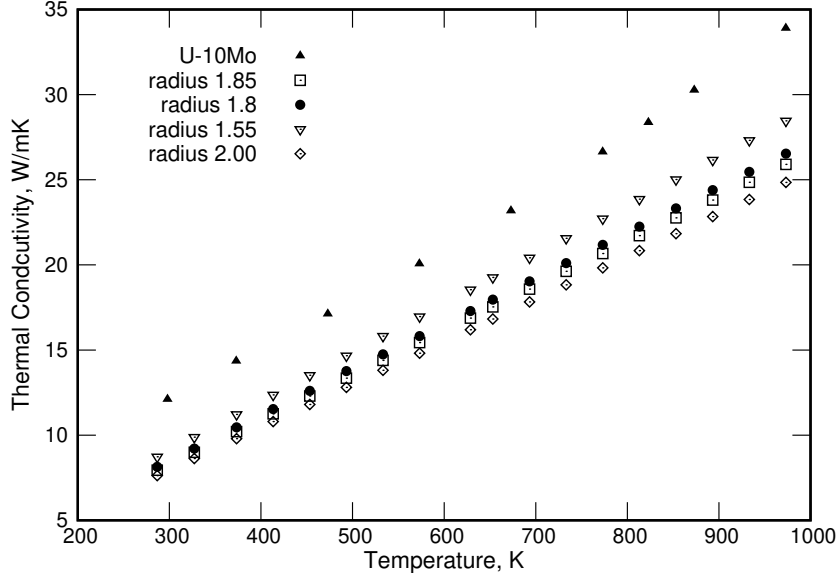


Figure 3.4. Comparison between the thermal conductivity of U-10Mo (from Kaufmann [50]) to the effective thermal conductivity of U-10Mo with intra-granular xenon bubbles of different diameters as arranged in Figure 3.1b.

granular case is intended to represent the effect of a gas bubble superlattice (GBS) on the conductivity. We will discuss each case in turn.

3.3.1.1 Intra-Granular Bubbles

A two-dimensional representation of a gas bubble superlattice, as shown in Figure 3.1, was used to simulate the effect of intra-granular bubbles on the thermal conductivity. Five different bubble sizes were used, each with the same superlattice constant (resulting in the same center–center distance between bubbles). Figure 3.4 shows the effective thermal conductivity due to the xenon bubble distribution in the intra-granular region. As is clear from Figure 3.4, the thermal conductivity decreases with increasing bubble size, and is 20–40 percent lower in all cases than it is for bubble-free U-10Mo. In these simulations, the thermal conductivity of xenon was assumed constant at its 1 bar value (it is still a function of temperature). Figure 3.5 shows the result of the finite element method solution compared with the

theoretical solution for porous materials' thermal conductivity from the Maxwell–Eucken equation [39],

$$\lambda = \lambda_s \frac{\lambda_p + 2\lambda_s + 2\nu_p(\lambda_p - \lambda_s)}{\lambda_p + 2\lambda_s - \nu_p(\lambda_p - \lambda_s)}, \quad (3.6)$$

where λ is the effective thermal conductivity of the fuel, λ_s is the thermal conductivity of the continuous phase (U-10Mo), λ_p is the thermal conductivity of the dispersed phase (xenon bubble), ν_p is the volume fraction of the dispersed phase (*i.e.*, the volume fraction of xenon in U-10Mo). Equation (3.6) assumes the pore volume fraction is less than 15 percent, that the pores are dispersed uniformly in the solid, and that the distance between the pores is large enough that they do not interact [62, 63]. The result is also compared with the Hashin–Shtrikman upper bound, which is based on a theoretical expression derived for the magnetic permeability of a multiphase material [64],

$$\lambda = \frac{1}{4} \left[\lambda_p(3\nu_p - 1) + \lambda_s(2 - 3\nu_p) + \left([\lambda_p(3\nu_p - 1) + \lambda_s(2 - 3\nu_p)]^2 + 8\lambda_s\lambda_p \right)^{\frac{1}{2}} \right]. \quad (3.7)$$

Figure 3.5 shows the effect of distributed gas bubbles in the intra-granular region (grain boundary bubbles were not included). Both theoretical models over-predict the conductivity by 5–10 percent, and the absolute error increases with temperature.

3.3.1.2 Inter-Granular Bubbles

Inter-granular fission gas bubbles are associated with bubbles that collect on or near grain boundaries. Bubbles are naturally drawn to grain boundaries because of the excess volume that accompanies grain boundaries, as well as the decreased energy associated with void formation at grain boundaries relative to the bulk.

To evaluate the effect of inter-granular fission gas on the overall thermal conductivity, Figure 3.2b was used as the simulation domain. As can be seen in Figure 3.2,

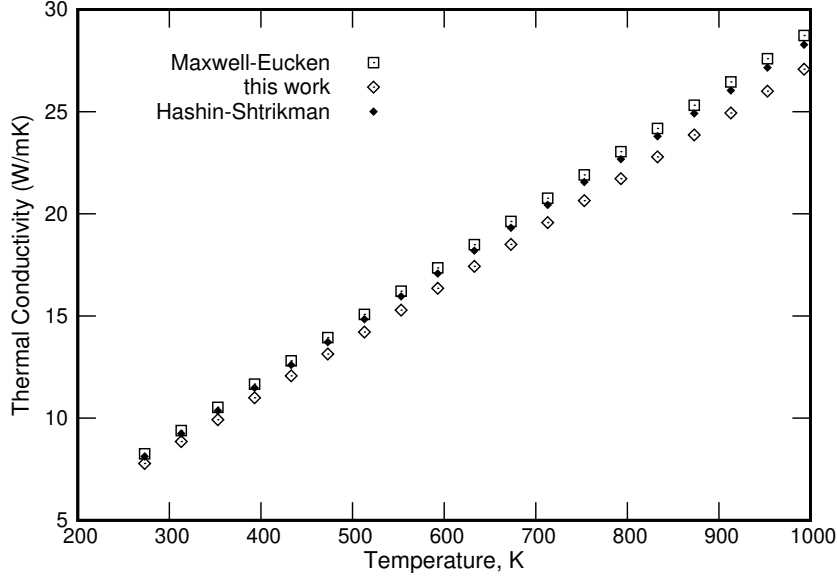


Figure 3.5. Comparison of the calculated effective thermal conductivity of U-10Mo with intra-granular xenon bubble (radius 1.55 nm, 10% porosity) with the Maxwell–Eucken [39] and Hashin–Shtrikman [64] models. In all cases, we find that the two theoretical models over-predict the thermal conductivity by about 5–10 percent compared with the numerical solution.

fission gas bubbles trapped on grain boundaries do not have consistent shapes. Note that this is only a snapshot in time of the grain structure: as burnup increases, the stress in the fuel changes, more fission gas is evolved, and the grains can rotate and change shape. For simplicity, the thermal conductivity values at 1 bar were used for xenon. It should be noted that this only includes the effect of the bubbles gathered at the grain boundary: effects on the conductivity associated with the grain boundaries themselves, which will result in changes in the conductivity because of phonon scattering effects (which are a minor contribution to thermal conductivity in metals), as well as any effects associated with U–Mo segregation at the grain boundary, are neglected in this model.

The presence of these (intra- and inter-granular) xenon bubbles decreased the thermal conductivity by more than 25 percent, as shown in Figure 3.6. According to Miller *et al.* [24], their sample (on which our simulations are based) went

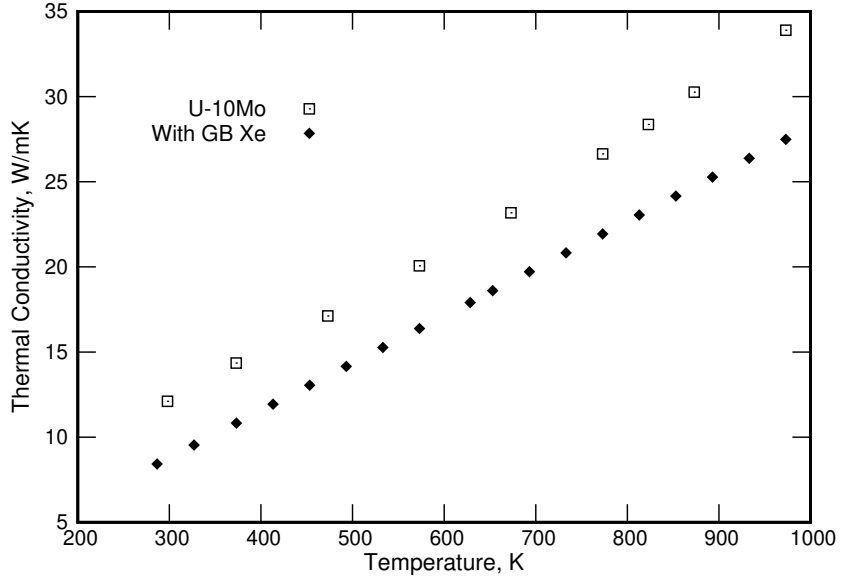


Figure 3.6. Comparison between the thermal conductivity of bubble-free U-10Mo with that of U-10Mo that has xenon bubbles decorating the grain boundaries according to the distribution in Figure 3.2. A 4% drop is observed, increasing with temperature.

through a fission density of 3.46×10^{21} fission/cm³. At this fission density, Burkes and coworkers [15] found that the experimental thermal conductivity of U-10Mo reduced to almost 33 percent of its unirradiated value at 473 K. It should be noted that the real material has a three-dimensional grain boundary structure with varying levels of fission gas at each cross section, meaning our estimates of the thermal conductivity (which effectively assume rod-like inclusions rather than spheres) will be too low. Past studies [38, 65] have indicated that conductivity in the presence of inclusions is underestimated in two-dimensional models. This suggests that the measured conductivity (33% of the conductivity of the unirradiated material) may be reasonably consistent with the conductivity estimated here (*i.e.*, 25% of the conductivity of the unirradiated material).

3.3.2 Effect of Xenon Pressure on the Overall Thermal Conductivity

To evaluate the impact of the pressure of the xenon bubbles on the overall thermal conductivity, we performed a study of the overall conductivity as a function of temperature for five different xenon bubble pressures given a fixed bubble distribution (Figure 3.1b). Each pressure has a distinct thermal conductivity (Figure 3.3) as a function of temperature. In this part of the study, a constant bubble size was used (radius 1.55 nm). The results are shown in Figure 3.7. The results show little to no change of the overall thermal conductivity of the fuel due to the bubbles' pressure over the range studied. However, though xenon has a wide range of thermal conductivities at different pressures (see Figure 3.3), the effect is negligible relative to the thermal conductivity of the fuel.

Also shown in Figure 3.7 is the overall conductivity of the system in Figure 3.1b for bubbles filled with an 85% xenon, 15% krypton mixture, with the mixture's conductivity given by Equation (3.1), using pure-component conductivities at both 1 bar and 1000 bar. The overall conductivity is nearly identical in all cases, indicating that the overall conductivity is not a strong function of pressure or composition under these conditions.

3.3.3 Effect of Bubble Arrangement on Thermal Conductivity

We performed a series of simulations to determine whether bubble distribution has a significant influence on the overall thermal conductivity. Two cases were considered. In the first case, we used same number (16) of bubbles of the same diameter (1 nm) and organized them into five different arrangements. The arrangements are arbitrary, but each has the same area fraction of bubbles (xenon gas). In the first arrangement (Figure 3.8a), the bubbles are dispersed uniformly throughout the domain. In Figure 3.8b, the bubbles are arranged in a denser pattern with bubble-free portions near the high-temperature side. In Figure 3.8c, the bubbles

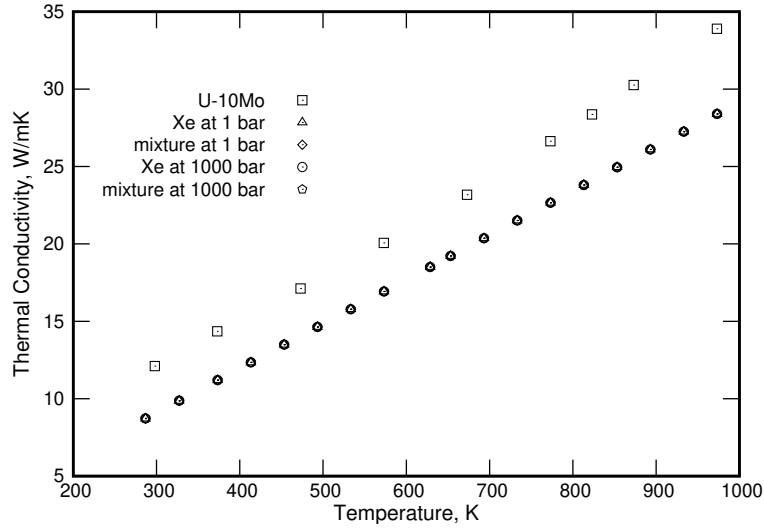


Figure 3.7. Overall thermal conductivity of U-10Mo using the thermal conductivity of xenon at two extremes of pressure (1 bar and 1000 bar), compared to that of pure (bubble-free) U-10Mo. Bubbles are distributed as in Figure 3.1b with radii of 1.55 nm. Also shown for reference is the effective thermal conductivity that would result from the same bubbles filled with a 15 atom% krypton, 85 atom% xenon mixture (representative of fission gas) at both 1 bar and 1000 bar.

are arranged in one corner. In Figure 3.8d, the bubbles are tightly clustered near the center of the domain, creating significant bubble-free regions at the top and bottom. The overall thermal conductivities for these arrangements are presented in Figure 3.9. In these simulations, heat is flowing from left to right, whereas the top and bottom boundaries are insulating (adiabatic).

Based on the results from Figure 3.8, arrangement (d) shows a minor deviation, particularly at high temperatures, compared to the other arrangements. The other four bubble arrangements do not produce significantly different thermal conductivities. The reason for the deviation for case (d) is the relatively wide “heat channel” in the direction of the heat flow, which is absent in the other arrangements. The highest thermal conductivity difference between Figure 3.8d and the other arrangements is approximately 0.93 W/m·K, which is also a function of the open channel’s area.

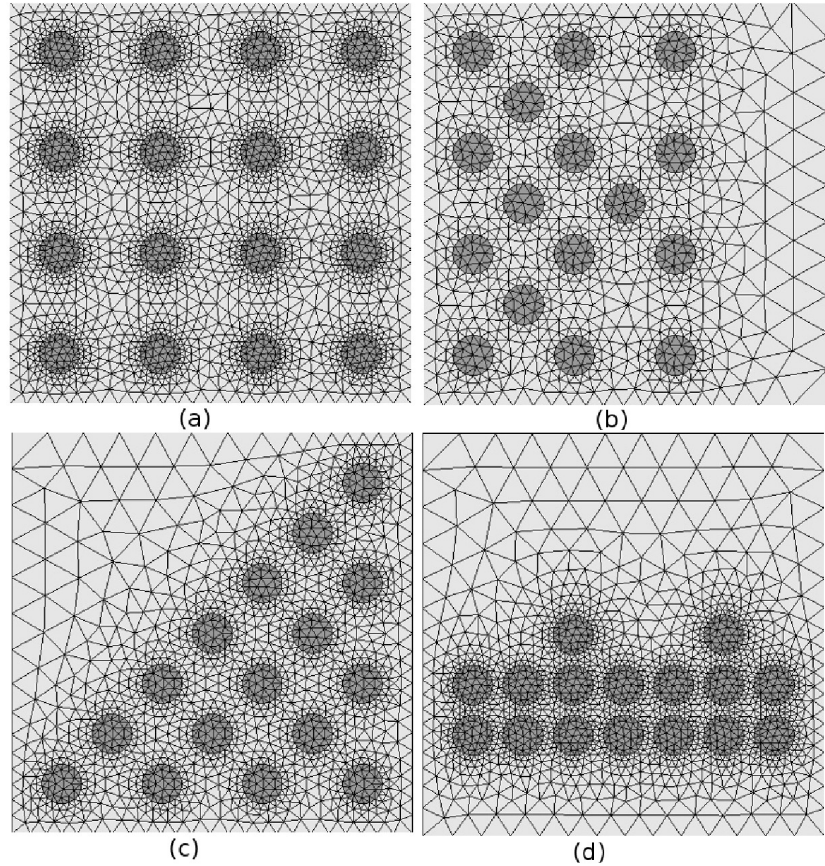


Figure 3.8. Different bubble arrangements in which the area of each bubble and the number of bubbles are the same. Heat flows from left to right in these simulations; only arrangement (d), with its uninterrupted “heat channel” in the top half of the domain, shows significantly different conductivity.

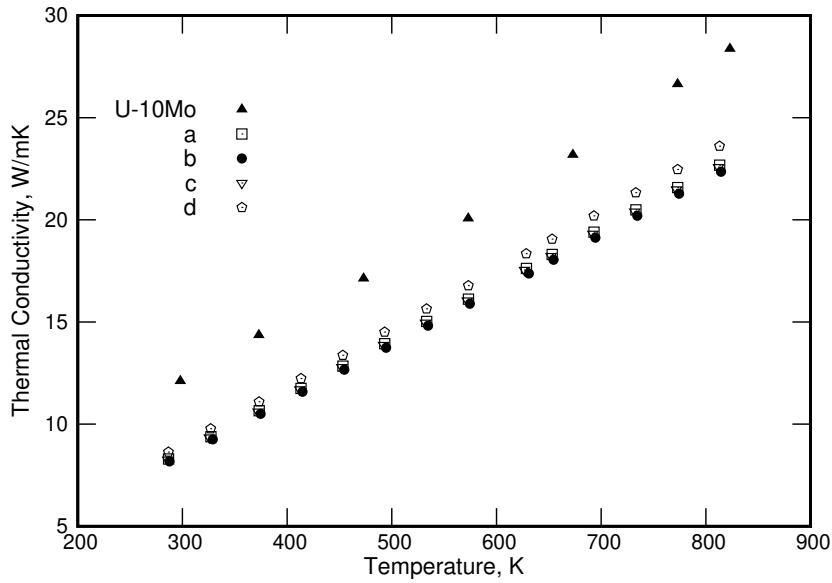


Figure 3.9. Comparison of the calculated thermal conductivity of different bubble arrangements (constant bubble area and diameter corresponding to Fig. 3.8). Only arrangement (d), with its properly-oriented “heat channel,” shows significant differences from the others, and such differences are relatively insignificant compared to the bubble-free conductivity.

In the second case, different bubble sizes were used with constant total area. As the first case shows, bubble arrangement has minimal impact on the overall heat transfer unless it produces a significant heat transfer channel in direction of the heat flow. In this step, we kept the total area covered by the bubbles the same, but with different sizes of bubbles. To keep the area same while decreasing the bubble diameter, the number of bubbles increases. Figure 3.10 shows the four different arrangements with different bubble sizes. None of the arrangements creates a heat transfer channel in the direction of heat flow. The results are shown in Figure 3.11. The results show no significant change in the overall thermal conductivity. We conclude that the bubble arrangement has little impact unless it produces a significant bubble-free heat transfer channel.

In our calculation, grain boundary xenon gas bubbles had very minimal impact on the overall heat transfer. That is because our sample has very low grain boundary

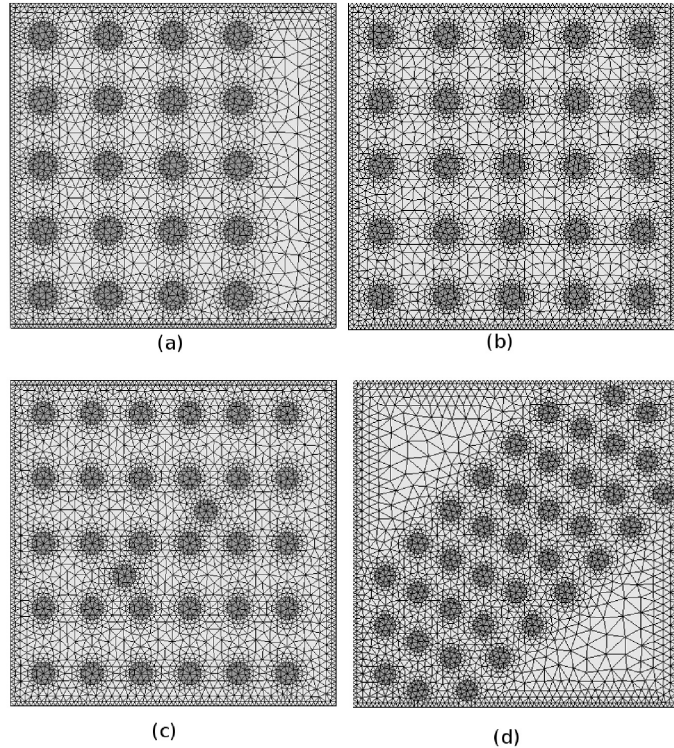


Figure 3.10. Different bubble arrangements where the area is the same but the bubbles have different diameters. (a) 20 bubbles, (b) 25 bubbles, (c) 32 bubbles, (d) 38 bubbles.

fission gas areal density, less than 2% of the total area. Grain boundary fission gas bubble size increases with an increase in burnup [22]. With an increase in fission density, more fission gas usually diffuses to the grain boundary area and recrystallization [66] subdivides the grains to accommodate the fission gas near the grain boundaries. This also increases the grain boundary fission gas density. Our results were also compared with porosity correction models, specifically those of Bauer [67] and Peddicord [68]. Bauer's model ($\lambda = \lambda_0 e^{-2.14\nu}$, where λ_0 is the thermal conductivity of the 100% dense material and ν is the porosity) over-predicts the porosity correction factor for thermal conductivity. Peddicord's model ($\lambda = \lambda_0(1 - \nu)^{2.58}$) agrees better with the effective thermal conductivity from our simulations.

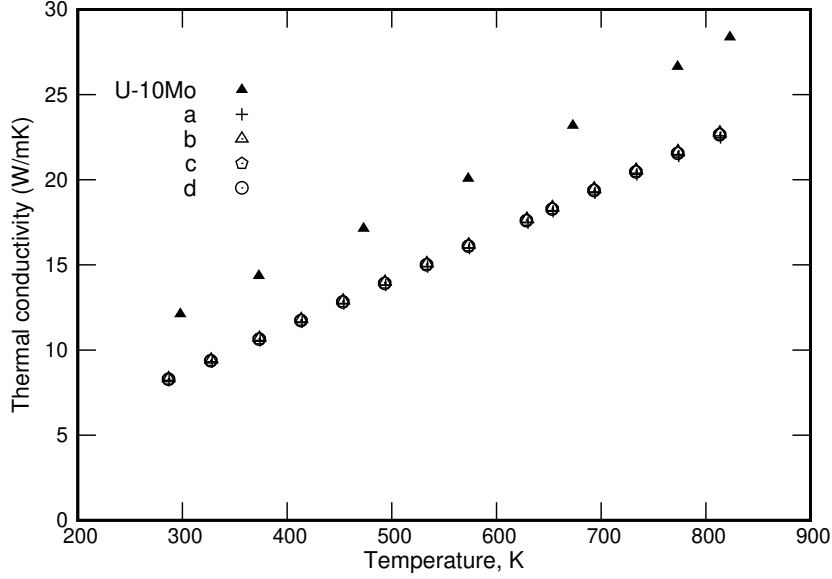


Figure 3.11. Comparison of thermal conductivity between different bubble diameters at constant total bubble area with bubble-free U-10Mo. Bubble arrangements are shown in Figure 3.10. Bubble diameters are (a) 0.894 nm (b) 0.8 nm (c) 0.707 nm and (d) 0.6488 nm; the bubble area fraction is 12.6% percent.

All these empirical models are applicable to intragranular gas bubbles with uniform distribution and negligible fission gas thermal conductivity. In our calculation, all the thermal conductivities are measured from two-dimensional finite element models, but two-dimensional thermal conductivity usually represents the lower limit of the three-dimensional thermal conductivity [69]. Accurate estimation of this limit is very important.

3.4 Conclusions

Estimating the thermal conductivity of nuclear fuel is an important part of understanding fuel behavior in nuclear reactors. In our work, xenon gas was used to represent fission gas bubbles in U-10Mo monolithic fuels. The impact of distributed xenon bubbles on the overall thermal conductivity of U-10Mo is significant, resulting in a 25–35 percent drop in conductivity for the bubble volume

fractions studied, largely independent of bubble arrangement. Both intra- and inter-granular gas bubble structures were used. For intra-granular bubbles, a gas bubble superlattice structure was used. The results indicate that the Maxwell–Eucken and Hashin–Shtrikman models overestimate thermal conductivities by at least 5% for the bubble volume fractions studied.

The pressure dependence of xenon’s thermal conductivity was also studied to estimate the impact of bubble pressure on the overall thermal conductivity of U-10Mo. Our results indicate that bubble pressure is not a significant factor for the bubble densities studied—the overall thermal conductivity remains largely unchanged between 1 bar and 1000 bar. We also find that there is little difference between pure xenon bubbles and 85% xenon–15% krypton bubbles from the perspective of overall thermal conductivity in bubble-laden U-10Mo.

We find that both intra- and inter-granular xenon bubbles reduce the overall thermal conductivity by more than 25 percent. Different bubble arrangements have very little impact on the overall heat flow, unless the arrangement leads to a significant bubble-free channel through which heat can be conducted without interference from nearby bubbles. Bubble size is also not a significant factor, as different bubble sizes at the same bubble areal density produce a U-10Mo slabs with identical overall conductivity.

We did not consider the effects of solid fission products and their influence on the overall thermal conductivity. We believe that this issue needs a complete and thorough investigation, because the chemical state and the distribution of the solid fission products of U–Mo may make important contributions to the overall conductivity. Future work should also study, quantitatively, the contact resistance between the cladding and fuel, as well as the evolution of grain boundaries with time and the influence of local molybdenum concentration on thermal conductivity.

References

1. J. L. Snelgrove, G. L. Hofman, M. K. Meyer, C. L. Trybus, and T. C. Wiencek, Nucl. Eng. Des. **178**, 119 (1997).
2. J. H. Kittel, B. R. T. Frost, J. P. Mustelier, K. Q. Bagley, G. C. Crittenden, and J. Van Dievoet, J. Nucl. Mater. **204**, 1 (1993).
3. M. K. Meyer, T. C. Wiencek, S. L. Hayes, and G. L. Hofman, J. Nucl. Mater. **278**, 358 (2000).
4. G. L. Hofman, R. F. Domagala, and G. L. Copeland, J. Nucl. Mater. **150**, 238 (1987).
5. G. Donzé and G. Cabane, J. Nucl. Mater. **1**, 364 (1959).
6. F. Giraud-Heraud and J. Guillaumin, Acta Metall. **21**, 1243 (1973).
7. D. A. Lopes, T. A. G. Restivo, and A. F. Padilha, J. Nucl. Mater. **440**, 304 (2013).
8. H. Okamoto, M. E. Schlesinger, and E. M. Mueller, eds., Mo (molybdenum) binary alloy phase diagrams, in *Alloy Phase Diagrams*, ASM Handbook, Vol. 3 (ASM International, 2016) pp. 489–498.
9. A. Berche, N. Dupin, C. Guénau, C. Rado, B. Sundman, and J. C. Dumas, J. Nucl. Mater. **411**, 131 (2011).
10. D. D. Keiser, J.-F. Jue, A. B. Robinson, P. Medvedev, J. Gan, B. D. Miller, D. M. Wachs, G. A. Moore, C. R. Clark, M. K. Meyer, and M. R. Finlay, J. Nucl. Mater. **425**, 156 (2012).
11. G. L. Hofman, M. R. Finlay, and Y. S. Kim, in *Proceedings of the 26th International Meeting on Reduced Enrichment for Research and Test Reactors (RERTR)* (Vienna, Austria, 2004) pp. 7–12.
12. S. Van den Berghe, W. Van Renterghem, and A. Leenaers, J. Nucl. Mater. **375**, 340 (2008).
13. A. Leenaers, S. Van den Berghe, E. Koonen, C. Jarousse, F. Huet, M. Trotabas, M. Boyard, S. Guillot, L. Sannen, and M. Verwerft, J. Nucl. Mater. **335**, 39 (2004).
14. J.-F. Jue, D. D. Keiser, C. R. Breckenridge, G. A. Moore, and M. K. Meyer, J. Nucl. Mater. **448**, 250 (2014).
15. D. E. Burkes, A. M. Casella, A. J. Casella, E. C. Buck, K. N. Pool, P. J. MacFarlan, M. K. Edwards, and F. N. Smith, J. Nucl. Mater. **464**, 331 (2015).
16. V. V. Rondinella and T. Wiss, Mater. Today **13**, 24 (2010).
17. S. Ishimoto, M. Hirai, K. Ito, and Y. Korei, J. Nucl. Sci. Technol. **31**, 796 (1994).

18. K. Kang, K. Song, S. Lee, and S. Kim, Int. J. Thermophys. **28**, 2188 (2007).
19. J. Gan, D. Keiser, B. Miller, A. Robinson, D. Wachs, and M. Meyer, J. Nucl. Mater. **464**, 1 (2015).
20. A. Blades, W. Fleming, and H. Thode, Can. J. Chem. **34**, 233 (1956).
21. J. Petruska, H. Thode, and R. Tomlinson, Can. J. Phys. **33**, 693 (1955).
22. Y. S. Kim and G. L. Hofman, J. Nucl. Mater. **419**, 291 (2011).
23. B. D. Miller, J. Gan, D. D. Keiser, Jr., A. B. Robinson, J. F. Jue, J. W. Madden, and P. G. Medvedev, J. Nucl. Mater. **458**, 115 (2015).
24. B. D. Miller, J. Gan, J. Madden, J.-F. Jue, A. Robinson, and D. D. Keiser, J. Nucl. Mater. **424**, 38 (2012).
25. J. Gan, D. D. Keiser, B. D. Miller, A. B. Robinson, J.-F. Jue, P. Medvedev, and D. M. Wachs, J. Nucl. Mater. **424**, 43 (2012).
26. J. Gan, D. D. Keiser, D. M. Wachs, A. B. Robinson, B. D. Miller, and T. R. Allen, J. Nucl. Mater. **396**, 234 (2010).
27. P. B. Johnson and D. J. Mazey, J. Nucl. Mater. **93–94**, 721 (1980).
28. P. B. Johnson and D. J. Mazey, J. Nucl. Mater. **91**, 41 (1980).
29. J. H. Evans, J. Nucl. Mater. **119**, 180 (1983).
30. D. J. Mazey and J. H. Evans, J. Nucl. Mater. **138**, 16 (1986).
31. J. H. Evans and D. J. Mazey, J. Nucl. Mater. **138**, 176 (1986).
32. P. B. Johnson, K. J. Stevens, and R. W. Thomson, Nucl. Instrum. Meth. Phys. Res. B **62**, 218 (1991).
33. P. B. Johnson and D. J. Mazey, J. Nucl. Mater. **218**, 273 (1995).
34. F. E. Lawson and P. B. Johnson, J. Nucl. Mater. **252**, 34 (1998).
35. N. M. Ghoniem, D. Walgraef, and S. J. Zinkle, J. Comput. Aided Mater. Des. **8**, 1 (2001).
36. P. B. Johnson and F. Lawson, Nucl. Instrum. Meth. Phys. Res. B **243**, 325 (2006).
37. J. Gan, D. D. Keiser, Jr., B. D. Miller, A. B. Robinson, D. M. Wachs, and M. K. Meyer, J. Nucl. Mater. **464**, 1 (2015).
38. K. Bakker, Int. J. Heat Mass Tran. **40**, 3503 (1997).
39. J. C. Maxwell, *A Treatise on Electricity and Magnetism*, Vol. 1 (Clarendon Press, Oxford, 1881).

40. J. B. MacEwan, R. L. Stoute, and M. J. F. Notley, *J. Nucl. Mater.* **24**, 109 (1967).
41. L. A. Goldsmith and J. A. M. Douglas, *J. Nucl. Mater.* **47**, 31 (1973).
42. M. F. DeVries, *J. Heat Tran.* **111**, 281 (1989).
43. A. L. Loeb, *J. Am. Ceram. Soc.* **37**, 96 (1954).
44. M. E. Cunningham and K. L. Peddicord, *Int. J. Heat Mass Tran.* **24**, 1081 (1981).
45. D. Y. Tzou, *Int. J. Heat Mass Tran.* **34**, 1839 (1991).
46. T. H. Bauer, *Int. J. Heat Mass Tran.* **36**, 4181 (1993).
47. S. Hu, A. M. Casella, C. A. Lavender, D. J. Senor, and D. E. Burkes, *J. Nucl. Mater.* **462**, 64 (2015).
48. Trellis Pro (csimsoft, LLC., American Fork, Utah, 2012–2017).
49. V. A. Rabinovich, A. A. Vasserman, V. I. Nedostup, and L. S. Veksler, *Thermo-physical Properties of Neon, Argon, Krypton, and Xenon* (Hemisphere Publishing Corporation, New York, NY, 1987).
50. A. R. Kaufmann, *Nuclear Reactor Fuel Elements: Metallurgy and Fabrication* (Interscience Publishers, New York, 1962).
51. D. E. Burkes, C. A. Papesch, A. P. Maddison, T. Hartmann, and F. J. Rice, *J. Nucl. Mater.* **403**, 160 (2010).
52. G. W. Greenwood, A. J. E. Foreman, and D. E. Rimmer, *J. Nucl. Mater.* **1**, 305 (1959).
53. H. Trinkaus, *Radiat. Eff.* **78**, 189 (1983).
54. H. Xiao, C. Long, X. Tian, and S. Li, *Mater. Des.* **74**, 55 (2015).
55. L. E. Thomas, in *Fundamental Aspects of Inert Gases in Solids* (Springer, New York, 1991) pp. 431–441.
56. M. Ross and A. K. McMahan, *Phys. Rev. B* **21**, 1658 (1980).
57. J. Zheng, Q. F. Chen, Y. J. Gu, Z. Y. Chen, and C. J. Li, *J. Chem. Phys.* **141**, 124 (2014).
58. C. Wilke, *J. Chem. Phys.* **18**, 517 (1950).
59. W. G. Vincenti and C. H. Kruger, *Introduction to Physical Gas Dynamics* (John Wiley and Sons, New York, 1965).
60. H. Alkandry, I. Boyd, and A. Martin, in *51st AIAA Aerospace Sciences Meeting including the New Horizons Forum and Aerospace Exposition* (2013) p. 303.

61. D. Gaston, C. Newman, G. Hansen, and D. Lebrun-Grandjean, Nucl. Eng. Des. **239**, 1768 (2009).
62. C. R. Clark, G. C. Knighton, M. K. Meyer, and G. L. Hofman, in *2003 International Meeting on Reduced Enrichment for Research and Test Reactors*, Vol. 1 (Chicago, Illinois, 2003).
63. D. S. Smith, A. Alzina, J. Bourret, B. Nait-Ali, F. Pennec, N. Tessier-Doyen, K. Otsu, H. Matsubara, P. Elser, and U. T. Gonzenbach, J. Mater. Res. **28**, 2260 (2013).
64. Z. Hashin and S. Shtrikman, J. Appl. Phys. **33**, 3125 (1962).
65. B. Schulz, High Temp. High Press. **13**, 649 (1981).
66. Y. S. Kim, G. Hofman, and J. Cheon, J. Nucl. Mater. **436**, 14 (2013).
67. T. H. Bauer and J. W. Holland, Nucl. Technol. **110**, 407 (1995).
68. K. L. Peddicord, M. E. Cunningham, and A. Tripathi, Trans. Am. Nucl. Soc. **28**, 548 (1978).
69. K. Bakker, H. Kwast, and E. H. P. Cordfunke, J. Nucl. Mater. **226**, 128 (1995).

CHAPTER 4

PSEUDOPOTENTIAL FOR PLANE-WAVE DENSITY FUNCTIONAL THEORY STUDIES OF METALLIC URANIUM

This chapter was largely published as an article in Computational Materials Science. The authors of that article are A. Rafi M. Iasir and Karl D. Hammond of the University of Missouri.

4.1 Introduction

Uranium is the heaviest naturally-occurring element on Earth. The discovery of fission in uranium (specifically, in ^{235}U) impacted not only scientists and engineers all over the world, it also changed global politics forever. In nuclear research, the nucleus of the uranium atom is of much more importance than the electrons surrounding it, but the electronic structure is important to the thermodynamic properties, including crystal structure. The structural features are particularly important to the study of next-generation nuclear fuels, such as U–10Mo, that are based on metallic uranium. The electronic behavior of uranium, along with other light actinides (Pa–Pu), results in a low-symmetry crystal structure at ambient temperature and pressure—most metallic elements take on relatively high-symmetry structures (bcc, fcc, and hcp), but the light actinides are either orthorhombic or monoclinic at standard temperature and pressure [1]. Pure uranium exists in three different solid phases at atmospheric pressure, depending on the temperature: α

(base-centered orthorhombic), β (tetragonal) and γ (body-centered cubic). At atmospheric pressure, α -uranium transforms to β -uranium at approximately 935 K, and β -uranium transforms to γ -uranium at approximately 1045 K [2, 3]. The influence of $5f$ electron-electron correlation plays a pivotal role in the crystallographic behavior of uranium and other light actinides [4, 5]; with this in mind, proper representation of uranium's $5f$ electrons is very important.

The stability of the crystal structures of the inner transition metals has been the target of several electronic structure studies. Eriksson and coworkers [6, 7] performed comparative studies of thorium, protactinium, and uranium's crystal structures, calculating the equilibrium volume and bulk modulus using the full-potential linear-muffin-tin-orbital (FP-LMTO) technique and the local density approximation (LDA). The predicted equilibrium lattice parameters did not compare well with experiments. However, Söderlind et al. [8] showed a few years later that the generalized gradient approximation (GGA) provides much better agreement with experiment for actinides.

Crocombette *et al.* [9] used norm-conserving pseudopotentials to study three metallic phases of uranium (α , γ , and a hypothetical fcc structure). The calculated equilibrium volume for α -uranium was underestimated by more than 6 percent. Söderlind [10] calculated the equilibrium lattice parameters and also estimated the elastic moduli of α -uranium using the FP-LMTO method. The calculated equilibrium lattice parameters were in good agreement with experimental values, but the elastic moduli did not agree particularly well with experiments. The calculated elastic moduli were likely higher than measured values because uranium undergoes strong phonon softening with increases in temperature, and the measured values (taken at room temperature) would likely be lower than they would be at low temperatures [11].

Söderlind's [10] was the first attempt to calculate α -uranium's elastic moduli. Other theoretical studies of light actinides prior to 2000 using full-core (*i.e.*, non-pseudopotential-based) techniques are summarized by Jones *et al.* [12]. Taylor [13] studied uranium phases using the projector augmented wave (PAW) method [14] with Perdew and Wang's 1991 (PW91) exchange–correlation functional [15, 16]. Taylor investigated α , γ , and fcc uranium. The equilibrium lattice parameters of α -uranium were within 1% of experimental values at 50 K [17]. The lattice parameter of γ -uranium was also in good agreement with measured values, though the lattice parameter of fcc uranium was overestimated compared to the value calculated by Crocombette *et al.* [9]. Xiang *et al.* [18] used the Perdew–Burke–Ernzerhof (PBE) exchange–correlation functional [19, 20] to study the equilibrium volume of α - and γ -uranium. They also studied the bct structure, an approximation of the β phase. Their results were also in good agreement with previous full-potential studies and experiments. Li *et al.* [21] also studied the structure, formation energies, and elastic moduli of α , β , γ , fcc, and hcp uranium using the PW91 exchange–correlation functional [22]. Their pseudopotential produced reasonably accurate lattice parameters and cell volumes for α -uranium, accompanied by reasonable elastic moduli. Beeler *et al.* [23] utilized the PBE exchange–correlation functional to study uranium, and found similar values to Li *et al.*, with the exception of the body-centered tetragonal case (approximating β -uranium). The existing pseudopotential (norm-conserving) in the QUANTUMESPRESSO PS library [24, 25] has a high cut-off energy, making it computationally expensive to study large supercells. We sought a PAW-based pseudopotential suitable for studies of uranium alloys.

In the present work, we investigate the crystal structure and elastic properties of metallic uranium with density functional theory (DFT) with a projector augmented wave (PAW) pseudopotential [14]. We investigate four structures of uranium: α , γ , bct, and fcc. Our results are compared with previously-published electronic

structure calculations and experiments. The electronic densities of states for all four crystal structures are also calculated. During the development of this pseudopotential, no PAW pseudopotential was available in PS library [24, 25]. However, a PAW pseudopotential (scalar-relativistic) was added recently, so we compare our results with the newly added pseudopotential in the PS library (PsL) for α - and γ -uranium. We obtain very similar results for α -uranium, but for γ -uranium, some of the stress–strain curves show discrepancies around the minima.

4.2 Computational Details

We perform all calculations using density functional theory (DFT) with plane-wave basis sets as implemented in the software QUANTUMESPRESSO [26]. We generated a uranium pseudopotential for use with the Perdew–Burke–Ernzerhof (PBE) exchange–correlation functional [19, 20]. The projector augmented wave (PAW) pseudopotential-generating software atompaw [27, 28] was used to generate the PAW pseudopotential for uranium. The same pseudopotential was used for all subsequent calculations.

The calculations are performed with a scalar-relativistic model. Full spin–orbit coupling was not used. Previous spin–orbit coupling results [10] showed a very small effect on α -uranium’s equilibrium lattice parameter (within 1% of experiment [17]). We also have not included on-site electron correlation (DFT+U) for uranium. Söderlind *et al.* [29] showed that the addition of on-site Coulomb repulsion leads to a finite magnetization of γ -uranium, which is not observed in experiments—it is therefore inadvisable to use such corrections.

One of the major challenges in studying actinides using DFT is how to treat the large number of electrons. The pseudopotential approach effectively reduces the number of electrons by modeling the “core” as a potential energy surface, so generating a pseudopotential requires one to choose the number of electrons that will

be treated explicitly. There are two approaches common for uranium: “small-core” pseudopotentials and “large-core” pseudopotentials. In a large-core pseudopotential, the valence electrons are the $5f$, $6s$, $6p$, $6d$ and $7s$ shells (14 electrons). In small-core pseudopotentials, the $5s$, $5p$, and $5d$ shells are also included, which treats 32 electrons as valence electrons. Iche-Tarrat and Marsden [30] have discussed this topic and shown that the explicit treatment of 32 electrons only marginally improves the performance of DFT at significantly higher computational cost. The valence electron configuration of uranium used when generating our pseudopotential was $6s^26p^67s^26d^15f^3$ (*i.e.*, it is a large-core pseudopotential). The radius of the augmentation region was chosen to be 2.5 bohr, which we determined by starting from half the experimental nearest-neighbor interatomic distance in α -uranium and adjusting based on energy–volume minimization. The pseudo-partial waves were generated using the RRKJ scheme [31], which uses a sum of Bessel functions to represent the pseudo-partial waves. A plane-wave cutoff energy analysis was performed and a 50 Ry energy cutoff was found to be sufficient based on a plot of total energy against cutoff energy. All calculations were performed on primitive cells using the cell geometries and coordinates given by Crocombette *et al.* [9] for α -uranium, Beeler *et al.* [23] for bct uranium, and values from the Structure of Crystals database [32] for all other structures. Periodic boundaries were applied in all directions. The Monkhorst–Pack scheme [33] was used for Brillouin zone sampling; the k -point meshes were $20 \times 20 \times 26$, $20 \times 20 \times 20$, $18 \times 18 \times 18$, and $20 \times 20 \times 20$ for the α , bct, γ , and fcc lattices, respectively. A Methfessel–Paxton [34] smearing method (width 0.02 Ry) was used to integrate the bands at the Fermi level. To calculate the nine unique elastic moduli of orthorhombic α -uranium, the energy–strain relationship (see section 4.4) was used as described by Ravindran *et al.* [35]. For cubic structures, the elastic moduli were evaluated using volume-conserving orthorhombic and monoclinic distortions as described by Beckstein *et al.* [36].

Table 4.1. Parameters used to generate the pseudopotential in atompaw [27, 28].

Cutoff	Value (bohr)
r_{PAW}	2.50
r_{shape}	2.02
r_{vloc}	1.50
r_{core}	1.80
$r_{c,i}$	r_{PAW}
EXCEPT	
$r_{c,6s}$	1.50
$r_{c,7s}$	1.50

4.3 Results

The pseudopotential itself is generated by atompaw [27, 28], which takes as input the augmentation radius (r_{PAW}), core radius (r_{core}), shape function cutoff (r_{shape}), matching radius (r_{vloc}), valence and core electron configurations, density functional, and the cutoff radii for each of the partial waves ($r_{c,i}$). We assumed $r_c = r_{\text{PAW}}$ for all valence electrons except the 6s and 7s electrons, for which r_c was adjusted. The cutoff radii are given in Table 4.1. These cutoffs, combined with the choice of density functional and valence electrons, are sufficient to reproduce the pseudopotential in atompaw.

According to our calculations, α phase has the lowest energy (see Fig. 4.1) at ground state. Properties of several uranium phases as calculated with the pseudopotential presented above are detailed in the rest of this section.

4.3.1 α -Uranium

Uranium's α phase has a base-centered orthorhombic structure with space group $Cmcm$ (no. 63). The asymmetric unit has uranium atoms at Wyckoff position $4c$ $(0, \pm y, \pm \frac{1}{4})$, where the position parameter y has been found to be a function of temperature [17]. At room temperature, the value of y has been measured to be

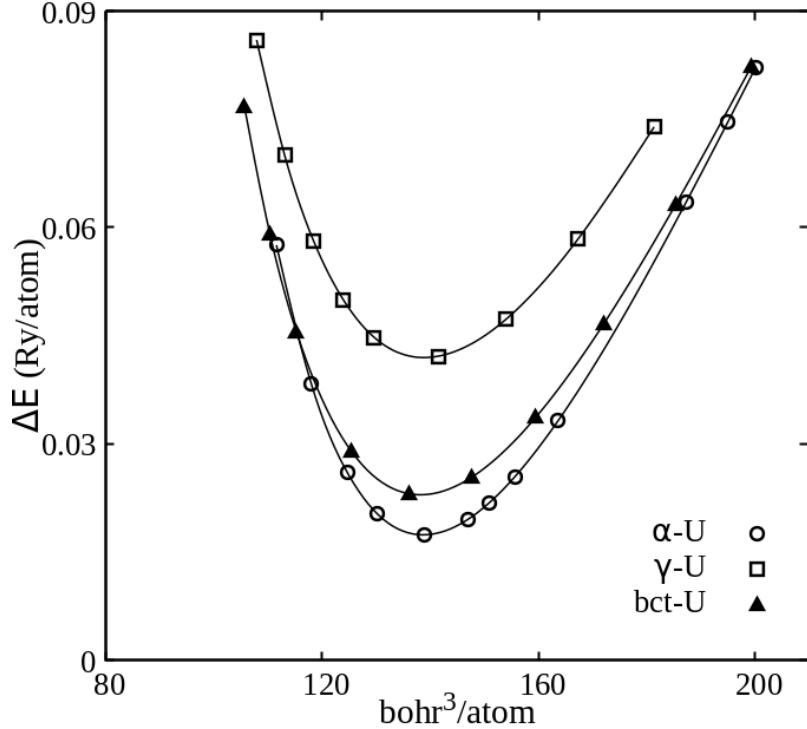


Figure 4.1. Energy vs. volume curve for three different phases of uranium.

0.1024 [17, 37]. There are four atoms in the standard unit cell (two in the primitive cell). The α phase is thermodynamically favorable at temperatures below 935 K and pressures up to 100 GPa [3, 38]. This makes the α phase important to the nuclear energy community because it is the naturally-occurring phase of uranium. The solid-state physics community also shows interest in α -uranium because of certain unusual characteristics, including charge density wave transitions and superconductivity.

The total energy as a function of unit cell volume for α -uranium is shown in Figure 4.2; Table 4.2 summarizes the optimized lattice parameters, the distance parameter y , and the calculated elastic moduli, along with results from previously-published calculations and experiments. We confirm that α -uranium is the lowest-energy crystal structure among those we tested. Our pseudopotential predicts an

equilibrium volume of 20.49 \AA^3 , which is in close agreement with the experimental value of 20.530 \AA^3 (at 50 K). The position parameter y exhibits a minimum-energy value of 0.0986 at the equilibrium volume of 20.49 \AA^3 . This trend in y is similar to that observed in the calculations of Wills and Eriksson [6].

Our cell volume results differ from previous calculations using PAW [23], which obtained an equilibrium volume of 19.987 \AA^3 (the work was done using VASP [39–41]). A Murnaghan [42] fit to the total energy as a function of volume for α -uranium yielded a bulk modulus of 132.1 GPa, which is larger than the experimental value of $104 \pm 2 \text{ GPa}$ [38], but agrees closely with the quantum molecular dynamics (QMD) results of Hood *et al.* [43] (133.5 GPa) and the diamond anvil cell (DAC) experiments of Yoo *et al.* [44], which reported a bulk modulus of 135.5 GPa. Our pseudopotential-based results are in close agreement with the all-electron FP-LMTO calculations of Söderlind [10], which gave an equilibrium volume of 20.67 \AA^3 and a bulk modulus of 133.0 GPa. A published PAW-based pseudopotential from Beeler *et al.* [23] yields an equilibrium volume of 19.92 \AA^3 , which is lower than our result and farther from both the experimental value and the result from all-electron calculations.

The elastic moduli predicted by our pseudopotential are presented in Table 4.2. Like all materials with orthorhombic symmetry, α -uranium has nine unique elastic moduli. Our model overestimates most of the elastic moduli relative to experiments. The three primary-direction elastic moduli (C_{11} , C_{22} , and C_{33}) show good agreement with other theoretical results and with experiment, though all three principal elastic moduli are overestimated. The order ($C_{33} > C_{11} > C_{22}$) of these three elastic moduli is also consistent with experiments. For C_{55} and C_{13} , the present results also show good agreement with experiments. The value of C_{66} is overestimated relative to experiment, but closer than any existing prediction from a pseudopotential-based calculation. The other elastic moduli are generally similar to existing theoretical predictions.

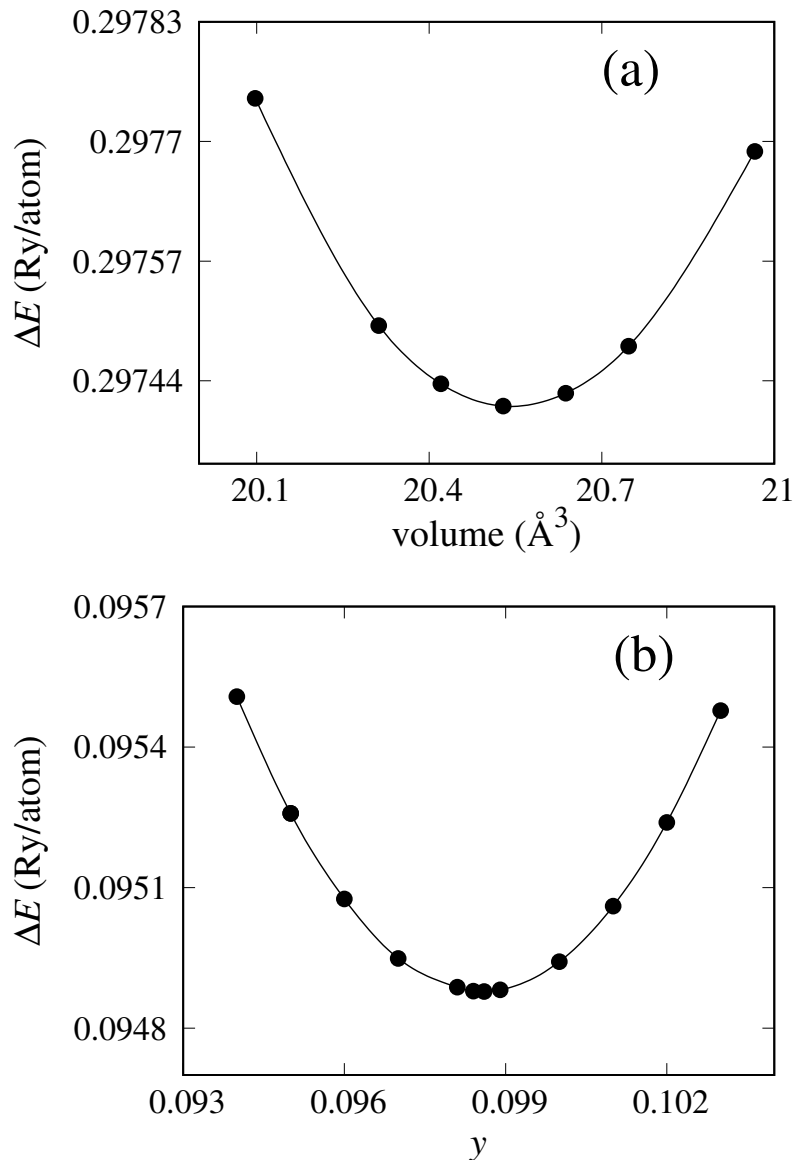


Figure 4.2. (a) Calculated total energy as a function of volume for α -uranium. (b) Calculated total energy as a function of the positional parameter y for α -uranium. The calculation of y is constrained to an equilibrium volume of 20.49 \AA^3 .

Table 4.2. Ground-state properties and elastic moduli of α -uranium from present work, compared with the PAW pseudopotential calculations of Beeler *et al.* [23], the full-core calculations of Söderlind [10], and experiments from Barrett [17], Le Bihan *et al.* [38], and Fisher and McSkimin [45] (295 K).

	Theory	Barrett [17]	Le Bihan [38]	Fisher [45]
	present work	Beeler [23]	Söderlind [10]	Experiment
a (Å)	2.834	2.793	2.845	2.836
b (Å)	5.862	5.849	5.818	5.867
c (Å)	4.932	4.893	4.996	4.936
y	0.0986	0.097	0.103	0.102
volume/atom (Å ³)	20.48	19.987	20.674	20.535
B (GPa)	132.1	151	133	104(2)
B'	5.27	-	5.4	6.2
C_{11} (GPa)	315	299	300	-
C_{22} (GPa)	213	231	220	-
C_{33} (GPa)	387	364	320	-
C_{44} (GPa)	135	100	150	-
C_{55} (GPa)	87	150	93	-
C_{66} (GPa)	104	132	120	-
C_{12} (GPa)	58	59	50	-
C_{13} (GPa)	45	30	5	-
C_{23} (GPa)	146	144	110	108

4.3.2 γ -U: Crystal Structure and Elastic Moduli

The structure of γ -uranium at high temperature was first elucidated by Wilson and Rundle [46] at Iowa State University in 1949 using powdered uranium at 800 °C. The γ phase of uranium has a body-centered cubic (bcc; Structurbericht designation A2) structure with two atoms in the standard unit cell [47, 48]. It is thermodynamically stable from 1050 K to the melting point of 1406 K [44].

In the nuclear fuels community, γ -uranium is preferred to α -uranium because it undergoes isotropic thermal expansion and radiation-induced swelling [49]. As Wilson and Rundle observed [46], it is not possible to quench pure γ -uranium to room temperature, but a metastable bcc phase can be retained at room temperature in U–Mo alloys. Recently, it was found that the bcc structure can be retained by alloying uranium with other metals, such as platinum, palladium, niobium, and zirconium [50]. In particular, the eutectoid point of γ -uranium with molybdenum impurities is at approximately 89 weight-percent uranium (see Fig. 1.3); to take advantage of the depressed phase transition temperature (and the associated increase in stability of the bcc phase), uranium alloyed with 10 wt% molybdenum (≈ 21.6 at.%; U-10Mo) is currently being developed as a potential high-density low-enrichment uranium (LEU) fuel for high-performance research reactors. The lattice parameters, volume per atom, and elastic moduli as calculated with our pseudopotential-based model are presented in Table 4.3.

The lattice parameters for γ -uranium as calculated with the pseudopotential presented here are in good agreement with experiments. The elastic moduli are comparable with those of Beeler *et al.* [23] and Taylor [13]. The value of C_{12} is larger than that of C_{11} , which is a violation of one of the stability criteria for cubic crystals ($C_{11} - C_{12} > 0$), often called the Born stability criterion [51–53]. This violation is expected, as the bcc phase of uranium is unstable at low temperatures. The

Table 4.3. Equilibrium lattice parameters, volume per atom, and elastic moduli of γ -uranium. Results are compared with the PAW pseudopotential calculations from PsL [24, 25], Beeler *et al.* [23], and Taylor [13], as well as the norm-conserving pseudopotential calculations of Crocombette *et al.* [9] and the experiments of Wilson and Rundle [46] at room temperature. Elastic moduli are compared with previous PAW pseudopotential calculations from Beeler *et al.* [23] and Taylor [13].

	Theory					Experiment	
	present work	PsL [24, 25]	Beeler [23]	Taylor [13]	Crocombette [9]	Wilson [46]	Yoo [44]
a (Å)	3.45	3.458	3.427	3.43	3.37	3.47	-
volume/atom (Å ³)	20.56	20.675	20.124	20.18	19.14	20.89	-
C_{11} (GPa)	28	27	86	161	-	-	-
C_{12} (GPa)	167	165	155	184	-	-	-
C_{44} (GPa)	51	59	37	56	-	-	-
B (GPa)	121	119	132	176	170	-	113.3

Table 4.4. The optimized lattice parameters (\AA), volume per atom (\AA^3), and elastic moduli of bct uranium. Our calculated results are compared with those of Beeler *et al.* [23], Li *et al.* [21], Xiang *et al.* [18], and Söderlind [54].

	present work	Beeler [23]	Li [21]	Xiang [18]	Söderlind [54]
a (\AA)	3.44	3.695	3.72	-	-
c/a	0.8125	0.8	1.24	-	0.82
vol./atom (\AA^3)	20.44	20.268	31.896	20.5	-
C_{11} (GPa)	270	264	230	-	-
C_{33} (GPa)	257	254	204	-	-
C_{12} (GPa)	65	55	61	-	-
C_{13} (GPa)	32	68	61	-	-
C_{44} (GPa)	59	56	79	-	-
C_{55} (GPa)	71	56	39	-	-
B (GPa)	115.4	130	114	-	-

experimental value of bulk modulus by Yoo *et al.* [44] is in good agreement with our result.

4.3.3 Body-Centered Tetragonal Uranium

The β phase of uranium is stable at atmospheric pressure between 935 and 1045 K [2]. Tucker [55] determined that it has a tetragonal structure with 30 atoms per unit cell, but his space group assignment was later disputed. The assignment of a space group remained a controversy until 1988, when Lawson and coworkers [2] published neutron powder diffraction results. The experimental difficulties lie in the preparation of a single crystal of β -uranium and the need to operate at high temperature. Single crystals of a β -uranium alloy containing 1.4 atom% chromium were created by Tucker [56] and quenched to room temperature, but he did not establish whether this alloy had the same crystal structure as pure β -uranium [2]. An overview of the development of the crystal structure of β -uranium is given by Donohue and Einspahr [57, 58]. The present consensus is that β -uranium has a

Table 4.5. The equilibrium lattice parameter, volume per atom, and elastic moduli of fcc uranium. Results are compared with PAW pseudopotential calculations of Beeler *et al.* [23], Taylor [13], and Crocombette *et al.* [9].

	present work	Beeler [23]	Taylor [13]	Crocombette [9]
a (Å)	4.300	4.433	4.48	4.30
volume/atom (Å ³)	21.765	21.774	22.48	19.88
C_{11} (GPa)	67	46	184	-
C_{12} (GPa)	130	144	267	-
C_{44} (GPa)	38	40	28	-
B (GPa)	108.7	111	239	148

tetragonal crystal structure with space group $P4_2/mnm$ (no. 136) and 30 atoms in the unit cell.

We chose to simulate a body-centered tetragonal structure instead of β -uranium because of the latter's complexity and computational expense. A similar simplification was used in studies similar to ours [21, 23]. The bct structure has only two atoms per unit cell, and is therefore less computationally expensive than β -uranium. The equilibrium lattice parameters of bct uranium are presented in Table 4.4, alongside values from Beeler *et al.* [23] and Li *et al.* [21]. The volume per atom agrees well with Beeler *et al.* but is significantly different from that of Li *et al.* Xiang *et al.* [18] also studied the bct structure of uranium, though they did not provide the equilibrium lattice parameter or c/a ratio; their value of the equilibrium volume per atom was 20.5 Å³, similar but larger than our value. Our c/a ratio is in good agreement with both Beeler *et al.* [23] (0.8) and Söderlind [54] (0.82).

4.3.4 Face-Centered Cubic Uranium

Face-centered cubic uranium does not exist in nature, but it is a reasonable way to check the pseudopotential. Beeler *et al.* [23] and Taylor [13] studied this structure as well, so we compare our results with theirs. Table 4.5 shows the

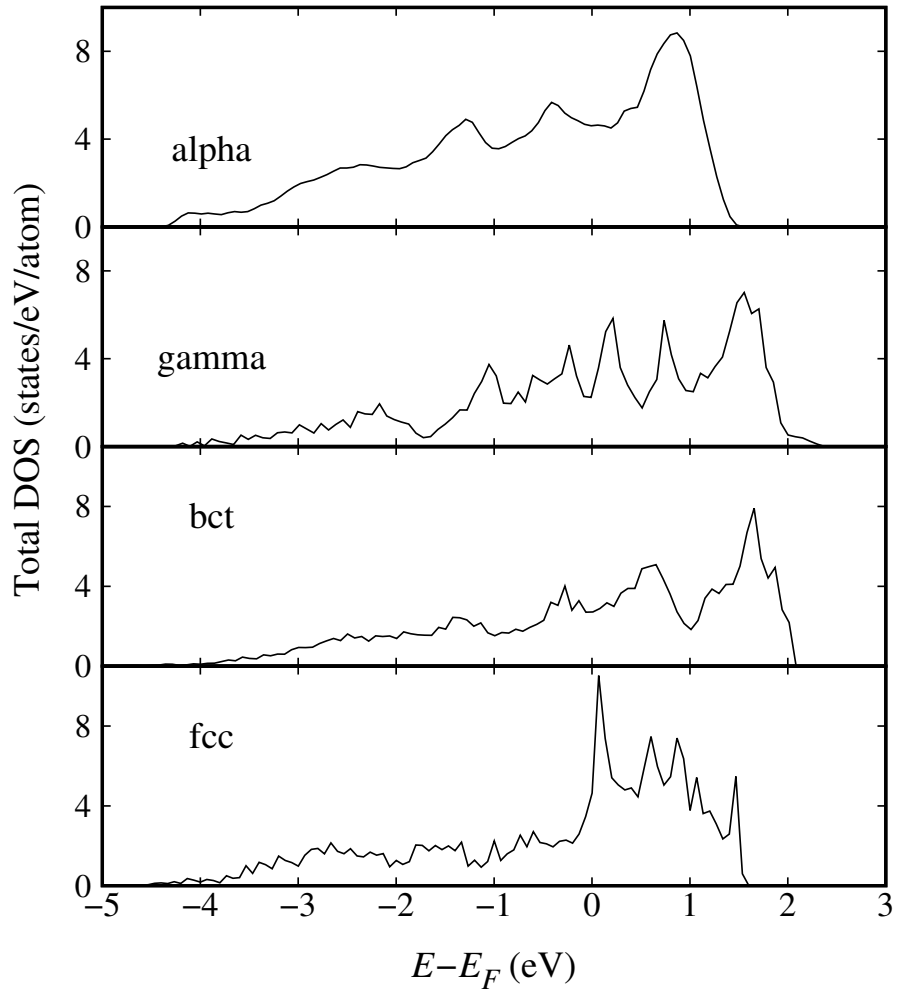


Figure 4.3. Total electronic densities of states of α , γ , bct, and fcc uranium near the Fermi level.

equilibrium parameters and elastic moduli as calculated with our model and with several other published pseudopotentials. Our results are in good agreement with other pseudopotential calculations, particularly those of Beeler *et al.* [23]; the bulk modulus shows good agreement with their value as well. It should be noted that C_{12} is still higher than C_{11} , confirming that this model predicts the fcc phase to be unstable.

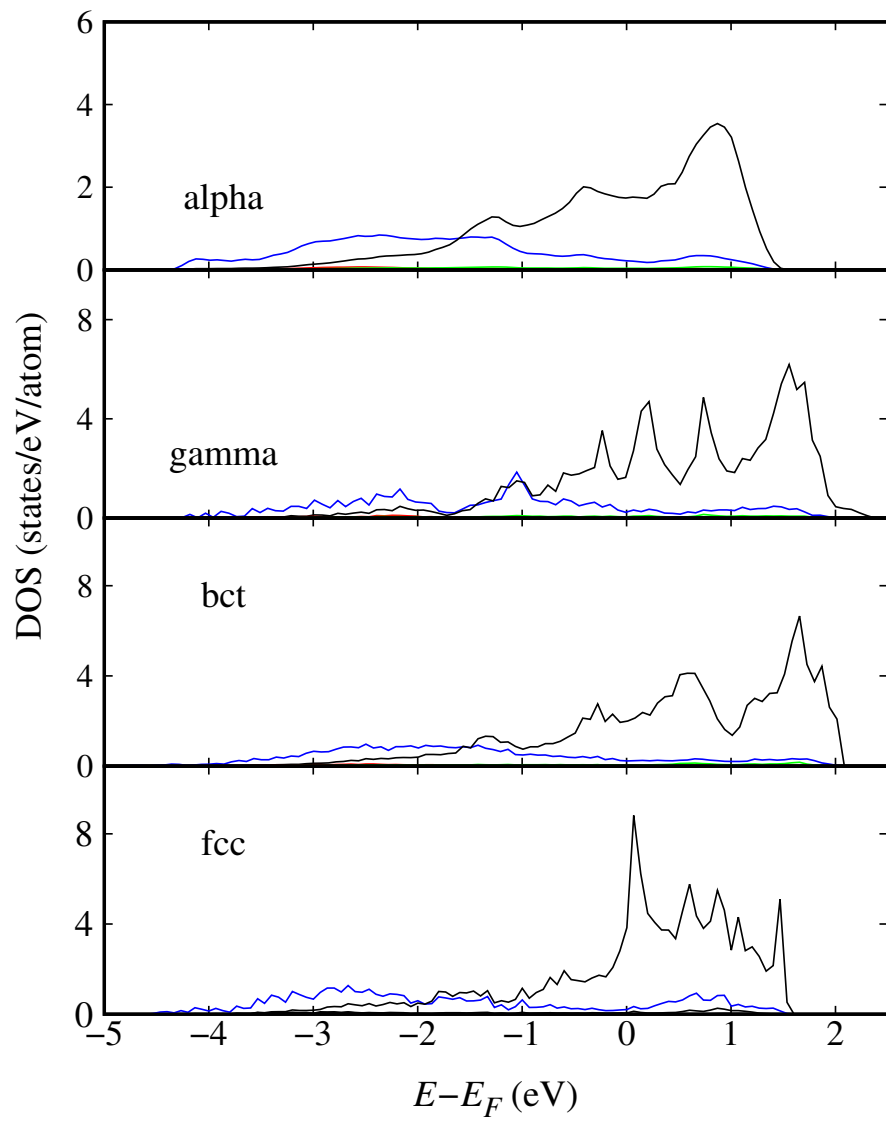


Figure 4.4. The partial electronic densities of states of α , γ , bct, and fcc uranium near the Fermi level. The 6d (blue line) and 5f (black line) electronic orbitals are shown. The s (red) and p (green) electronic orbitals are also included, but due to their very low contributions near the Fermi level, they are barely visible.

4.3.5 Electronic Density of States

The electronic densities of states (DOS) of α , bct, γ , and fcc uranium are shown in Figure 4.3. The partial densities of states for the $5f$ and $6d$ orbitals are shown in Figure 4.4. We have only shown the partial densities of states for the $5f$ and $6d$ orbitals because these are the dominant orbitals near the Fermi level of uranium. There are also contributions from $6s$, $6p$, and $7s$ orbitals near the Fermi level, but these contributions are not as significant as the dominant $5f$ and $6d$ orbitals. Electrons near the Fermi level are important because they are responsible for most of the metallic behavior. From Figure 4.3, it can be seen that the DOS spreads over energies between -4 eV and 2 eV relative to the Fermi level. The density of states with our model is comparable to those calculated by Beeler *et al.* [23] and Xiang *et al.* [18]. For bcc and bct uranium, the f orbitals spread over a broader range of energies near the Fermi level and show multiple peaks above the Fermi level. The high density of states at energies above the Fermi level in the bct and γ phases suggests that these phases would be favored over α -uranium at high temperature.

4.4 Conclusion

The equilibrium structures, cell volumes, and elastic moduli have been calculated using DFT with a newly-parameterized pseudopotential model for four different uranium phases (α , γ , body-centered tetragonal, and face-centered cubic). Our results are either in good agreement with previous work or show improvement in comparison with experiments. Studying pure uranium is the first step in exploring different alloys of uranium that are of interest to the nuclear fuels community. Due to the lower cutoff energies that can typically be used, PAW-based pseudopotentials allow one to study larger supercells, which in turn provide more accurate studies of vacancy formation, grain boundaries, and fission gas transport.

According to our pseudopotential, α -uranium is the lowest-energy crystal structure of the ones tested. The calculated elastic moduli show good agreement with previous DFT studies and experiments. Our model shows good agreement with previous pseudopotentials, but generally provides results that are either comparable to previously published pseudopotentials or closer to experimental values than previously published pseudopotentials. The three elastic moduli associated with shear (C_{44} , C_{55} , and C_{66}) show better agreement with experimental results than the tensile components. The lattice parameters of the bct structure are also very similar to those predicted by Beeler *et al.* [23], but they deviate significantly from those of Li *et al.* [21]. The elastic moduli show very similar trends to previously-published models, apart from C_{23} , which is over-predicted by our model.

For γ -uranium, which is of great interest for the development of low-enrichment uranium fuel, the lattice parameters are in close agreement with those of Taylor *et al.* [13] and with experiments. Apart from the elastic modulus C_{11} , the values of all computed parameters show very little discrepancy compared with those from the work of Taylor *et al.* [13] and Beeler *et al.* [23]. The bulk modulus shows very good agreement with experiment.

For fcc uranium, a hypothetical crystal structure, the computed lattice parameter is in close agreement with values reported by Beeler *et al.* [23] and by Crocombette *et al.* [9]. The equilibrium volume per atom does show a discrepancy from Crocombette but is in good agreement with Beeler *et al.* The elastic modulus C_{44} is also in good agreement with Beeler *et al.*, whereas C_{11} is intermediate between the value predicted by Beeler *et al.* and that predicted by Taylor *et al.* Lastly, the electronic density of states shows that the $5f$ orbital partial density of states is the largest contribution to the total density of states at the Fermi energy, and the $5f$ electrons therefore contribute the most to the bonding and conductivity of uranium. Most of the $5f$ orbital electron density is spread over energies between -4 and 2 eV

relative to the Fermi level. We also find that γ -uranium has the highest density of states at energies above the Fermi level, confirming that it should be favored at high temperature.

Appendix: Elastic Parameter Calculation of α -uranium

In this appendix, we will discuss the stress-strain relationships that were used to calculate the nine independent elastic constants of α -uranium. The base-centered orthorhombic phase of uranium has three lattice parameters: a , b , and c ; with the Bravais lattice matrix

$$\mathbf{R} = \begin{bmatrix} \frac{a}{2} & -\frac{b}{2} & 0 \\ \frac{a}{2} & \frac{b}{2} & 0 \\ 0 & 0 & c \end{bmatrix}. \quad (4.1)$$

Applying a small strain to the equilibrium lattice changes the total energy, and from this information, the elastic parameters are deduced. The elastic parameters are identified as proportional to the second order coefficient in a polynomial fit of the total energy as a function of the distortion parameter δ [59]. The distortion of the lattice vectors follows the rule $\mathbf{R}' = \mathbf{RD}$. Here, \mathbf{R}' is a matrix containing the components of the distorted lattice vectors and \mathbf{D} is the symmetric distortion matrix.

The internal energy of a crystal under strain δ can be expanded in powers of the strain tensor with respect to initial energy of the unstrained crystal in the following way:

$$E(V, \delta) = E(V_0, 0) + V_0 \left(\sum_i \tau_i \xi_i d_1 + 1/2 \sum_{ij} C_{ij} \delta_i \xi_i \delta_j \xi_j \right) + O(\delta^3) \quad (4.2)$$

The unstrained volume is V_0 , and $E(V_0, 0)$ is the energy of the unstrained system. Voight notation has been used in Eqn. (4.2) (*i.e.*, xx , yy , zz , yz , xz , and xy , respectively, are replaced with 1–6). Here, yz , xz , and xy , are equal to zy , zx , and yx , and for this reason, ξ_i is equal to 1 for $i = 1, 2$, and 3 and equal to 2 for $i = 4, 5$, and 6. τ_i is a component of the stress tensor. The first three elastic constants; C_{11} , C_{22} ,

and C_{33} ; are obtained from the following distortions:

$$\mathbf{D}_1 = \begin{bmatrix} 1 + \delta & 0 & 0 \\ 0 & 1 & 0 \\ 0 & 0 & 1 \end{bmatrix} \quad (4.3)$$

$$\mathbf{D}_2 = \begin{bmatrix} 1 & 0 & 0 \\ 0 & 1 + \delta & 0 \\ 0 & 0 & 1 \end{bmatrix} \quad (4.4)$$

$$\mathbf{D}_3 = \begin{bmatrix} 1 & 0 & 0 \\ 0 & 1 & 0 \\ 0 & 0 & 1 + \delta \end{bmatrix}. \quad (4.5)$$

The internal energies for these three distortions can be obtained from

$$E(V, \delta) = E(V_0, 0) + V_0 \tau_i \delta + \frac{V_0 C_{ii} \delta^2}{2}. \quad (4.6)$$

The constants C_{44} , C_{55} , and C_{66} are related to the distortions:

$$\mathbf{D}_4 = \begin{bmatrix} \frac{1}{(1-\delta^2)^{1/3}} & 0 & 0 \\ 0 & \frac{1}{(1-\delta^2)^{1/3}} & \frac{\delta}{(1-\delta^2)^{1/3}} \\ 0 & \frac{\delta}{(1-\delta^2)^{1/3}} & \frac{1}{(1-\delta^2)^{1/3}} \end{bmatrix} \quad (4.7)$$

$$\mathbf{D}_5 = \begin{bmatrix} \frac{1}{(1-\delta^2)^{1/3}} & 0 & \frac{\delta}{(1-\delta^2)^{1/3}} \\ 0 & \frac{1}{(1-\delta^2)^{1/3}} & 0 \\ \frac{\delta}{(1-\delta^2)^{1/3}} & 0 & \frac{1}{(1-\delta^2)^{1/3}} \end{bmatrix} \quad (4.8)$$

and

$$\mathbf{D}_6 = \begin{bmatrix} \frac{1}{(1-\delta^2)^{1/3}} & \frac{\delta}{(1-\delta^2)^{1/3}} & 0 \\ \frac{\delta}{(1-\delta^2)^{1/3}} & \frac{1}{(1-\delta^2)^{1/3}} & 0 \\ 0 & 0 & \frac{1}{(1-\delta^2)^{1/3}} \end{bmatrix}. \quad (4.9)$$

These three elastic constants can be calculated from the corresponding internal energy:

$$E(V, \delta) = E(V_0, 0) + V_0 \tau_i \delta + \frac{V_0 C_{ii} \delta^2}{2} \quad (4.10)$$

The last three distortions are

$$\mathbf{D}_7 = \begin{bmatrix} \frac{1+\delta}{(1-\delta^2)^{1/3}} & 0 & 0 \\ 0 & \frac{1-\delta}{(1-\delta^2)^{1/3}} & 0 \\ 0 & 0 & \frac{1}{(1-\delta^2)^{1/3}} \end{bmatrix} \quad (4.11)$$

$$\mathbf{D}_8 = \begin{bmatrix} \frac{1+\delta}{(1-\delta^2)^{1/3}} & 0 & 0 \\ 0 & \frac{1}{(1-\delta^2)^{1/3}} & 0 \\ 0 & 0 & \frac{1-\delta}{(1-\delta^2)^{1/3}} \end{bmatrix} \quad (4.12)$$

and

$$\mathbf{D}_9 = \begin{bmatrix} \frac{1}{(1-\delta^2)^{1/3}} & 0 & 0 \\ 0 & \frac{1+\delta}{(1-\delta^2)^{1/3}} & 0 \\ 0 & 0 & \frac{1-\delta}{(1-\delta^2)^{1/3}} \end{bmatrix} \quad (4.13)$$

The internal energies related to these three distortions are given by the following equations:

$$E(V, \delta) = E(V_0, 0) + V_0 [\tau_1 - \tau_2] \delta + \frac{1}{2} (C_{11} + C_{22} - 2C_{12}) \delta^2 \quad (4.14)$$

$$E(V, \delta) = E(V_0, 0) + V_0 [\tau_1 - \tau_3] \delta + \frac{1}{2} (C_{11} + C_{33} - 2C_{13}) \delta^2 \quad (4.15)$$

$$E(V, \delta) = E(V_0, 0) + V_0 [\tau_2 - \tau_3] \delta + \frac{1}{2} (C_{22} + C_{33} - 2C_{23}) \delta^2 \quad (4.16)$$

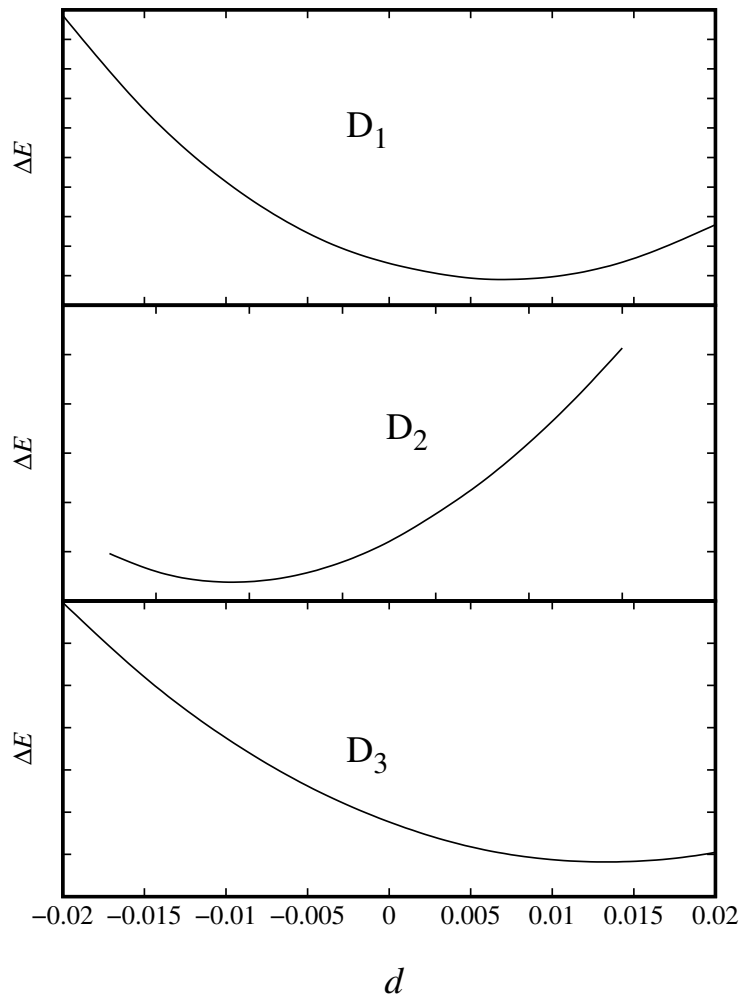


Figure 4.5. Changes in the strain energy as a function of strain using distortion matrix D_1 (4.3), D_2 (4.4), and D_3 (4.5).

The above equations can be used to calculate the remaining elastic constants C_{12} , C_{13} , and C_{23} . The energy and strain relations are calculated and included in Figures 4.5, 4.6, and 4.7.

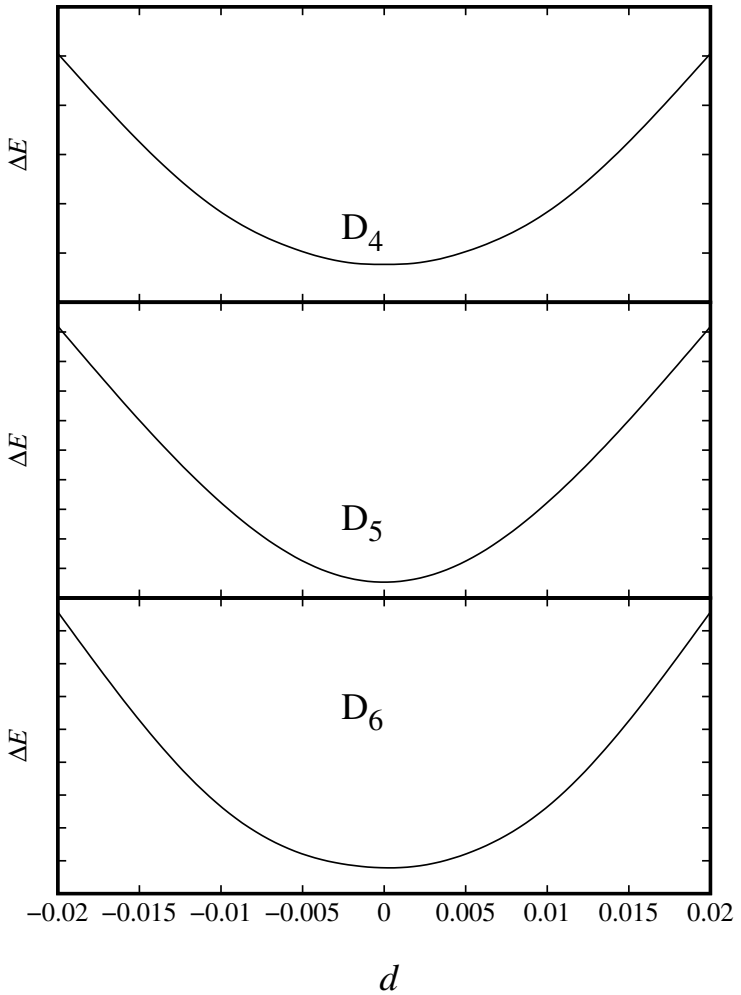


Figure 4.6. Changes in the strain energy as a function of strain using distortion matrix D_4 (4.7), D_5 (4.8), and D_6 (4.9).

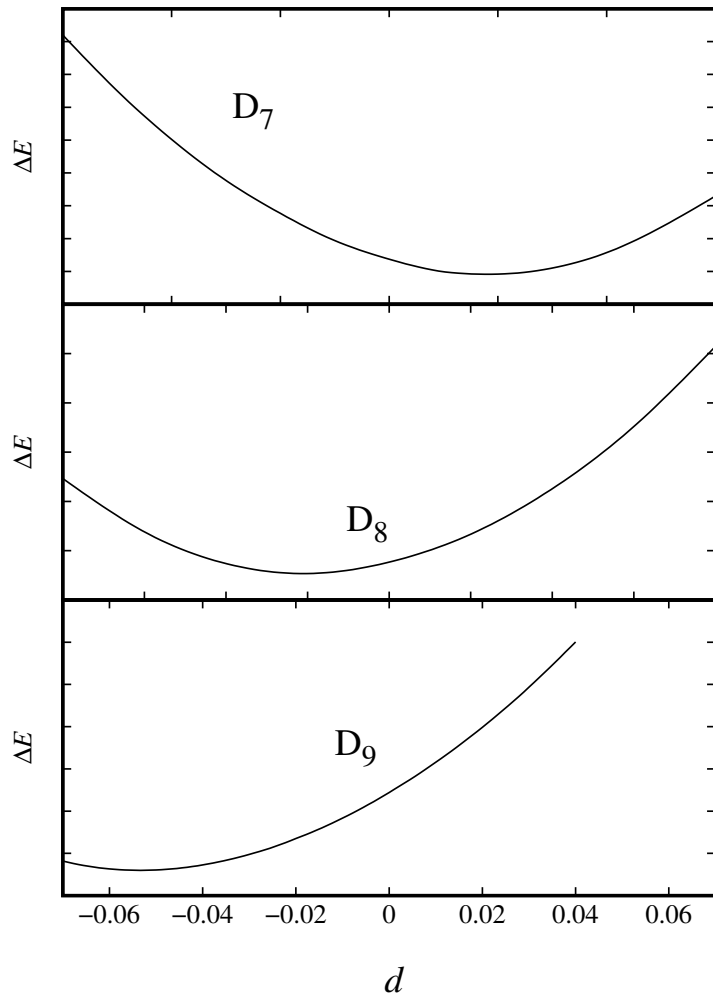


Figure 4.7. Changes in the strain energy as a function of strain using distortion matrix D_7 (4.11), D_8 (4.12), and D_9 (4.13).

Appendix: Elastic Parameter Calculation for γ -uranium

Applying a small strain (δ) to the equilibrium lattice changes the total energy, and from this information, the elastic parameters are deduced. The distortion of a lattice vector follows the rule $\mathbf{R}' = \mathbf{RD}$. Here, \mathbf{R} is the Bravais lattice vector, \mathbf{R}' is a matrix containing the components of the distorted lattice vectors, and \mathbf{D} is the symmetric distortion matrix.

By symmetry, there are only three independent elastic parameters for a cubic system (*i.e.*, C_{11} , C_{12} , and C_{44}). Elastic parameters are evaluated from the total energy of the crystal, to which volume-conserving orthorhombic [$C' = (C_{11} - C_{12})/2$] and monoclinic (C_{44}) distortions are applied. The relevant distortion matrices are

$$\mathbf{D}_{\text{ortho}} = \begin{bmatrix} 1 + \delta_o & 0 & 0 \\ 0 & 1 - \delta_o & 0 \\ 0 & 0 & \frac{1}{1-\delta_o^2} \end{bmatrix} \quad (4.17)$$

and

$$\mathbf{D}_{\text{mono}} = \begin{bmatrix} 1 & \delta_m & 0 \\ \delta_m & 1 & 0 \\ 0 & 0 & \frac{1}{1-\delta_m^2} \end{bmatrix}. \quad (4.18)$$

The associated total energy change for an orthorhombic distortion is

$$\Delta E = V(C_{11} - C_{12})\delta_o^2 + O(\delta_o^4). \quad (4.19)$$

For a monoclinic distortion, the energy change is

$$\Delta E = 2VC_{44}\delta_m^2 + O(\delta_m^4). \quad (4.20)$$

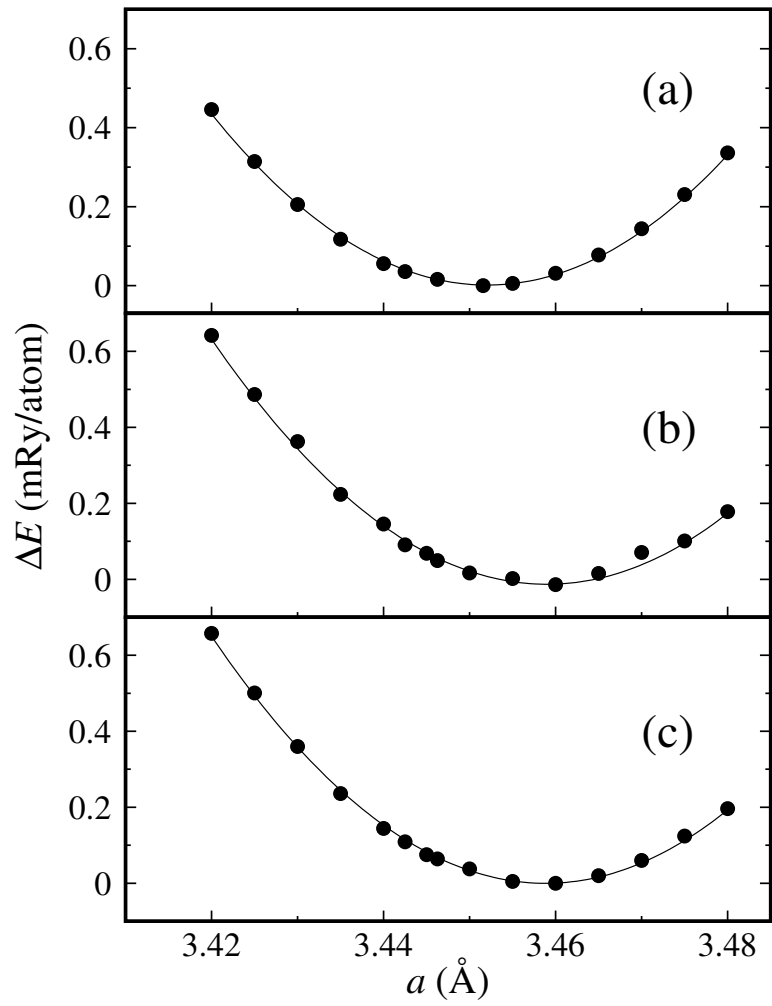


Figure 4.8. Energy as a function of lattice parameter for γ -uranium. (a) this work with a k -point mesh of $30 \times 30 \times 30$; (b) Pseudopotential from PS library [24, 25] with a k -point mesh of $30 \times 30 \times 30$; (c) Pseudopotential from PS library [24, 25] with $42 \times 42 \times 42$ k -point mesh.

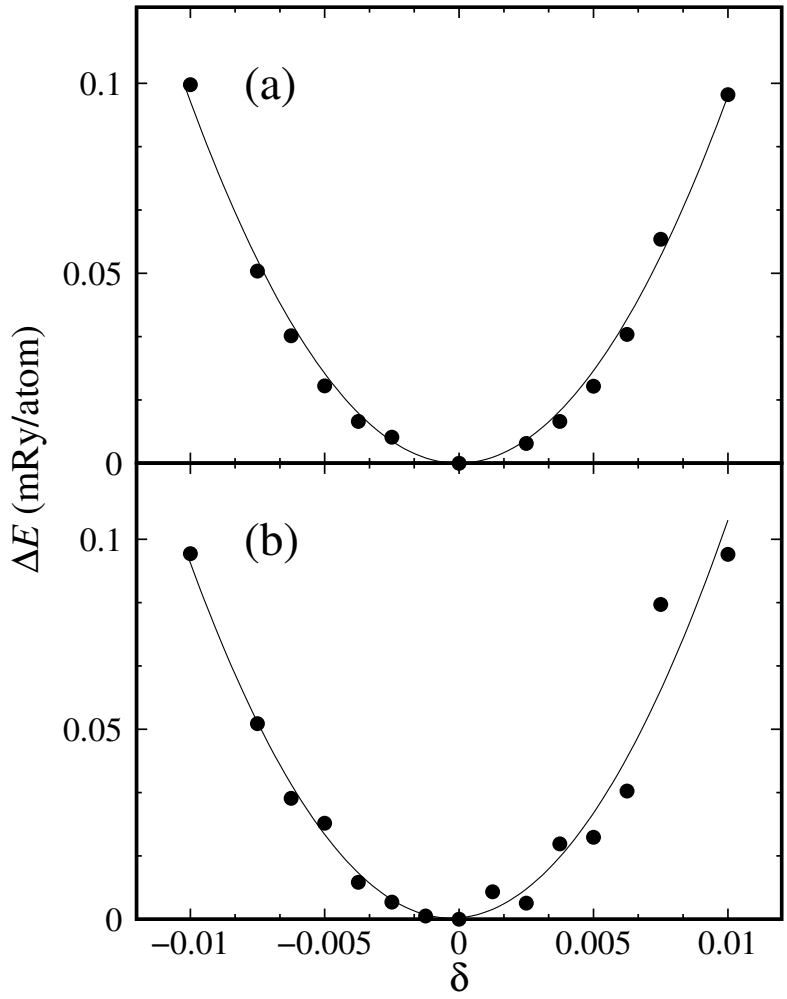


Figure 4.9. Changes in the strain energy as a function of strain (δ) for monoclinic distortions of γ -uranium (Eq. (4.18) and Eq. (4.20)). (a) this work; (b) Pseudopotential from the PS library [24, 25]. Increasing the number of k -points does not improve the smoothness of plot (b).

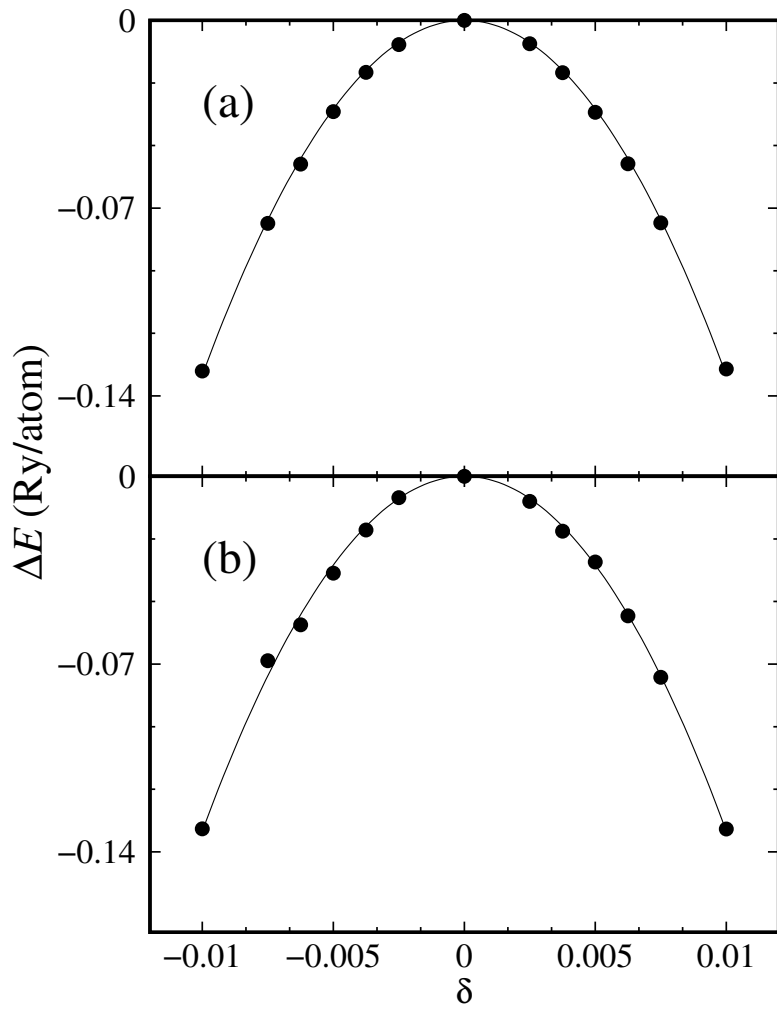


Figure 4.10. Changes in the strain energy as a function of strain (δ) for orthorhombic distortions of γ -uranium (Eq. (4.17) and Eq. (4.19)). (a) this work; (b) Pseudopotential from the PS library [24, 25].

References

1. P. Söderlind, O. Eriksson, B. Johansson, J. M. Wills, and A. M. Boring, *Nature* **374**, 524 (1995).
2. A. C. Lawson, C. E. Olsen, J. W. Richardson, M. H. Mueller, and G. H. Lander, *Acta Crystallogr. B* **44**, 89 (1988).
3. J. Akella, S. Weir, J. M. Wills, and P. Söderlind, *J. Phys. Condens. Matter* **9**, L549 (1997).
4. G. H. Lander, *Science* **301**, 1057 (2003).
5. A. J. Freeman and G. H. Lander, *Handbook on the Physics and Chemistry of the Actinides*, Vol. 1,2 (North-Holland, Amsterdam, 1984).
6. J. M. Wills and O. Eriksson, *Phys. Rev. B* **45**, 13879 (1992).
7. O. Eriksson, P. Söderlind, J. M. Wills, and A. M. Boring, *Phys. C Supercond.* **190**, 5 (1993).
8. P. Söderlind, O. Eriksson, B. Johansson, and J. M. Wills, *Phys. Rev. B* **50**, 7291 (1994).
9. J. P. Crocombette, F. Jollet, L. Thien Nga, and T. Petit, *Phys. Rev. B* **64**, 104107 (2001).
10. P. Söderlind, *Phys. Rev. B* **66**, 085113 (2002).
11. A. C. Lawson, B. Martinez, J. A. Roberts, B. I. Bennett, and J. W. Richardson, Jr., *Philos. Mag. B* **80**, 53 (2000).
12. M. D. Jones, J. C. Boettger, R. C. Albers, and D. J. Singh, *Phys. Rev. B* **61**, 4644 (2000).
13. C. D. Taylor, *Phys. Rev. B* **77**, 094119 (2008).
14. P. E. Blöchl, *Phys. Rev. B* **50**, 17953 (1994).
15. J. P. Perdew, J. A. Chevary, S. H. Vosko, K. A. Jackson, M. R. Pederson, D. J. Singh, and C. Fiolhais, *Phys. Rev. B* **46**, 6671 (1992).
16. J. P. Perdew, J. A. Chevary, S. H. Vosko, K. A. Jackson, M. R. Pederson, D. J. Singh, and C. Fiolhais, *Phys. Rev. B* **48**, 4978 (1993).
17. C. S. Barrett, M. H. Mueller, and R. L. Hitterman, *Phys. Rev.* **129**, 625 (1963).
18. S. Xiang, H. Huang, and L. Hsiung, *J. Nucl. Mater.* **375**, 113 (2008).
19. J. P. Perdew, K. Burke, and M. Ernzerhof, *Phys. Rev. Lett.* **77**, 3865 (1996).

20. J. P. Perdew, K. Burke, and M. Ernzerhof, Phys. Rev. Lett. **78**, 1396 (1997).
21. J. H. Li, Q. B. Ren, C. H. Lu, L. Lu, Y. Dai, and B. X. Liu, J. Alloy Compd. **516**, 139 (2012).
22. J. P. Perdew and Y. Wang, Phys. Rev. B **45**, 13244 (1992).
23. B. Beeler, C. Deo, M. Baskes, and M. Okuniewski, J. Nucl. Mater. **433**, 143 (2013).
24. QUANTUM ESPRESSO, PS library,
<http://www.quantum-espresso.org/pseudopotentials> (2019).
25. A. Dal Corso, Comput. Mater. Sci. **95**, 337 (2014).
26. P. Giannozzi, S. Baroni, N. Bonini, M. Calandra, R. Car, C. Cavazzoni, D. Ceresoli, G. L. Chiarotti, M. Cococcioni, I. Dabo, A. Dal Corso, S. de Gironcoli, S. Fabris, G. Fratesi, R. Gebauer, U. Gerstmann, C. Gougaussis, A. Kokalj, M. Lazzeri, L. Martin-Samos, N. Marzari, F. Mauri, R. Mazzarello, S. Paolini, A. Pasquarello, L. Paulatto, C. Sbraccia, S. Scandolo, G. Sclauzero, A. P. Seitsonen, A. Smogunov, P. Umari, and R. M. Wentzcovitch, J. Phys. Condens. Matter **21**, 395502 (2009),
<http://www.quantum-espresso.org/>.
27. N. A. W. Holzwarth, A. R. Tackett, and G. E. Matthews, Comput. Phys. Commun. **135**, 329 (2001).
28. A. R. Tackett, N. A. W. Holzwarth, and G. E. Matthews, Comput. Phys. Commun. **135**, 348 (2001).
29. P. Söderlind, B. Sadigh, V. Lordi, A. Landa, and P. E. A. Turchi, J. Nucl. Mater. **444**, 356 (2014).
30. N. Iché-Tarrat and C. J. Marsden, J. Phys. Chem. A **112**, 7632 (2008).
31. A. M. Rappe, K. M. Rabe, E. Kaxiras, and J. D. Joannopoulos, Phys. Rev. B **41**, 1227 (1990).
32. Naval Research Laboratories, Structure of Crystals, <http://aflowlib.duke.edu/users/egossett/lattice/> (2015).
33. H. J. Monkhorst and J. D. Pack, Phys. Rev. B **13**, 5188 (1976).
34. M. Methfessel and A. T. Paxton, Phys. Rev. B **40**, 3616 (1989).
35. P. Ravindran, L. Fast, P. A. Korzhavyi, B. Johansson, J. Wills, and O. Eriksson, J. Appl. Phys. **84**, 4891 (1998).
36. O. Beckstein, J. E. Klepeis, G. L. W. Hart, and O. Pankratov, Phys. Rev. B **63**, 134112 (2001).
37. G. H. Lander, E. S. Fisher, and S. D. Bader, Adv. Phys. **43**, 1 (1994).

38. T. Le Bihan, S. Heathman, M. Idiri, G. H. Lander, J. M. Wills, A. C. Lawson, and A. Lindbaum, Phys. Rev. B **67**, 134102 (2003).
39. G. Kresse and J. Hafner, Phys. Rev. B **47**, 558 (1993).
40. G. Kresse and J. Furthmüller, Comput. Mater. Sci. **6**, 15 (1996).
41. G. Kresse and J. Furthmüller, Phys. Rev. B **54**, 11169 (1996).
42. F. D. Murnaghan, Proc. Natl. Acad. Sci. U. S. A. **30**, 244 (1944).
43. R. Q. Hood, L. H. Yang, and J. A. Moriarty, Phys. Rev. B **78**, 024116 (2008).
44. C.-S. Yoo, H. Cynn, and P. Söderlind, Phys. Rev. B **57**, 10359 (1998).
45. E. S. Fisher and H. J. McSkimin, J. Appl. Phys. **29**, 1473 (1958).
46. A. S. Wilson and R. E. Rundle, Acta Crystallogr. **2**, 126 (1949).
47. H. L. Yakel, *Review of X-ray Diffraction Studies in Uranium Alloys*, Tech. Rep. CONF-740205-9 (Oak Ridge National Laboratory, 1973).
48. I. Grenthe, J. Drozdzynski, T. Fujino, E. C. Buck, T. E. Albrecht-Schmitt, and S. F. Wolf, *The Chemistry of the Actinide and Transactinide Elements*, Vol. 1 (Springer, Dordrecht, 2006) pp. 253–698.
49. J. H. Kittel, B. R. T. Frost, J. P. Mustelier, K. Q. Bagley, G. C. Crittenden, and J. Van Dievoet, J. Nucl. Mater. **204**, 1 (1993).
50. N.-T. H. Kim-Ngan and L. Havela, J. Sci. Adv. Mater. Dev. **1**, 121 (2016).
51. M. Born, Proc. Camb. Phil. Soc. **36**, 160 (1940).
52. M. Born and K. Huang, *Dynamical Theory of Crystal Lattices* (Clarendon Press, 1954).
53. F. Mouhat and F.-X. Coudert, Phys. Rev. B **90**, 224104 (2014).
54. P. Söderlind, Adv. Phys. **47**, 959 (1998).
55. C. W. Tucker, Jr., *An Approximate Crystal Structure for the Beta Phase of Uranium*, Tech. Rep. KAPL-388 (Knolls Atomic Power Laboratory, 1950).
56. C. W. Tucker, Acta Crystallogr. **4**, 425 (1951).
57. J. Donohue and H. Einspahr, Acta Crystallogr. B **27**, 1740 (1971).
58. J. Donohue, *Structures of the Elements* (John Wiley and Sons, New York, 1974) pp. 134–148.
59. D. C. Wallace, *Thermodynamics of Crystals* (Courier Corporation, 1998).
60. A. R. M. Iasir and K. D. Hammond, Comput. Mater. Sci. **171**, 109221 (2020).

CHAPTER 5

XENON MOBILITY IN BCC-URANIUM AND URANIUM-MOLYBDENUM ALLOYS

This chapter has been submitted as journal article for peer review. The authors are A. Rafi M Iasir and Karl D. Hammond of the University of Missouri.

5.1 Introduction

High-performance research reactors require high-enrichment uranium (HEU) fuels to attain the desired neutron flux. The replacement of HEU fuels with low-enrichment uranium (LEU) is an important antiproliferation initiative. The United States High-Performance Research Reactor (USHPRR) program is currently aiming to replace the HEU fuels currently used in high performance reactors with LEU fuels [1]. LEU fuels require a higher uranium density than that of uranium oxides to compensate for the decrease in ^{235}U enrichment. Metallic uranium shows great promise in this regard.

Metallic fuels are usually chosen because of their high thermal conductivity and high density. Isotropic swelling behavior is desirable, but uranium, like other light actinides (Pa–Pu), has a low-symmetry crystal structure (the orthorhombic α phase) at ambient temperature and pressure, which results in anisotropic thermal and radiation-induced expansion. Pure uranium has three allotropes at atmospheric pressure: α (base-centered orthorhombic), β (tetragonal), and γ (body-centered cubic). At atmospheric pressure, α -uranium transforms to β -uranium at

approximately 935 K, and β -uranium transforms to γ -uranium at approximately 1045 K [2, 3].

The γ -uranium allotrope (which is body-centered cubic) is preferred to α -uranium by nuclear engineers because it undergoes both isotropic thermal expansion and isotropic radiation-induced swelling [4]. It is not possible to retain pure γ -uranium under the required processing and radiation conditions; however, a metastable bcc phase can be obtained at room temperature by alloying with molybdenum [5–8]. A study by Kim-Ngan and Havela [9] showed that the bcc structure can also be retained at temperatures below the ordinary phase transition temperature by alloying uranium with metals such as platinum, palladium, niobium, and zirconium. Molybdenum stabilizes uranium's γ phase at concentrations near the eutectoid point (11.1 wt% Mo) and lowers the phase transition temperature from 1045 K for pure γ -uranium to 828 K for a U–Mo alloy at the eutectoid point [10, 11]. Uranium alloyed with 10 wt% molybdenum (U-10Mo, which is 21.6 at.% molybdenum) is currently being developed as a potential high-density, low-enrichment uranium fuel for high-performance research reactors [12–14].

Uranium–molybdenum alloys have been studied extensively both experimentally [6, 15, 16] and theoretically [17–21]. Castellano *et al.* [22] showed that the addition of molybdenum to uranium leads to the stabilization of the γ phase using *ab initio* molecular dynamics. This thermodynamic stabilization is important because un-alloyed γ -uranium is not stable under fuel preparation and irradiation conditions [6, 8]. Fission creates a variety of products, resulting in gas bubbles, metallic precipitates, and solutes in the fuel matrix. Among the many fission products, fission gas (*i.e.*, xenon and krypton) produces some of the most significant challenges associated with nuclear fuel development. Fission gas influences the thermal conductivity, causes swelling, and impacts the neutron economy of the reactor [23, 24]. The ratio of xenon to krypton in fission gases is typically nine to

one [25]. The most important fission gas isotopes with short half lives are ^{133}Xe (5.25 d) and ^{135}Xe (9.1 h). In particular, ^{135}Xe has a very high neutron absorption cross-section ($\sigma_a = 2.7 \times 10^6 \pm 0.1$ barns) that can lower the fuel's reactivity. Hence, the evolution of fission gases is directly related to the fuel performance.

Large fission gas atoms (*i.e.*, xenon) are mostly insoluble in the fuel matrix [26, 27]. There is a significant driving force for segregation of fission gas atoms to defects such as grain boundaries or dislocations, and consequently gas bubbles form at these sinks. Post-irradiation analysis of U–Mo alloys showed that the fission gases distribute themselves both inside the grains and along grain boundaries [28–31]. Fission gas in U–Mo alloys also forms superlattices, in which the bubbles distribute themselves in an organized array [31, 32]. To understand the mechanism of the formation of gas-bubble superlattices, the rate-limiting processes involved in fission gas transport need to be studied. One of these processes is the motion of individual gas atoms through the fuel matrix, assisted by vacancies.

The behavior of fission gas has been extensively researched for common fuels such as UO_2 [33–37]. A number of theoretical approaches have also been used to understand the behavior of fission products in UO_2 , including electronic structure theory [26, 27, 38–44]. In particular, vacancies play an important role in the diffusion of xenon because of its size relative to the metal atoms.

Solute diffusion in light actinides is a very interesting phenomenon because such solutes typically have very high diffusivities [45–47]. Diffusion of solutes in metallic uranium has not been studied extensively. However, there are some early works that provide some information about defect and impurity diffusion in uranium [48–55]. Recently, Smirnova *et al.* [56] studied self-diffusion in γ -uranium and U–Mo alloys using molecular dynamics. They showed that diffusion in γ -uranium, like that in other light actinides, is anomalously fast compared to bcc transition metals.

In recent years, there have been many attempts to calculate diffusion coefficients of impurities using electronic structure and atomistic methods [57–64]. Electronic structure calculations based on DFT and multi-frequency models have shown their usefulness in various works. Five-frequency models of face-centered cubic crystals [65–67] and nine-frequency (or sometimes four-frequency) models of bcc crystals [68, 69] have been widely used. Methods based on electronic structure theory involve calculating the activation energies of an atom jumping to a vacancy in one of the atom’s nearest-neighbor positions. This is often referred to as vacancy-mediated diffusion. The calculations employed here are based on DFT coupled with classical transition state theory (TST), which treats vibration using the harmonic oscillator approximation [70, 71].

In this study, we use DFT and TST to study the diffusion of xenon and molybdenum in γ -uranium alloys such as U-7Mo and U-10Mo by varying the local molybdenum concentration around the diffusing solute atom. We find that molybdenum’s migration energy is much higher than xenon’s in γ -U alloys and that the presence of molybdenum in the local environment of a xenon atom tends to decrease the mobility of xenon in γ -uranium alloys. We also calculate the vacancy–solute binding energies of several solutes in γ -uranium and find that such binding energies are generally higher in γ -uranium than in iron or aluminum.

5.2 Theory

Diffusion coefficients in crystalline solids are often described by an Arrhenius equation over a wide range of temperatures. This model consists of two parameters, the migration energy, E_m , and the pre-exponential factor, D_0 , with the diffusion coefficient given by

$$D = D_0 e^{-E_m/k_B T}, \quad (5.1)$$

where k_B is the Boltzmann constant and T is the absolute temperature. If D_0 is independent of temperature, an Arrhenius plot (D against $1/T$) gives a straight line; if D_0 changes with T , it yields a curve that falls away from the constant- D_0 line at high temperature (the left of the plot).

The migration energy is the activation energy for an atom to jump onto a nearby vacancy. According to classical transition state theory (TST), the rate at which a vacancy exchanges its place with a neighboring atom can be expressed by the Eyring–Polanyi equation [71–73],

$$v = v^\ddagger \exp\left(\frac{-\Delta G_m}{k_B T}\right) \approx \frac{k_B T}{h} \frac{Q_{TS}}{Q_{IS}} \exp\left(\frac{-E_m}{k_B T}\right) \approx \frac{k_B T}{h} \exp\left(\frac{-E_m}{k_B T}\right), \quad (5.2)$$

where Q_{IS} is the vibrational partition function of the initial state and Q_{TS} is the vibrational partition function of the transition state with the vibrational mode along the minimum-energy pathway removed. In the current work, we did not calculate the jump frequencies, which are part of the Q_i terms; we instead make the approximation that the vibrational partition functions not associated with the minimum energy pathway are unity (*i.e.*, $Q_{TS}/Q_{IS} \approx 1$). The diffusion coefficient is proportional to the rate of a jump: $D = v\lambda^2/6$, where $\lambda = a/\sqrt{8}$ for bcc lattices [74] and a is the lattice parameter.

Metals that undergo irradiation have point defects such as self-vacancies and self-interstitials in the lattice. The diffusion of these defects results in microstructural changes that can impact the mechanical properties. The diffusion of vacancies is of significant interest because they form voids, dislocation loops, and clusters, and they facilitate the diffusion of substitutional solute atoms. This method of solute diffusion is controlled by the interaction between a vacancy and a solute atom. The diffusion of vacancies is particularly influenced by the presence of nearby substitutional solute atoms. Sometimes the vacancy and the solute can coexist as an

atom–vacancy complex. Hence, understanding solute–vacancy interactions is an important step in developing models of diffusion in irradiated materials [75, 76]. The authors are not aware of any previous results regarding solute–vacancy binding in γ -uranium for any solutes, so we calculated them as part of this work.

We used defects in supercells to calculate the binding energies of solute–vacancy ($X-\square$) pairs. The binding energy is the difference between the energy at infinite separation and the energy at nearest-neighbor separation. We used the following expression to calculate the binding energy of a solute to a vacancy:

$$E_b^{X-\square} = E_{U_{N-1}}^{X_1} + E_{U_{N-1}}^{\square_1} - E_{U_{N-2}}^{X_1 \square_1} - E_{U_N}. \quad (5.3)$$

For a bcc supercell with N sites, the cell may contain no defects (energy E_{U_N}), or it may contain a vacancy (energy $E_{U_{N-1}}^{\square_1}$), a solute impurity ($E_{U_{N-1}}^{X_1}$), or a solute–vacancy pair ($E_{U_{N-2}}^{X_1 \square_1}$). A positive binding energy means the complex is bound. Equation (5.3) can also be conveniently written as the energy required to form a vacancy next to a solute (X) atom. The vacancy formation energy is

$$E_f^{\square} = E_{U_{N-1}}^{\square_1} - \frac{N-1}{N} E_{U_N}, \quad (5.4)$$

where E_{U_N} is the energy of a supercell with N uranium atoms. A positive formation energy indicates that energy must be added to form the vacancy.

The disordered nature of U–Mo alloys creates some challenges for electronic structure studies. The manner in which molybdenum is distributed among the lattice sites produces different diffusion pathways for xenon, and there are several ways to arrange molybdenum atoms on the lattice sites around a particular xenon atom. We use a combinatorial approach to estimate the probabilities (Table 5.1) of having various numbers of molybdenum atoms in the first-nearest-neighbor shell of the bcc structure around a xenon atom. Assuming the molybdenum atoms are

Table 5.1. Probability of having different numbers of molybdenum atoms in the nearest-neighbor (NN) location for a bcc uranium–molybdenum alloy. We have used Eq. (5.5) to calculate the probabilities.

# of Mo	U-10Mo ($x_{\text{Mo}} = 0.216$)	U-7Mo ($x_{\text{Mo}} = 0.157$)
0	0.182	0.302
1	0.351	0.394
2	0.290	0.221
3	0.133	0.069
4	0.037	0.013
5	0.006	0.001
6	0.0006	8.95×10^{-5}
7	2.19×10^{-5}	2.39×10^{-6}

arranged randomly, the probability (\mathcal{P}) of a particular U/Mo combination on the sites near a xenon atom can be calculated using a binomial distribution:

$$\mathcal{P} = \binom{n}{k} x_{\text{Mo}}^k (1 - x_{\text{Mo}})^{n-k}, \quad (5.5)$$

where n is the number of available nearest-neighbor positions not occupied by the vacancy (for bcc, $n = 7$), k is the number of molybdenum atoms in the nearest-neighbor shell, and x_{Mo} is the (overall) mole fraction of molybdenum. According to Table 5.1, the probability (\mathcal{P}) of having more than three molybdenum atoms in the first nearest-neighbor shell is low (< 5%). We assume, for simplicity, that $x_{\text{Xe}} \approx 0$.

5.3 Methodology

All calculations used the QUANTUMESPRESSO [77] simulation package with the projector augmented wave (PAW) method [78]. A full description of the uranium pseudopotential can be found in our earlier work [79]. For the elements Mo, Xe, Fe, Co, Au, Nb, and Zr, we used PAW-based pseudopotentials from the QUANTU-

`mESPRESSO` PS Library [80, 81]. We used the exchange–correlation functional of Perdew, Burke, and Ernzerhof (PBE) [82, 83] for all calculations.

DFT calculates the ground state properties of a system; however, γ -uranium is mechanically unstable at low temperatures, which results in negative shear moduli [84]. Other elements (*e.g.*, Ti, Zr, Pr, and Hf) also have high-temperature bcc structures that are unstable at low temperature [85, 86]. It is consequently challenging to study γ -uranium with DFT, particularly using a supercell that includes vacancies or defects. To perform our calculations, we used the so-called shell method [87], in which the outer layer of atoms is fixed at crystallographic coordinates and the rest of the atoms are allowed to move freely. We used a $3 \times 3 \times 3$ supercell of bcc uranium, which consists of 54 atoms in the absence of heteroatoms or vacancies. A convergence test showed that a Monkhorst–Pack [88] k -point mesh of $5 \times 5 \times 5$ is suitable to yield formation and migration energies that are converged to within 0.01 eV/ \AA .

To calculate the migration energy, each initial state was relaxed with respect to internal coordinates and volume. We determined the transition state by way of a nudged elastic band (NEB) [89, 90] calculation with a climbing image as implemented in QUANTUMESPRESSO. We used five images in the NEB calculations.

5.4 Results and Discussion

5.4.1 Vacancy Formation and Impurity–Vacancy Binding Energies

The formation energy of a single vacancy is calculated using Eq. (5.4). Our results are compared with previously-published DFT calculations and experimental results in Table 5.2. Our results are in good agreement with both previous DFT studies. Xian *et al.* [91] also used 54 atoms in their supercell, but our vacancy formation energy is higher by 0.2 eV. Discrepancies could arise from their use of a $6 \times 6 \times 6$ k -point mesh, whereas we used $5 \times 5 \times 5$. Beeler *et al.* [87] used a supercell

Table 5.2. Vacancy formation energy (eV) of γ -uranium compared with previously-published results.

Source	Energy (eV)
Present work	1.28
Beeler <i>et al.</i> [87]	1.384
Xian <i>et al.</i> [91]	1.08
Matter <i>et al.</i> (expt.) [92]	1.2 ± 0.3
Lund <i>et al.</i> (expt.) [93]	1.6 ± 0.2

of 128 atoms to calculate the vacancy formation energy. The experimental values bracket our results and those of Beeler *et al.* [87]: The earlier work of Matter *et al.* [92] found a formation energy of 1.2 ± 0.3 eV, whereas Lund *et al.* [93] found 1.6 ± 0.2 eV.

We are not aware of any previous reports of calculations of solute–vacancy ($X-\square$) binding energies in γ -uranium, so we calculated these ourselves. We chose solutes so as to compare to diffusion measurements by Rothman and coworkers [49–51]. The results are shown in Table 5.3. All of the solute–vacancy binding energies in γ -uranium are substantially higher than in other bcc metals. For example, in iron and tungsten, the $X-\square$ binding energy varies from -0.6 to 0.6 eV for a variety of solutes [94–97]. In γ -uranium, however, the binding energy varies from 5.715 eV (Fe– \square) to 6.619 eV (Cr– \square), which indicates that the solute–vacancy binding energy is much higher in bcc uranium than it is in other bcc metals.

The solute–vacancy binding energy characterizes the interaction between a solute and a vacancy, which modifies the local concentration of vacancies near a solute. In the case of γ -uranium, the interaction between solute and vacancy is strongly attractive. The total solute–vacancy binding energy can be decomposed into two factors: elastic effects and electrostatic effects [98]. The elastic energy (or elastic binding energy) is the energy that is released if the strain fields of a

Table 5.3. Solute–vacancy binding energies in γ -uranium for various solutes near a vacancy. Positive energies indicate energetically-favorable binding.

Solute	Binding energy (eV)
Xe	6.034
Mo	6.249
Fe	5.715
Co	5.876
Au	6.450
Cr	6.619
Zr	6.318
Nb	6.113

solute and a vacancy interact [95, 97]. Due to the unstable nature of γ -uranium at low temperatures, the elastic binding energy contributes the most to the total solute–vacancy binding energy and is the primary reason for the high value of the solute–vacancy binding energy in bcc uranium.

5.4.2 Xenon and Molybdenum Diffusion

Migration energies are calculated using the climbing-image nudged elastic band method. We calculated the migration energies of xenon and molybdenum moving from the center of the supercell to one of the nearest-neighbor lattice sites. Such solute–vacancy exchange is the primary mechanism of diffusion of xenon and molybdenum because of their size relative to uranium. Table 5.4 presents our findings. Note that in bcc lattices, all eight nearest-neighbor sites are symmetrically equivalent, so there is only one unique migration energy for xenon near seven uranium atoms and one vacancy. As the amount of molybdenum in the nearest-neighbor shell increases, there are more and more symmetrically distinct migration pathways. Xenon’s migration energy in the absence of any molybdenum in the nearest-neighbor positions is significantly lower than molybdenum’s migration energy. The Xe– \square binding energy is also lower than the Mo– \square binding energy,

Table 5.4. Xenon migration energy (E_m) for different configurations.

Composition ^a	Xe Jump	E_m (eV)
7 U	$\langle 1\ 1\ 1 \rangle$ (Fig. 5.1a)	0.161
1 Mo	1 (Fig. 5.1b)	0.313
	2 (Fig. 5.1b)	0.172
	3 (Fig. 5.1b)	0.261
2 Mo	1 (Fig. 5.2a)	0.110
	2 (Fig. 5.2a)	0.212
	3 (Fig. 5.2b)	0.532
	4 (Fig. 5.2b)	0.108
	5 (Fig. 5.2b)	0.224
	6 (Fig. 5.2c)	0.110
3 Mo	1 (Fig. 5.3a)	0.515
	2 (Fig. 5.3a)	0.917
	3 (Fig. 5.3a)	0.265
	4 (Fig. 5.3a)	0.579
	5 (Fig. 5.3b)	0.201
	6 (Fig. 5.3b)	0.384
	7 (Fig. 5.3b)	0.386
	8 (Fig. 5.3c)	1.213
	9 (Fig. 5.3c)	0.461
	10 (Fig. 5.3c)	0.435
	Mo Jump	E_m (eV)
7 U	$\langle 1\ 1\ 1 \rangle$ (Fig. 5.1a)	2.067

^aThe eight nearest-neighbor sites consist of one vacancy plus the atoms listed, with the remaining sites occupied by uranium atoms.

which may occur in part because xenon tends to find its energetic minimum location in between the empty lattice site and the site closest to the xenon atom, resulting in shorter jump distances and lower barriers.

We studied the xenon migration energy in the presence of molybdenum in a systematic way by including various numbers of molybdenum atoms in the nearest-neighbor (NN) shell around a xenon atom and calculating all symmetrically distinct xenon migration energies associated with each distinct arrangement of

molybdenum atoms around a central xenon atom. One molybdenum in the NN shell creates three symmetrically equivalent xenon jumps (see Fig. 5.1b). These three migration pathways (labeled 1, 2, and 3) show higher activation energies than the case with no molybdenum atoms in the NN shell.

In the presence of a vacancy, xenon tends to take a position in between the vacancy and lattice site at the energy minimum. This results in a very low migration energy for xenon to move to the nearest vacancy. This behavior is very similar to how xenon moves in UO_2 fuel: in UO_2 , the xenon atoms prefer to find their lowest energy location in between the original trap site and the second uranium vacancy [27]. Adding one molybdenum to the nearest neighbor shell increases the migration energies for all three unique migration pathways. The relative locations of the molybdenum atom and the vacancy change the minimum energy location of the xenon atom. Xenon tends to relax towards the vacancy and the extra space created by the molybdenum atom. It finds a low-energy site in between its original site, the vacancy, and the molybdenum atom, which increases the migration energy.

There is more than one way to put two molybdenum atoms in the NN shell around a solute atom in a bcc crystal, and three of these arrangements create distinct xenon migration pathways. Figure 5.2 shows all symmetrically-distinct locations for two molybdenum atoms around a xenon atom and the resulting symmetrically-distinct jumps that could result if a vacancy were in another position nearby. Migration energies with two molybdenum atoms present range from 0.110 eV to 0.532 eV. Both the positions of the two molybdenum atoms and the direction of the jump influence the migration energy. Directions 1 and 2 (Fig. 5.2a) have migration energies of 0.110 and 0.212 eV, respectively; direction 2 has almost double the migration energy of direction 1. Directions 1, 4, and 6, which all have a molybdenum atom on the corner of the cube adjacent to the vacancy, have the lowest migration energies. The lowest-energy locations for xenon for jumps in

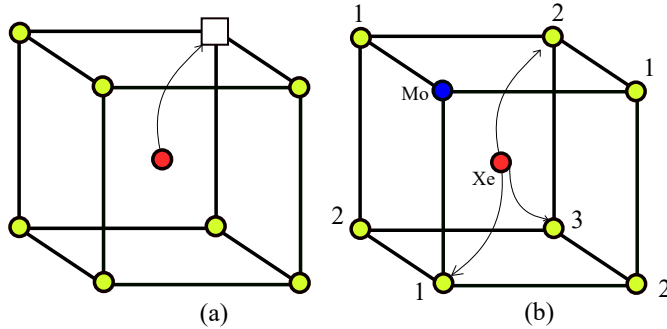


Figure 5.1. Diagram of a xenon jump from the center site to a nearest-neighbor vacancy in γ -uranium. (a) All eight jumps are symmetrically equivalent with no molybdenum present; (b) with one molybdenum atom in the nearest-neighbor shell, there are three unique solute jumps (1, 2, and 3).

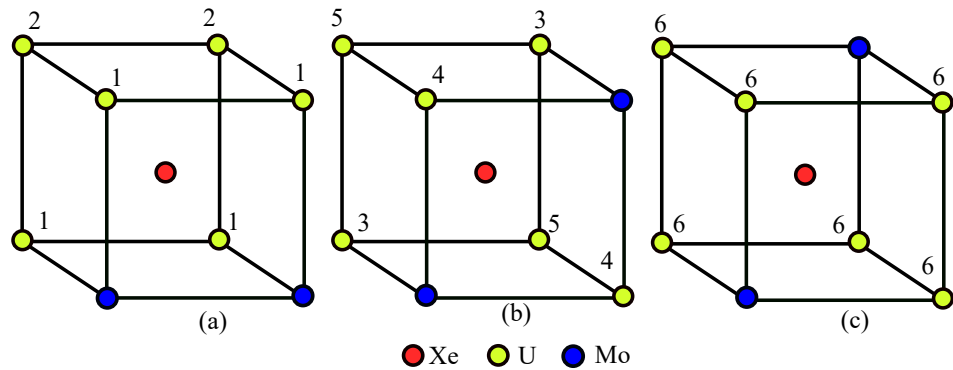


Figure 5.2. The three sets of symmetrically-inequivalent hops of xenon from the center with two molybdenum atoms in the nearest-neighbor shell. The numbers denote symmetrically distinct pathways.

directions 1, 4, and 6 are close to each other, which produces a very low migration energy.

Figure 5.3 shows the symmetrically-distinct arrangements of three molybdenum atoms in the nearest-neighbor shell. This local concentration creates ten distinct jumps of a xenon atom to a nearest-neighbor vacancy (Fig. 5.3). The migration energies for three-molybdenum configurations vary from 0.201 eV for direction 5 to 1.213 eV for direction 8. The highest migration energy is for a xenon atom that jumps to a site between two molybdenum atoms (site 8 in Fig. 5.3c). Figure 5.3a

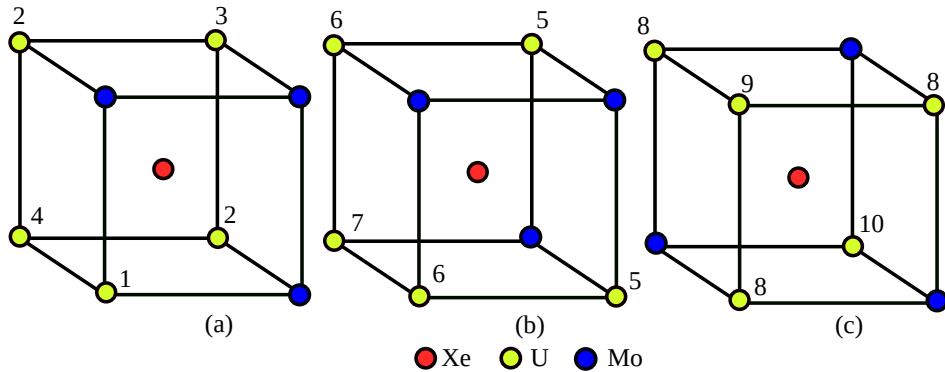


Figure 5.3. The three sets of symmetrically-distinct hops from the center site with three molybdenum atoms in the nearest-neighbor shell. The numbers denote symmetrically distinct pathways.

shows the arrangements of three molybdenum atoms on the same (100) plane, which produces four distinct jumps with migration energies ranging from 0.515 eV to 0.917 eV, the highest one being for direction 2, where xenon moves to the opposite corner from the three molybdenum atoms. Figure 5.3b has a combination of two molybdenum atoms on one face of the cell and one molybdenum atom in the lower corner on the opposite site. This configuration reduces the migration energy compared to the configuration in which all three molybdenum atoms are co-planar. Direction 8 (Figure 5.3c) produces the highest migration energy for xenon. In this configuration, the initial minimum energy position for xenon is equidistant from all three molybdenum atoms. The final position is not equidistant but creates a larger activation energy. In the cases of directions 9 and 10, the location of the vacancy changes the lowest-energy location (final position) for xenon and reduces the barrier.

We did not calculate the migration energy of xenon with more than three molybdenum atoms in the nearest-neighbor shell. The assumption of a random (binomial) distribution (Table 5.1) implies that the probability of having 0–3 molybdenum

atoms near a xenon solute is much higher (> 96%) than having more than three molybdenum atoms for either U-10Mo or U-7Mo.

5.5 Conclusions

We calculated solute–vacancy binding energies for different solutes in bcc uranium. Uranium shows relatively high vacancy–solute binding energies compared to iron and aluminum. The unstable nature of γ -uranium at low temperature contributes to a significant increase in solute–vacancy binding energy relative to other bcc metals. The higher elastic binding energy in bcc uranium produces a high solute–vacancy binding energy.

We also calculated migration energies of xenon and molybdenum in pure bcc uranium. Molybdenum’s migration energy is very high compared to that of xenon, indicating that in pure bcc uranium, xenon moves much faster than molybdenum. The relatively low diffusivity of molybdenum also supports our assumption that molybdenum is randomly distributed in uranium–molybdenum alloys (presuming that the manufacturing process initially starts with a melt or powder that produces an ideal mixture). We also studied migration energies of xenon in the presence of molybdenum in U–Mo alloys. Different arrangements of molybdenum atoms in the nearest-neighbor shell and xenon’s distinct jumps are identified and their activation energies calculated. The binomial distribution suggests that having up to three molybdenum atoms in the nearest-neighbor shell is highly probable in U-10Mo and U-7Mo alloys. The presence of molybdenum in the nearest-neighbor shell of a xenon atom has an impact on the migration energy, but it does not generally increase or decrease the migration energy; both the locations of the molybdenum atoms and the direction of the jump influence the migration energy. Having one molybdenum atom in the nearest-neighbor shell increases the activation energy between 0.01 eV and 0.15 eV, depending on the location of the molybdenum atom relative to the

xenon atom and the vacancy. If xenon has two molybdenum atoms nearby, we found a similar increase, though there are combinations for which the migration energy is lower than it is in the single-molybdenum cases. For xenon with three nearby molybdenum atoms, the migration energy increases for all molybdenum/vacancy arrangements. While there are several molybdenum arrangements that result in decreased migration energies relative to some of the two-molybdenum configurations, the general trend with the addition of molybdenum in the nearest-neighbor shell near xenon is to increase the migration energy, hence reducing xenon mobility in U–Mo alloys.

We did not consider the influence of molybdenum in the second-nearest neighbor shell in bcc uranium. Future work should include a determination of the effective diffusion coefficient of xenon in U–Mo alloys using the kinetic Monte Carlo method.

References

1. J. L. Snelgrove, G. L. Hofman, M. K. Meyer, C. L. Trybus, and T. C. Wiencek, Nucl. Eng. Des. **178**, 119 (1997).
2. A. C. Lawson, C. E. Olsen, J. W. Richardson, M. H. Mueller, and G. H. Lander, Acta Crystallogr. B **44**, 89 (1988).
3. J. Akella, S. Weir, J. M. Wills, and P. Söderlind, J. Phys. Condens. Matter **9**, L549 (1997).
4. J. H. Kittel, B. R. T. Frost, J. P. Mustelier, K. Q. Bagley, G. C. Crittenden, and J. Van Dievoet, J. Nucl. Mater. **204**, 1 (1993).
5. A. S. Wilson and R. E. Rundle, Acta Crystallogr. **2**, 126 (1949).
6. V. P. Sinha, P. V. Hegde, G. J. Prasad, G. K. Dey, and H. S. Kamath, J. Alloy Compd. **506**, 253 (2010).
7. H. L. Yakel, J. Nucl. Mater. **33**, 286 (1969).
8. V. P. Sinha, P. V. Hegde, G. J. Prasad, G. K. Dey, and H. S. Kamath, J. Alloy Compd. **491**, 753 (2010).

9. N.-T. H. Kim-Ngan and L. Havela, *J. Sci. Adv. Mater. Dev.* **1**, 121 (2016).
10. H. Okamoto, M. E. Schlesinger, and E. M. Mueller, eds., Mo (molybdenum) binary alloy phase diagrams, in *Alloy Phase Diagrams*, ASM Handbook, Vol. 3 (ASM International, 2016) pp. 489–498.
11. A. Berche, N. Dupin, C. Guénau, C. Rado, B. Sundman, and J. C. Dumas, *J. Nucl. Mater.* **411**, 131 (2011).
12. R. Prabhakaran, *JOM* **69**, 2529 (2017).
13. M. K. Meyer, J. Gan, J. F. Jue, D. D. Keiser, E. Perez, A. Robinson, D. M. Wachs, N. Woolstenhulme, G. L. Hofman, and Y. S. Kim, *Nucl. Eng. Technol.* **46**, 169 (2014).
14. W. Williams, A. Robinson, and B. Rabin, *JOM* **69**, 2546 (2017).
15. A. E. Dwight, *J. Nucl. Mater.* **2**, 81 (1960).
16. K. Tangri and G. Williams, *J. Nucl. Mater.* **4**, 226 (1961).
17. A. Berche, N. Dupin, C. Guénau, C. Rado, B. Sundman, and J. C. Dumas, *J. Nucl. Mater.* **411**, 131 (2011).
18. X. Zhang, Y. F. Cui, G. L. Xu, W. J. Zhu, H. S. Liu, B. Y. Yin, and Z. P. Jin, *J. Nucl. Mater.* **402**, 15 (2010).
19. E. L. Losada and J. E. Garcés, *J. Nucl. Mater.* **518**, 380 (2019).
20. A. Landa, P. Söderlind, and P. E. A. Turchi, *J. Nucl. Mater.* **414**, 132 (2011).
21. P. R. Alonso and G. H. Rubiolo, *Model. Simulat. Mater. Sci. Eng.* **15**, 263 (2007).
22. A. Castellano, F. Bottin, B. Dorado, and J. Bouchet, *Phys. Rev. B* **101**, 184111 (2020).
23. V. V. Rondinella and T. Wiss, *Mater. Today* **13**, 24 (2010).
24. A. R. M. Iasir, N. J. Peters, and K. D. Hammond, *J. Nucl. Mater.* **508**, 159 (2018).
25. J. Rest, Y. S. Kim, G. L. Hofman, M. K. Meyer, and S. L. Hayes, *U-Mo Fuels Handbook. Version 1.0*, Tech. Rep. ANL-09/31 (Argonne National Lab. (ANL), Argonne, IL (United States), 2006).
26. R. W. Grimes and C. R. A. Catlow, *Phil. Trans. A Math. Phys. Eng. Sci.* **335**, 609 (1991).
27. D. A. Andersson, B. P. Überuaga, P. V. Nerikar, C. Unal, and C. R. Stanek, *Phys. Rev. B* **84**, 054105 (2011).

28. B. D. Miller, J. Gan, J. Madden, J.-F. Jue, A. Robinson, and D. D. Keiser, *J. Nucl. Mater.* **424**, 38 (2012).
29. B. D. Miller, J. Gan, D. D. Keiser, Jr, A. B. Robinson, J. F. Jue, J. W. Madden, and P. G. Medvedev, *J. Nucl. Mater.* **458**, 115 (2015).
30. J. Gan, D. D. Keiser, D. M. Wachs, A. B. Robinson, B. D. Miller, and T. R. Allen, *J. Nucl. Mater.* **396**, 234 (2010).
31. J. Gan, D. D. Keiser, B. D. Miller, A. B. Robinson, J.-F. Jue, P. Medvedev, and D. M. Wachs, *J. Nucl. Mater.* **424**, 43 (2012).
32. S. Van den Berghe, W. Van Renterghem, and A. Leenaers, *J. Nucl. Mater.* **375**, 340 (2008).
33. Y. Yun, H. Kim, H. Kim, and K. Park, *J. Nucl. Mater.* **378**, 40 (2008).
34. J. C. Carter, E. J. Driscoll, and T. S. Elleman, *Phys. Status Solidi A* **14**, 673 (1972).
35. H. Matzke, *Nucl. Appl.* **2**, 131 (1966).
36. J. R. MacEwan and W. H. Stevens, *J. Nucl. Mater.* **11**, 77 (1964).
37. K. Une, I. Tanabe, and M. Oguma, *J. Nucl. Mater.* **150**, 93 (1987).
38. C. R. A. Catlow, *Proc. Roy. Soc. Lond. Math. Phys. Sci.* **364**, 473 (1978).
39. R. A. Jackson, A. D. Murray, J. H. Harding, and C. R. A. Catlow, *Philos. Mag. A* **53**, 27 (1986).
40. R. W. Grimes, C. R. A. Catlow, and A. M. Stoneham, *J. Am. Ceram. Soc.* **72**, 1856 (1989).
41. R. G. J. Ball and R. W. Grimes, *J. Chem. Soc. Faraday Trans.* **86**, 1257 (1990).
42. T. Petit, G. Jomard, C. Lemaignan, B. Bigot, and A. Pasturel, *J. Nucl. Mater.* **275**, 119 (1999).
43. J.-P. Crocombette, *J. Nucl. Mater.* **305**, 29 (2002).
44. M. Freyss, N. Vergnet, and T. Petit, *J. Nucl. Mater.* **352**, 144 (2006).
45. G. Neumann and C. Tuijn, *Self-Diffusion and Impurity Diffusion in Pure Metals: Handbook of Experimental Data* (Elsevier, 2008) Chap. 10, pp. 333–348.
46. A. Paul and S. Divinski, *Handbook of Solid State Diffusion: Volume 2: Diffusion Analysis in Material Applications* (Elsevier, 2017) Chap. 8, pp. 339–372.
47. H. Matzke, Diffusion processes in nuclear fuels, in *Diffusion Processes in Nuclear Materials*, edited by R. P. Agarwala (North-Holland, 1992) pp. 9–69.

48. Y. Adda and A. Kirianenko, J. Nucl. Mater. **1**, 120 (1959).
49. N. L. Peterson and S. J. Rothman, Phys. Rev. **136**, A842 (1964).
50. S. J. Rothman, L. T. Lloyd, R. Weil, and A. L. Harkness, *Self-Diffusion in gamma Uranium*, Tech. Rep. ANL-5971 (Argonne National Lab., Lemont, Ill., 1959).
51. S. J. Rothman, J. Nucl. Mater. **3**, 77 (1961).
52. Y. Adda and A. Kirianenko, J. Nucl. Mater. **6**, 130 (1962).
53. R. Resnick and L. L. Seigle, J. Nucl. Mater. **5**, 5 (1962).
54. S. J. Rothman, J. Gray, Jr, J. P. Hughes, and A. L. Harkness, J. Nucl. Mater. **3**, 72 (1961).
55. Y. Liu, D. Yu, Y. Du, G. Sheng, Z. Long, J. Wang, and L. Zhang, Calphad **37**, 49 (2012).
56. D. E. Smirnova, A. Y. Kuksin, S. V. Starikov, and V. V. Stegailov, Phys. Met. Metallogr. **116**, 445 (2015).
57. J. B. Adams, S. M. Foiles, and W. G. Wolfer, J. Mater. Res. **4**, 102 (1989).
58. P. E. Blöchl, E. Smargiassi, R. Car, D. B. Laks, W. Andreoni, and S. T. Pantelides, Phys. Rev. Lett. **70**, 2435 (1993).
59. P. E. Blöchl, C. G. Van de Walle, and S. T. Pantelides, Phys. Rev. Lett. **64**, 1401 (1990).
60. W. Frank, U. Breier, C. Elsässer, and M. Fähnle, Phys. Rev. Lett. **77**, 518 (1996).
61. A. Janotti, M. Krčmar, C. L. Fu, and R. C. Reed, Phys. Rev. Lett. **92**, 085901 (2004).
62. M. Krčmar, C. L. Fu, A. Janotti, and R. C. Reed, Acta Mater. **53**, 2369 (2005).
63. V. Milman, M. C. Payne, V. Heine, R. J. Needs, J. S. Lin, and M. H. Lee, Phys. Rev. Lett. **70**, 2928 (1993).
64. N. Sandberg, B. Magyari-Köpe, and T. R. Mattsson, Phys. Rev. Lett. **89**, 065901 (2002).
65. A. B. Lidiard, Philos. Mag. Series 7 **46**, 1218 (1955).
66. A. B. Lidiard, Philos. Mag. A **5**, 1171 (1960).
67. A. D. Le Claire and A. B. Lidiard, Philos. Mag. A **1**, 518 (1956).
68. A. D. Le Claire, Philos. Mag. A **21**, 819 (1970).

69. H. Mehrer, *Diffusion in Solids: Fundamentals, Methods, Materials, Diffusion-Controlled Processes*, Vol. 155 (Springer Science & Business Media, 2007) pp. 116–122.
70. G. H. Vineyard and G. J. Dienes, Phys. Rev. **93**, 265 (1954).
71. G. H. Vineyard, J. Phys. Chem. Solid **3**, 121 (1957).
72. H. Eyring, J. Chem. Phys. **3**, 107 (1935).
73. M. G. Evans and M. Polanyi, Trans. Faraday Soc. **31**, 875 (1935).
74. K. Heinola and T. Ahlgren, J. Appl. Phys. **107**, 113531 (2010).
75. R. W. Balluffi and P. S. Ho, Diffusion (American Society for Metals, Metals Park, Ohio, 1973) p. 83.
76. C. Wolverton, Acta Mater. **55**, 5867 (2007).
77. P. Giannozzi, S. Baroni, N. Bonini, M. Calandra, R. Car, C. Cavazzoni, D. Ceresoli, G. L. Chiarotti, M. Cococcioni, I. Dabo, A. Dal Corso, S. de Gironcoli, S. Fabris, G. Fratesi, R. Gebauer, U. Gerstmann, C. Gouguassis, A. Kokalj, M. Lazzeri, L. Martin-Samos, N. Marzari, F. Mauri, R. Mazzarello, S. Paolini, A. Pasquarello, L. Paulatto, C. Sbraccia, S. Scandolo, G. Sclauzero, A. P. Seitsonen, A. Smogunov, P. Umari, and R. M. Wentzcovitch, J. Phys. Condens. Matter **21**, 395502 (2009), <http://www.quantum-espresso.org/>.
78. P. E. Blöchl, Phys. Rev. B **50**, 17953 (1994).
79. A. R. M. Iasir and K. D. Hammond, Comput. Mater. Sci. **171**, 109221 (2020).
80. QUANTUM ESPRESSO, PS library,
<http://www.quantum-espresso.org/pseudopotentials> (2019).
81. A. Dal Corso, Comput. Mater. Sci. **95**, 337 (2014).
82. J. P. Perdew, K. Burke, and M. Ernzerhof, Phys. Rev. Lett. **77**, 3865 (1996).
83. J. P. Perdew, K. Burke, and M. Ernzerhof, Phys. Rev. Lett. **78**, 1396 (1997).
84. P. Soderlind, Adv. Phys. **47**, 959 (1998).
85. Y.-Y. Ye, Y. Chen, K.-M. Ho, B. N. Harmon, and P.-A. Lindgård, Phys. Rev. Lett. **58**, 1769 (1987).
86. J. M. Sanchez and D. De Fontaine, Phys. Rev. Lett. **35**, 227 (1975).
87. B. Beeler, B. Good, S. Rashkeev, C. Deo, M. Baskes, and M. Okuniewski, J. Phys. Condens. Matter **22**, 505703 (2010).
88. H. J. Monkhorst and J. D. Pack, Phys. Rev. B **13**, 5188 (1976).

89. G. Henkelman, B. P. Uberuaga, and H. Jónsson, *J. Chem. Phys.* **113**, 9901 (2000).
90. G. Henkelman and H. Jónsson, *J. Chem. Phys.* **113**, 9978 (2000).
91. S. Xiang, H. Huang, and L. Hsiung, *J. Nucl. Mater.* **375**, 113 (2008).
92. H. Matter, J. Winter, and W. Triftshäuser, *J. Nucl. Mater.* **88**, 273 (1980).
93. K. R. Lund, K. G. Lynn, M. H. Weber, and M. A. Okuniewski, *J. Phys. Conf. Ser.* **443**, 012021 (2013).
94. P. Olsson, T. P. C. Klaver, and C. Domain, *Phys. Rev. B* **81**, 054102 (2010).
95. T. Ohnuma, N. Soneda, and M. Iwasawa, *Acta Mater.* **57**, 5947 (2009).
96. E. Vincent, C. Becquart, and C. Domain, *Nucl. Instrum. Meth. Phys. Res. B* **228**, 137 (2005).
97. X.-S. Kong, X. Wu, Y.-W. You, C. Liu, Q. Fang, J.-L. Chen, G.-N. Luo, and Z. Wang, *Acta Mater.* **66**, 172 (2014).
98. J. Burke, *Journal of the Less-Common Metals* **28**, 441 (1972).

CHAPTER 6

HELIUM IMPURITIES AND INTERACTION WITH LITHIUM

This chapter has been submitted as journal article for peer review. The authors are A. Rafi M. Iasir and Karl D. Hammond of the University of Missouri.

6.1 Introduction

Lithium is potentially an important element in the context of magnetic fusion devices. Lithium-coated surfaces have been tested in several fusion devices around the world [1–6] and have been found to increase plasma confinement and improve plasma edge conditions [7]. This behavior is due in part to lithium’s ability to trap hydrogen isotopes [8], which has the net result of decreasing fuel recycling at the plasma edge, leading to higher confinement and fewer disruptions [7]. Lithium has also been proposed as a tritium-breeding material in fusion reactors [9] and as a liquid wall-coating “armor” to protect plasma-facing components [10]. In the near-surface region of plasma-facing materials, high densities of interstitials and vacancies are produced and high concentrations of hydrogen and helium are present. These defects and impurities will change the microstructure of the material [11]. It is therefore important to determine the energies of defects in lithium and their interactions with helium. This study calculates the energies of several point defects in lithium as well as the formation, binding, and migration energies of helium atoms and clusters trapped in lithium.

6.2 Methodology

We performed all of our calculations using density functional theory (DFT) with plane-wave basis sets as implemented in the software QUANTUMESPRESSO [12]. Projector augmented wave (PAW) [13] pseudopotentials from QUANTUMESPRESSO's PS library [14, 15] were used. The density functional of Perdew, Burke, and Ernzerhof (PBE) was used as the exchange–correlation functional [16, 17]. We used a $4 \times 4 \times 4$ supercell of bcc lithium, which consists of 128 atoms, to simulate defects. Brillouin zone sampling was performed using the scheme of Monkhorst and Pack [18] with a k -point mesh of $5 \times 5 \times 5$. The plane wave cutoff energy was 50 Ry. The equilibrium lattice parameter obtained was 3.436 Å for bcc lithium. All defect calculations were performed by fully relaxing the atomic positions in the supercell at constant volume using this lattice parameter. The migration energies were calculated using the nudged elastic band method [19–21] with seven images along the migration pathway.

The formation energies are calculated as follows:

$$E_f^{\text{oct}} = E_{\text{Li+He}_{\text{oct}}} - E_{\text{Li}_N} - E_{\text{He}_{\text{isolated}}} \quad (6.1\text{a})$$

$$E_f^{\text{tetr}} = E_{\text{Li+He}_{\text{tetr}}} - E_{\text{Li}_N} - E_{\text{He}_{\text{isolated}}} \quad (6.1\text{b})$$

$$E_f^{\square} = E_{\text{Li}_{N-1}} - \frac{N-1}{N} E_{\text{Li}_N} \quad (6.1\text{c})$$

$$E_f^{\text{subs}} = E_{\text{Li+He}_{\square}} - \frac{N-1}{N} E_{\text{Li}_N} - E_{\text{He}_{\text{isolated}}}. \quad (6.1\text{d})$$

Here, $E_{\text{Li+He}_{\text{tetr/oct}}}$ is the energy of a system in which helium is situated at either octahedral or tetrahedral sites in bcc lithium. $E_{\text{Li+He}_{\square}}$ is the energy of a system in which helium is in a substitutional position, E_{Li_N} is the energy of a defect-free lithium supercell containing N atoms, and $E_{\text{He}_{\text{isolated}}}$ is the energy of an isolated helium atom. $E_{\text{Li}_{N-1}}$ is the energy of a lithium bcc supercell with a lithium self-vacancy present.

The formation energy of a self-interstitial atom (SIA) is calculated using

$$E_f^{\text{SIA}} = E_{\text{Li}_{N+1}} - \frac{N+1}{N} E_{\text{Li}_N}, \quad (6.2)$$

where $E_{\text{Li}_{N+1}}$ is the energy of a system with a lithium self-interstitial atom starting in either an octahedral or tetrahedral position. The binding energy of two helium atoms is determined via the formula

$$E_b^{\text{He}_1-\text{He}_2} = E_{\text{Li}_N+\text{He}_1} + E_{\text{Li}_N+\text{He}_2} - E_{\text{Li}_N+\text{He}_1+\text{He}_2} - E_{\text{Li}_N}. \quad (6.3)$$

Here, $E_{\text{Li}+\text{He}_1}$ is the energy of the supercell with a single helium interstitial present, and $E_{\text{Li}_N+\text{He}_1+\text{He}_2}$ is the energy of the supercell containing two nearby helium atoms in interstitial positions. For more than two helium atoms, the following equation is used to calculate the binding energies between them:

$$E_b^{\text{He}_n} = \left(\sum_{i=1}^n E_{\text{Li}_N+\text{He}_i} \right) - [E_{\text{Li}_N+\text{He}_n} + (n-1)E_{\text{Li}_N}]. \quad (6.4)$$

The helium–helium dumbbell formation energy (two helium atoms sharing a vacancy) can be calculated using the following equation:

$$E_f^{\text{He}-\square-\text{He}} = E_{\text{Li}_{N-1}+\text{He}-\square-\text{He}} - \frac{N-1}{N} E_{\text{Li}_N} - E_{\text{He}_{\text{isolated}}}. \quad (6.5)$$

Here, $E_{\text{Li}_{N-1}+\text{He}-\square-\text{He}}$ is the energy of a supercell containing the helium dumbbell.

6.3 Results and Discussion

We calculated the formation energies for different configurations of the self-interstitial atoms and the vacancy formation energy for lithium. The results are presented in Table 6.1. Our results are comparable with previous DFT calculations

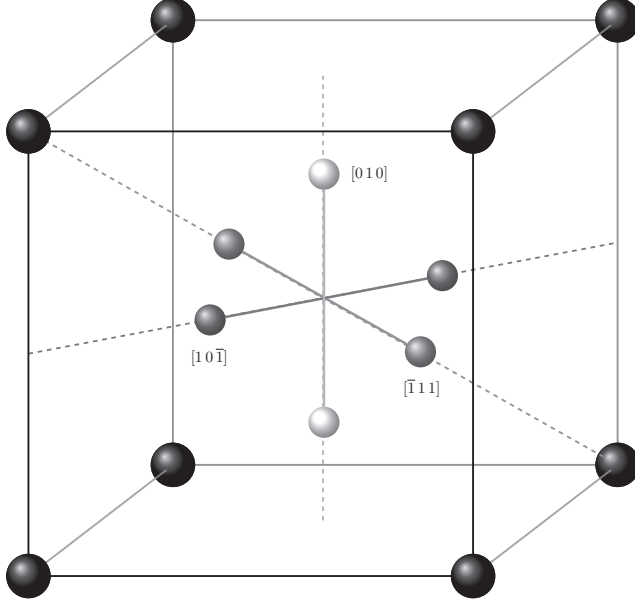


Figure 6.1. Helium–helium dumbbells in different orientations in the bcc lithium unit cell.

and with experiments. Earlier DFT studies produced formation energies of lithium self-vacancies from 0.52 to 0.57 eV [22–25], compared to our value of 0.496 eV. The discrepancy could come from the size of the supercell, elastic interaction, the density functional, and the quality of the pseudopotential.

We also calculated the self-interstitial formation energy of lithium. Octahedral self-interstitials are unstable and relax to a dumbbell oriented in one of the $\langle 100 \rangle$ directions (Fig. 6.1). Tetrahedral self-interstitials are also unstable and relax to $\langle 110 \rangle$ dumbbells. The lowest-energy dumbbell orientations are the $\langle 111 \rangle$ orientations, which is a similar trend as in other non-ferromagnetic bcc materials. The vacancy formation energy is slightly lower than Frank *et al.*'s value (0.52 eV) [25] and Ma and Dudarev's value (0.506 eV) [26], while the migration energy of the vacancy in $\langle 111 \rangle$ directions is slightly higher than that found by Ma and Dudarev [26]. The self-interstitial dumbbell formation energy is comparable to the values reported by Ma and Dudarev [27].

Table 6.1. Calculated vacancy formation energy E_f^\square , vacancy migration energy E_m^\square , and various split-dumbbell and self-interstitial formation energies in lithium. Results are compared with previous theoretical and experimental results (experiments in italics).

Defect	Energy (eV)	Previous Work
vacancy (E_f^\square)	0.496	0.506 [26]
		0.52 [25]
		0.508 [28]
vacancy (E_m^\square)	0.086	0.053 [26]
		0.038 [28]
$\langle 111 \rangle$ dumbbell (E_f)	0.589	0.573 [27]
$\langle 110 \rangle$ dumbbell (E_f)	0.646	0.637 [27]
$\langle 100 \rangle$ dumbbell (E_f)	0.791	0.782 [27]
tetrahedral ($E_f^{\text{tetr}}\text{a}$)	0.646	0.696 [27]
octahedral ($E_f^{\text{oct}}\text{b}$)	0.793	0.785 [27]

^a equivalent to $\langle 110 \rangle$ dumbbell formation

^b equivalent to $\langle 100 \rangle$ dumbbell formation

We now turn our attention to helium interactions with lithium. During the operation of a plasma device in which lithium is present, any lithium-coated surfaces will interact with high fluxes of helium and hydrogen isotopes. There will also be (n,α) reactions that transmute lithium to hydrogen and helium. These processes will build up a substantial amount of hydrogen and helium inside the plasma-facing material. Significant research has been and is still being performed to understand the behavior of helium in metals [11, 31, 32].

One of the major challenges is the low solubility of helium in metals. Helium atoms in a metal may find low-energy positions either in substitutional or interstitial lattice sites. We calculated the formation energies of different configurations of helium in substitutional as well as interstitial positions in lithium. The results are presented in Table 6.2. We compare our results to similar configurations in tungsten and iron, two common bcc metals used in plasma devices. Our calculations predict

Table 6.2. Formation energies (E_f), binding energies (E_b), and migration energies (E_m , all in eV) for helium located at octahedral or tetrahedral interstitial sites as well as substitutional sites. The results are compared with helium interactions with tungsten and iron, which are both bcc metals at standard temperature and pressure.

Quantity	Li–He	W–He [29]	Fe–He [30]
E_f^{oct}	1.142	6.38	4.60
E_f^{tetr}	1.132	6.16	4.37
E_f^{subs}	1.213	4.70	4.08
$E_m^{\text{T-T}}$	0.003	0.06	0.06
$E_m^{\text{T-O-T}}$	0.013		
$E_m^{\text{O-O}}$	0.004		
$E_b^{\text{He-He}}\text{a}$	0.209	1.03	
$E_b^{\text{He}_s-\square}\text{b}$	0.211		
$E_b^{\text{He}_t-\square}\text{c}$	0.421		

^aboth helium at nearest tetrahedral positions

^bone helium at a substitutional position interacting with a vacancy

^cone helium at a tetrahedral position interacting with a vacancy

Table 6.3. Formation energies (E_f) of He–He split dumbbells bound to a vacancy.

Orientation	E_f (eV)
$\langle 111 \rangle$	1.844
$\langle 110 \rangle$	1.863
$\langle 100 \rangle$	1.879

that the tetrahedral interstitial position is the lowest-energy interstitial site for helium, which is also the case for other bcc metals such as tungsten and iron [29, 33]. However, the difference between the octahedral and tetrahedral interstitial formation energies is only 0.01 eV. This is very low compared to tungsten–helium (0.22 eV [29]) and iron–helium (0.23 eV [30]).

The formation energy of helium in a substitutional position in lithium is 1.213 eV, which is higher than both the tetrahedral and the octahedral interstitial formation energies (which are 1.132 eV and 1.142 eV, respectively). This is an atypical result compared to helium in other bcc metals or in fcc metals, for which the substitutional site has a significantly lower formation energy than the two interstitial sites [29, 30, 34, 35], and is more consistent with the energetics of helium in hexagonal close-packed (hcp) metals [36, 37]. We reproduced this result using a different DFT package (*i.e.*, ABINIT [38, 39]) and got the same values. We also got similar values using ultrasoft pseudopotentials in QUANTUMESPRESSO. This is an intriguing result, and will have implications for future simulations of helium in lithium.

Next, we calculated the binding energy of helium to a vacancy. The substitutional formation energy is higher than the two interstitial formation energies, though the substitutional site is still the energetic minimum in the presence of a vacancy. The binding energy of helium in a substitutional position to a vacancy is 0.21 eV. The binding energy of helium at a tetrahedral interstitial site to a vacancy is 0.42 eV. The binding energy between two helium atoms at nearby interstitial sites is 0.209 eV, which is lower than that in the tungsten–helium system (1.03 eV [29]). The binding energy of multiple helium atoms to a vacancy is also calculated, and the result is shown in Fig. 6.3. There is a nearly linear increase in the binding energy as the number of helium atoms increases, which indicates that a group of helium atoms will tend to aggregate onto a vacancy and that helium bubble self-nucleation will likely occur in lithium, as it does in other bcc metals [40].

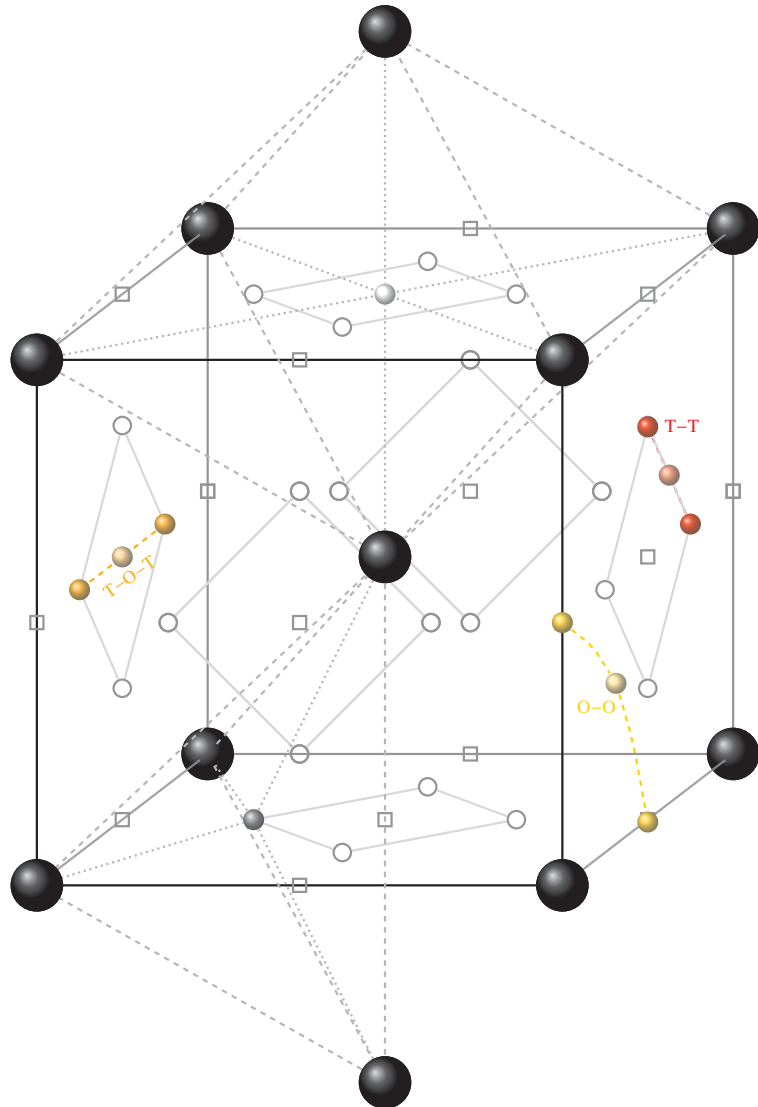


Figure 6.2. Tetrahedral (\circ) and octahedral (\square) sites in a bcc crystal. Three different transition states—tetrahedral to tetrahedral (T–T), octahedral to octahedral (O–O) and tetrahedral to octahedral to tetrahedral (T–O–T)—are shown.

Table 6.4. Binding energy of n helium atoms to a vacancy.

n	E_b
1	0.415
2	0.898
3	1.249
4	1.903
5	2.194
6	3.062
7	3.216
8	3.925

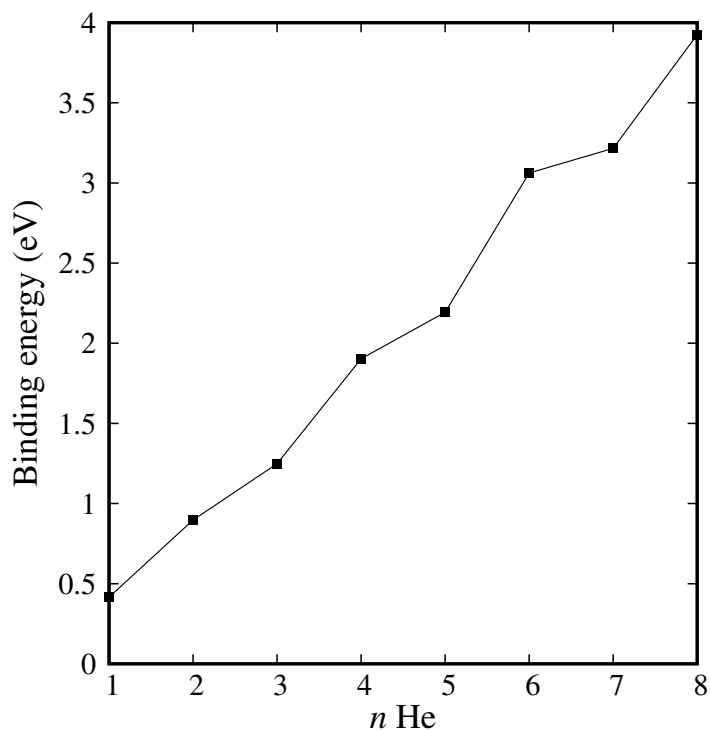


Figure 6.3. Binding energy of n helium atoms to a vacancy for $n \in [1, 8]$.

Two helium atoms around a vacancy form a split dumbbell, much like lithium self-interstitials do. The formation energy varies based on the orientation of the dumbbell. The helium dumbbell formation energies are presented in Table 6.3. The lowest-energy dumbbells have $\langle 1\ 1\ 1 \rangle$ orientations (Fig. 6.1).

The migration energies of helium from one tetrahedral site to a nearby tetrahedral site (Fig. 6.2) were calculated using the nudged elastic band method [19–21]. The migration energy from one tetrahedral site to an adjacent tetrahedral site (Fig. 6.2) is only 0.003 eV, indicating that helium interstitials will be very mobile in lithium. Helium has a higher migration energy (E_m^{T-T}) in tungsten (0.06 eV [29]) and iron (0.06 eV [33]). The migration energy from one octahedral site to the next octahedral site (E_m^{O-O}) without passing through a tetrahedral site in lithium is 0.004 eV, which is also very low. The low migration energies indicate that helium would be highly mobile in bulk lithium, much more so than in other bcc metals. It also indicates that bulk helium diffusion in lithium would be more akin to diffusion in gases or liquids, with a $T^{3/2}$ dependence of the diffusion coefficient arising from translational motion, but without the Arrhenius temperature dependence associated with vibrational motion. This result, combined with the higher formation energy of substitutional helium compared to interstitial helium, suggests that helium transport in lithium will be fundamentally different than it is in iron, nickel, tungsten, and other metals.

References

1. M. G. Bell, H. W. Kugel, R. Kaita, L. E. Zakharov, H. Schneider, B. P. LeBlanc, D. Mansfield, R. E. Bell, R. Maingi, S. Ding, S. M. Kaye, S. F. Paul, S. P. Gerhardt, J. M. Canik, J. C. Hosea, G. Taylor, and the NSTX Research Team, *Plasma Phys. Contr. Fusion* **51**, 124054 (2009).
2. S. V. Mirnov, V. B. Lazarev, S. M. Sotnikov, T-11M Team, V. A. Evtikhin, I. E. Lyublinski, and A. V. Vertkov, *Fusion Eng. Des.* **65**, 455 (2003).
3. J. Sánchez, F. L. Tabarés, D. Tafalla, J. A. Ferreira, I. García-Cortés, C. Hidalgo, F. Medina, M. A. Ochando, M. A. Pedrosa, and The TJ-II Team, *J. Nucl. Mater.* **390**, 852 (2009).
4. A. Tuccillo, A. Alekseyev, B. Angelini, S. Annibaldi, M. Apicella, G. Apruzzese, J. Berrino, E. Barbato, A. Bertocchi, A. Biancalani, W. Bin, A. Botrugno, G. Bracco, S. Briguglio, A. Bruschi, P. Buratti, G. Calabro, A. Cardinali, C. Castaldo, C. Centoli, R. Cesario, L. Chen, S. Cirant, V. Cociollo, F. Crisanti, R. D. Angelis, U. de Angelis, L. D. Matteo, C. D. Troia, B. Esposito, G. Fogaccia, D. Frigione, L. Gabellieri, F. Gandini, E. Giovannozzi, G. Granucci, F. Gravanti, G. Grossetti, G. Grossi, F. Iannone, H. Kroegler, V. Lazarev, E. Lazzaro, I. Lyublinski, G. Maddaluno, M. Marinucci, D. Marocco, J. Martin-Solis, G. Mazzitelli, C. Mazzotta, V. Mellera, F. Mirizzi, S. Mirnov, G. Monari, A. Moro, V. Muzzini, S. Nowak, F. Orsitto, L. Panaccione, D. Pacella, M. Panella, F. Pegoraro, V. Pericoli-Ridolfini, S. Podda, S. Ratynskaia, G. Ravera, A. Romano, A. Rufoloni, A. Simonetto, P. Smeulders, C. Sozzi, E. Sternini, B. Tilia, O. Tudisco, A. Vertkov, V. Vitale, G. Vlad, R. Zagórski, M. Zerbini, and F. Zonca, *Nucl. Fusion* **49**, 104013 (2009).
5. G. Xu, B. Wan, J. Li, X. Gong, J. Hu, J. Shan, H. Li, D. Mansfield, D. Humphreys, V. Naulin, and East team and international collaborators, *Nucl. Fusion* **51**, 072001 (2011).
6. S. Munaretto, S. D. Bello, P. Innocente, M. Agostini, F. Auriemma, S. Barison, A. Canton, L. Carraro, G. D. Masi, S. Fiameni, P. Scarin, and D. Terranova, *Nucl. Fusion* **52**, 023012 (2012).
7. J. P. Allain and C. N. Taylor, *Phys. Plasma* **19**, 056126 (2012).
8. S. Erents, G. McCracken, and P. Goldsmith, *J. Phys. D Appl. Phys.* **4**, 672 (1971).
9. J. Hartley, B. Gore, and J. Young, *Lithium Needs and Resources* , 337 (1978).
10. C. E. Kessel, D. Andruczyk, J. P. Blanchard, T. Bohm, A. Davis, K. Hollis, P. W. Humrickhouse, M. Hvasta, M. Jaworski, J. Jun, Y. Katoh, A. Khodak, J. Klein, E. Kolemen, G. Larsen, R. Majeski, B. J. Merrill, N. B. Morley, G. H. Neilson, B. Pint, M. E. Rensink, T. D. Rognlien, A. F. Rowcliffe, S. Smolentsev, M. S.

- Tillack, L. M. Waganer, G. M. Wallace, P. Wilson, and S.-J. Yoon, *Fusion Sci. Technol.* **75**, 886 (2019).
11. K. D. Hammond, *Mater. Res. Express* **4**, 104002 (2017).
 12. P. Giannozzi, S. Baroni, N. Bonini, M. Calandra, R. Car, C. Cavazzoni, D. Ceresoli, G. L. Chiarotti, M. Cococcioni, I. Dabo, A. Dal Corso, S. de Gironcoli, S. Fabris, G. Fratesi, R. Gebauer, U. Gerstmann, C. Gougaud, A. Kokalj, M. Lazzeri, L. Martin-Samos, N. Marzari, F. Mauri, R. Mazzarello, S. Paolini, A. Pasquarello, L. Paulatto, C. Sbraccia, S. Scandolo, G. Sclauzero, A. P. Seitsonen, A. Smogunov, P. Umari, and R. M. Wentzcovitch, *J. Phys. Condens. Matter* **21**, 395502 (2009), <http://www.quantum-espresso.org/>.
 13. P. E. Blöchl, *Phys. Rev. B* **50**, 17953 (1994).
 14. A. Dal Corso, *Comput. Mater. Sci.* **95**, 337 (2014).
 15. QUANTUM ESPRESSO, PS library,
<http://www.quantum-espresso.org/pseudopotentials> (2019).
 16. J. P. Perdew, K. Burke, and M. Ernzerhof, *Phys. Rev. Lett.* **77**, 3865 (1996).
 17. J. P. Perdew, K. Burke, and M. Ernzerhof, *Phys. Rev. Lett.* **78**, 1396 (1997).
 18. H. J. Monkhorst and J. D. Pack, *Phys. Rev. B* **13**, 5188 (1976).
 19. H. Jónsson, G. Mills, and K. W. Jacobsen, in *Classical and Quantum Dynamics in Condensed Phase Simulations*, edited by B. J. Berne, G. Ciccotti, and D. F. Coker (World Scientific, Singapore, 1998) Chap. 16, pp. 385–405.
 20. G. Henkelman, B. P. Uberuaga, and H. Jónsson, *J. Chem. Phys.* **113**, 9901 (2000).
 21. G. Henkelman and H. Jónsson, *J. Chem. Phys.* **113**, 9978 (2000).
 22. R. Benedek, L. Yang, C. Woodward, and B. Min, *Phys. Rev. B* **45**, 2607 (1992).
 23. R. Pawellek, M. Fahnle, C. Elsasser, K. M. Ho, and C. T. Chan, *J. Phys. Condens. Matter* **3**, 2451 (1991).
 24. W. Frank, U. Breier, C. Elsässer, and M. Fähnle, *Phys. Rev. B* **48**, 7676 (1993).
 25. W. Frank, U. Breier, C. Elsässer, and M. Fähnle, *Phys. Rev. Lett.* **77**, 518 (1996).
 26. P. Ma and S. Dudarev, *Phys. Rev. Mater.* **3**, 063601 (2019).
 27. P. Ma and S. L. Dudarev, *Phys. Rev. Mater.* **3**, 013605 (2019).
 28. P. Ehrnhar, P. Jung, H. Schultz, and H. Ullmaier, in *Atomic Defects in Metals*, Vol. 25, edited by H. Ullmaier (Springer-Verlag Berlin Heidelberg, 1991).
 29. C. S. Becquart and C. Domain, *Phys. Rev. Lett.* **97**, 196402 (2006).

30. T. Seletskaia, Y. Ossetsky, R. E. Stoller, and G. M. Stocks, Phys. Rev. Lett. **94**, 046403 (2005).
31. K. D. Hammond, D. Maroudas, and B. D. Wirth, Sci. Rep. **10**, 2192 (2020).
32. M. Samaras, Mater. Today **12**, 46 (2009).
33. C. Fu and F. Willaime, Phys. Rev. B **72**, 064117 (2005).
34. T. Seletskaia, Y. Ossetsky, R. E. Stoller, and G. M. Stocks, Phys. Rev. B **78**, 134103 (2008).
35. L.-X. Liao, X. Zhang, C.-L. Ren, Z.-D. Zhang, H.-F. Huang, G.-H. Ma, and P. Huai, J. Appl. Phys. **127**, 175903 (2020).
36. L. Yang, R. Chen, S. Peng, X. Long, Z. Wu, F. Gao, and X. Zu, Sci. China Phys. Mech. Astron. **54**, 827 (2011).
37. L. Yang, S. M. Peng, X. G. Long, F. Gao, H. L. Heinisch, R. J. Kurtz, and X. T. Zu, J. Phys. Condens. Matter **23**, 035701 (2011).
38. X. Gonze, B. Amadon, G. Antonius, F. Arnardi, L. Baguet, J.-M. Beuken, J. Bieder, F. Bottin, J. Bouchet, E. Bousquet, N. Brouwer, F. Bruneval, G. Brunin, T. Cavignac, J.-B. Charraud, W. Chen, M. Côté, S. Cottenier, J. Denier, G. Geneste, P. Ghosez, M. Giantomassi, Y. Gillet, O. Gingras, D. R. Hamann, G. Hautier, X. He, N. Helbig, N. Holzwarth, Y. Jia, F. Jollet, W. Lafargue-Dit-Hauret, K. Lejaeghere, M. A. Marques, A. Martin, C. Martins, H. P. Miranda, F. Naccarato, K. Persson, G. Petretto, V. Planes, Y. Pouillon, S. Prokhorenko, F. Ricci, G.-M. Rignanese, A. H. Romero, M. M. Schmitt, M. Torrent, M. J. van Setten, B. Van Troeye, M. J. Verstraete, G. Zérah, and J. W. Zwanziger, Comput. Phys. Commun. **248**, 107042 (2020).
39. A. H. Romero, D. C. Allan, B. Amadon, G. Antonius, T. Applencourt, L. Baguet, J. Bieder, F. Bottin, J. Bouchet, E. Bousquet, F. Bruneval, G. Brunin, D. Caliste, M. Côté, J. Denier, C. Dreyer, P. Ghosez, M. Giantomassi, Y. Gillet, O. Gingras, D. R. Hamann, G. Hautier, F. Jollet, G. Jomard, A. Martin, H. P. C. Miranda, F. Naccarato, G. Petretto, N. A. Pike, V. Planes, S. Prokhorenko, T. Rangel, F. Ricci, G.-M. Rignanese, M. Royo, M. Stengel, M. Torrent, M. J. van Setten, B. V. Troeye, M. J. Verstraete, J. Wiktor, J. W. Zwanziger, and X. Gonze, J. Chem. Phys. **152**, 124102 (2020).
40. F. Sefta, K. D. Hammond, N. Juslin, and B. D. Wirth, Nucl. Fusion **53**, 073015 (2013).

CHAPTER 7

CONCLUSIONS AND FUTURE WORK

We have studied the impact of fission gas on U–Mo alloys. Xenon and krypton gas bubbles inside the fuel have a significant impact on the thermal conductivities of the fuel. In comparison to pure xenon bubbles in U-10Mo, a xenon–krypton mixture makes very little differences in terms of thermal conductivity. This reaffirms that xenon contributes the most to the thermal conductivity. Both intra- and inter-granular xenon bubbles impact the heat transfer. The arrangements of the bubbles also influence the heat transfer.

Since xenon forms a gas-bubble superlattice in U–Mo alloys, we can estimate the reduction of the thermal conductivity within reasonable precision. Grain boundaries also play an important role in the collection of fission gas. The growth of grain boundaries in U-10Mo should be studied. The current model can be adjusted to accommodate the expansion of grain boundaries. It is important to mention that, all of our studies here used a two-dimensional (2D) model. Mathematical models of thermal conductivity in 2D underestimate the three dimensional thermal conductivities. However, because of the complexities of studying the grain boundaries in three dimensions, one can get the general idea using a simpler 2D model as was done here. The growth of grain boundaries and recrystallization may change the grain structure.

Solid fission products play important roles in metallic fuel. The influence of intermetallic compounds has already been observed in the case of dispersion U–

Mo fuel. We have not included solid fission products in our thermal conductivity model for U–Mo fuel, but this could be a possible improvement. They can influence both the swelling and transport processes inside the fuel. In monolithic fuel, there are two layers of cladding around the fuel meat. One is aluminum and other one is zirconium. These two layers will have significant impact on the heat transfer and should be studied extensively. A proper thermal conductivity model with contact pressure analysis would also improve the one discussed in Ch. 3.

We also introduced a new pseudopotential for density functional theory studies of uranium. The electronic properties of the three phases of metallic uranium were calculated and compared with previous results. The new pseudopotential shows that α -uranium has the lowest energy in the ground state. The elastic moduli for α - and γ -uranium were also calculated and compared. We used this model to study supercells of γ -uranium and uranium–molybdenum alloys. The vacancy formation energy agrees well with both experiment and previous theoretical studies.

Xenon forms inside the fuel matrix as a fission product. Because of its size, it uses vacancies to diffuse inside the matrix. We calculated the xenon migration energy from the lattice site to the nearest vacancy in both γ -uranium and uranium–molybdenum alloys. In pure γ -uranium, the migration energy is about 0.161 eV, which is lower than the molybdenum migration energy of 2.067 eV. This higher migration energy of molybdenum indicates that in γ -uranium, molybdenum atoms move very slowly. Xenon moves significantly faster. In the presence of a vacancy, xenon tends to find its minimum-energy position in between the lattice site and the vacancy.

Uranium–molybdenum alloys are disordered (*i.e.*, non-stoichiometric). This makes *ab initio* study of uranium–molybdenum alloys challenging. To study xenon diffusion inside uranium–molybdenum fuel, we systematically included molybdenum in nearest-neighbor locations of a bcc lattice. We did not include the effects

of molybdenum in the second-nearest-neighbor shell, which could be a potential future study to see how the second shell impacts the migration energy of xenon. According to our calculations, the migration energy of xenon increases when a single molybdenum atom is present in a first-nearest-neighbor location. As the number of molybdenum atoms increases, the value of migration energy may also increase, depending on the direction of the migration and the presence of molybdenum at sites near the pathway. The overall trend is an increase of the migration energy with molybdenum content. To estimate the diffusion coefficient of xenon in uranium-molybdenum, a kinetic Monte Carlo simulation can be used that incorporates these different migration pathways.

Finally, we discussed the defect properties of lithium and its interactions with helium. Lithium, a potential plasma-facing material, is the first metal in the periodic table. The vacancy formation and migration energies are calculated and compared with previous theoretical work. The formation energies of helium in interstitial positions are calculated. The lowest-energy position is the tetrahedral position in bcc lithium. Our calculation predicts that the formation energy of helium in a substitutional position is higher than that of tetrahedral and octahedral interstitial locations.

The binding energies of helium to vacancies are also calculated. The binding energies of helium in tetrahedral locations and nearby vacancies are higher than the binding energy of helium to a lattice (substitutional) site. Multiple helium atoms bound to a vacancy have higher and higher binding energies as the number of helium increases. Because of the size of helium relative to lithium and the larger lattice parameter of lithium, helium can migrate from one interstitial site to another without a relatively high barrier. The lowest migration energy is 0.003 eV for the migration from a tetrahedral site to another tetrahedral site. Future work should study helium mobility through complex grain boundaries and surfaces in lithium.

Molecular dynamics methods can be used to study grain boundaries. A robust pair potential for lithium–helium system is required, and needs to be developed. The DFT results in the current work can be used to fit a pair potential.

APPENDIX A

ATOMIC UNITS

There are special units of measurement which is convenient for atomic physics and DFT calculations. They are named after the physicist Douglas Hartree [1]. In this system of units, the numerical values of the four fundamental physical constants are assumed to be unity. They are as follows:

- Reduced Planck constant: $\hbar = 1$, the atomic unit of angular momentum.
- Elementary charge: $e = 1$, the atomic unit of charge.
- Bohr radius: $a_0 = 1$, atomic unit of length.
- Electronic mass: $m_e = 1$, the atomic unit of mass.

Now we will explore how atomic units simplify quantum mechanical equations for the hydrogen atom. The hydrogen atom consists of a heavy proton (charge e) with a much lighter electron (charge $-e$) that orbits around it. The potential energy (in SI units) is

$$V(\mathbf{r}) = -\frac{Ze^2}{4\pi\epsilon_0 r} \quad (\text{A.1})$$

where Z is the atomic number and r is the position relative to the nuclear site. The radial Schrödinger equation including the centrifugal term is:

$$\left[-\frac{\hbar^2}{2m_e} \nabla_r^2 + \frac{\hbar^2 \ell(\ell+1)}{2m_e r^2} - \frac{Ze^2}{4\pi\epsilon_0 r} - E \right] r R(r) = 0 \quad (\text{A.2})$$

This equation can be simplified by introducing dimensionless quantities. Multiplying Eq. (A.2) by m_e/\hbar^2 the equation becomes

$$\begin{aligned} \left[-\nabla_r^2 + \frac{\ell(\ell+1)}{r^2} + \frac{2m_e Ze^2}{4\pi\epsilon_0\hbar^2} \frac{1}{r} - \frac{2m_e E}{\hbar^2} \right] rR(r) &= 0 \\ \left[-\frac{1}{2}\nabla_r^2 + \frac{\ell(\ell+1)}{2r^2} + \frac{Z}{a_0 r} - \frac{E}{E_0 a_0^2} \right] rR(r) &= 0 \\ \left[-\frac{1}{2}\nabla_\zeta^2 + \frac{\ell(\ell+1)}{2\zeta^2} + \frac{Z}{\zeta} - \frac{E}{E_0} \right] \zeta R(\zeta a_0) &= 0 \end{aligned} \quad (\text{A.3})$$

The above equation has two units: one is a length scale, the Bohr radius a_0 and the other is an energy scale, the hartree E_0 .

A.1 Bohr Radius

$$a_0 = \frac{4\pi\epsilon_0\hbar^2}{m_e e^2} \quad (\text{A.4})$$

The Bohr radius is the length unit of the hartree atomic unit system. It corresponds to the radius of a classical electron circling a proton at the ground state energy of the hydrogen atom. Using all the fundamental constants in Eq. (A.4) the standard atomic unit of length is

$$1 \text{ bohr} = \frac{4\pi\epsilon_0\hbar^2}{m_e e^2} = 0.529\,177\,25 \times 10^{-10} \text{ m} = 0.52917725 \text{ \AA} \quad (\text{A.5})$$

A.2 Hartree

$$E_0 = \frac{\hbar^2}{m_e a_0^2} = \frac{m_e e^4}{(4\pi\epsilon_0\hbar)^2} \quad (\text{A.6})$$

The Hartree is the energy unit in the Hartree atomic unit system. One Hartree is twice the binding energy of an electron in the hydrogen atom. To satisfy $a_0 = 1$, the fundamental constants are defined to be unity ($\hbar = m_e = e = 4\pi\epsilon_0 = 1$), according

to Eq. (A.4). The unit of Hartree can also be calculated from the fundamental constants:

$$1 \text{ hartree} = \frac{\hbar^2}{m_e a_0^2} = \frac{m_e e^4}{(4\pi\epsilon_0\hbar)^2} = 4.359\,748\,2 \times 10^{-10} \text{ J} = 27.211396 \text{ eV} \quad (\text{A.7})$$

In Hartree units, the Schrödinger equation of an electron in the Coulomb potential of the nucleus has the following form:

$$\left(-\frac{1}{2}\nabla^2 - \frac{Z}{r} - E \right) |\psi\rangle = 0 \quad (\text{A.8})$$

A.3 Rydberg Units

The Rydberg is another useful atomic unit which is widely used in DFT and atomic physics. In Hartree atomic units, the assumption is $\hbar^2/2m_e = \frac{1}{2}$. In Rydberg atomic units the equivalent assumption is:

$$\hbar = 2m_e = e^2/2 = 1$$

Using the above relations, the length unit does not change:

$$a_0 = \frac{4\pi\epsilon_0\hbar^2}{2m_e e^2/2} = \frac{4\pi\epsilon_0\hbar^2}{m_e e^2} = 0.52917725 \text{ \AA} \quad (\text{A.9})$$

The energy unit does change:

$$1 \text{ Ry} = \frac{\hbar^2}{2m_e a_0^2} = \frac{1}{2} \frac{\hbar^2}{m_e a_0^2} = 13.605693 \text{ eV} = \frac{1}{2} \text{ Ha} \quad (\text{A.10})$$

References

1. D. R. Hartree, Mat. Proc. Cambridge Philos. Soc. **24**, 89 (1928).

APPENDIX B

ORTHOGONAL PLANE WAVE

For now, we will try to approximate the time-independent Schrödinger equation so that we can achieve self-consistency. Let $V(r)$ be the potential seen by each electron. Then each energy eigenfunction will satisfy the following equation:

$$\hat{\mathcal{H}}\psi_i = \left[\hat{T} + \hat{V}(r) \right] \psi_i = E_i \psi_i \quad (\text{B.1})$$

Here, \hat{T} is the kinetic energy operator ($-\hbar^2 \nabla^2 / 2m$), and E_i is the energy of the i -th state. The next step is to distinguish between the core and the valence state. The index α will be used for the core electrons and v will be used for the valence band. The core states are the same as in the isolated ion, but their energies are different (*i.e.*, E_α is different):

$$\left[\hat{T} + \hat{V}(r) \right] \psi_\alpha = E_\alpha \psi_\alpha \quad (\text{B.2})$$

Here, the subscript α not only denotes the position of the ion but also the energy and angular momentum quantum numbers of the state in the equation. This is a well-defined Sturm–Liouville eigenvalue problem, apart from not knowing $V(r)$. We can approach the problem in several ways. The most common is to represent ψ_α by a basis set. Plane-wave basis sets are often used in band structure calculations. If we expand the Schrödinger Eqn. (B.2) with a complete set of states, then we may obtain a linear solution of simultaneous equations in the expansion coefficients. The

problem of solving differential equations then becomes a matrix diagonalization problem.

The choice of plane waves has its pros and cons. One of the difficulties of using plane waves is that, it typically requires a large number of plane waves to give a reasonable description of the wavefunction. Thus the solution becomes very difficult. In addition the core electrons have higher kinetic energy near the nucleus (see Fig. 2.2), which makes it even harder for plane waves to approximate those electrons. Herring [1] suggested that, rather than expanding the valence electron wave function in plane waves, a more rapidly convergent procedure is to expand in *orthogonalized* plane waves (OPWs). Hopefully, the expansions in terms of OPWs, would require fewer terms and therefore yield a faster calculation. The OPWs with wave number \mathbf{k} can be defined as follows:

$$OPW_{\mathbf{k}} = e^{i\mathbf{k}\cdot\mathbf{r}} - \sum_{\alpha} \psi_{\alpha}(\mathbf{r})\psi_{\alpha}^* e^{i\mathbf{k}\cdot\mathbf{r}} d\mathbf{r} \quad (B.3)$$

An example would be sodium, which has a ground state configuration of $1s^2 2s^2 2p^6 3s^1$. The core orbitals would be $1s^2 2s^2 2p^6$. For so-called simple metals (*i.e.*, Na, Mg, and Al), the electron wavefunction is rapidly convergent in the OPW basis. Before going any further, let's check whether this OPW (B.3) is orthogonal to the core states. Let's assume an arbitrary core wavefunction ψ_{β} and check the orthogonality with B.3:

$$\int \psi_{\beta}^*(\mathbf{r}) OPW_{\mathbf{k}} d\mathbf{r} = \int \psi_{\beta}^*(\mathbf{r}) e^{i\mathbf{k}\cdot\mathbf{r}} d\mathbf{r} - \sum_{\alpha} \delta_{\alpha\beta} \int \psi_{\alpha}^*(\mathbf{r}) e^{i\mathbf{k}\cdot\mathbf{r}} d\mathbf{r} = 0 \quad (B.4)$$

It is convenient to normalize the plane waves in the unit cell volume of the metal Ω , and we will use Dirac's bra-ket notation for the wave functions from now on. The plane wave becomes

$$|\mathbf{k}\rangle = \Omega^{-1/2} e^{i\mathbf{k}\cdot\mathbf{r}} \quad (B.5)$$

For core electron wave functions

$$|\alpha\rangle \equiv \psi_\alpha(\mathbf{r}) \quad (\text{B.6})$$

where $\langle\alpha| = |\alpha\rangle^*$, and

$$\langle\alpha|\mathbf{k}\rangle = \Omega^{-1/2} \int \psi_\alpha^*(\mathbf{r}) e^{i\mathbf{k}\cdot\mathbf{r}} d\mathbf{r} \quad (\text{B.7})$$

Thus the OPW equations becomes

$$OPW_{\mathbf{k}} = |\mathbf{k}\rangle - \sum_{\alpha} |\alpha\rangle \langle\alpha|\mathbf{k}\rangle \quad (\text{B.8})$$

The projection operator P can be defined as follows:

$$P = \sum_{\alpha} |\alpha\rangle\langle\alpha|. \quad (\text{B.9})$$

The P operator projects any function onto the core states. In terms of the P operator the OPW can take following form:

$$OPW_{\mathbf{k}} = (1 - P) |\mathbf{k}\rangle. \quad (\text{B.10})$$

Now, we can expand the valence-band (valence electron) state as a linear combination of OPWs:

$$\psi_k = \sum_q a_q(\mathbf{k})(1 - P) |\mathbf{k} + \mathbf{q}\rangle \quad (\text{B.11})$$

Before going a bit further, lets see how kinetic energy is represented by plane waves.

$$\langle q' | -\frac{\hbar^2}{2m} \nabla^2 | q \rangle = \frac{1}{2} \frac{\hbar^2}{2m} |\mathbf{q}|^2 \delta_{qq'} \quad (\text{B.12})$$

In the above approximation of kinetic energy we assumed the normalizing factor is one. Now we are going to expand B.2 with OPWs, and the Schrödinger equation

becomes

$$\hat{\mathcal{H}}\psi_k = \sum_q a_q(\mathbf{k}) \hat{\mathcal{H}}(1 - P) |\mathbf{k} + \mathbf{q}\rangle = E_k \sum_q a_q(\mathbf{k})(1 - P) |\mathbf{k} + \mathbf{q}\rangle \quad (\text{B.13})$$

where $\hat{\mathcal{H}}$ consists both the kinetic energy and the potential energy. Multiplying on the left by $\langle \mathbf{k} + \mathbf{q}' |$, and using Equation (B.12) we obtain

$$a_{q'}(\mathbf{k}) \frac{\hbar^2}{2m} |\mathbf{k} + \mathbf{q}'|^2 + \sum_q a_q(\mathbf{k}) [\langle \mathbf{k} + \mathbf{q}' | V |\mathbf{k} + \mathbf{q}\rangle - \sum_\alpha E_\alpha \langle \mathbf{k} + \mathbf{q}' | \alpha \rangle \langle \alpha | \mathbf{k} + \mathbf{q}\rangle] = \\ [a_{q'}(\mathbf{k}) - \sum_q a_q(\mathbf{k}) \langle \mathbf{k} + \mathbf{q}' | P |\mathbf{k} + \mathbf{q}\rangle] E_k \quad (\text{B.14})$$

The above equation can be solved by diagonalizing some of matrix element. If we can evaluate some of the various matrix elements (integrals), we obtain a set of linear algebraic equations.

References

1. C. Herring, Phys. Rev. **57**, 1169 (1940).

APPENDIX C

PROJECTOR AUGMENTED WAVE

The pseudopotential technique has proven to be accurate for a large variety of systems, but there is no strict guarantee that it will produce the same results as an all-electron calculation. The challenge with norm-conserving pseudopotentials is that they limit the *softness*. Another way to say it is that, it requires a high cut-off energy. In the plane-wave basis set for the pseudo wavefunctions is defined by the shortest wave length $\lambda = 2\pi/|\mathbf{G}|$, where \mathbf{G} is the wave vector. Projector augmented waves (PAW) introduces projectors and auxiliary localized functions to increase the softness of the pseudopotential, while at the same time keeping the full wavefunction. In this section, I will try to introduce PAW with basic formalism. The origin of the PAW method lies in a transformation that maps the true wavefunctions with their complete nodal structure onto auxiliary wavefunctions. The purpose of this transformation is to have smooth auxiliary wavefunctions that have a rapidly convergent plane-wave expansion. The PAW method was first proposed by Blöchl in 1994 [1]. The linear transformation is as follows:

$$|\Psi_n\rangle = \hat{\mathcal{T}} |\tilde{\Psi}_n\rangle \quad (\text{C.1})$$

where, $|\Psi_n\rangle$ is the true all-electron Kohn–Sham (KS) single-particle wavefunction, $|\tilde{\Psi}_n\rangle$ is an auxiliary smooth wavefunction, and $\hat{\mathcal{T}}$ is a linear transformation operator. Since the true wavefunctions are already smooth at a certain minimum distance from the core, $\tilde{\mathcal{T}}$ should only modify the wavefunction close to the nuclei. Thus

the transformation operator becomes

$$\tilde{\mathcal{T}} = 1 + \sum_a \tilde{\mathcal{T}}^a, \quad (\text{C.2})$$

where a is an atom index and $\tilde{\mathcal{T}}^a$ has no effect outside a certain atom-specific augmentation region, r_C^a . Inside the augmentation spheres, the true wavefunction can be expanded in the partial waves ϕ_i^a , for a corresponding auxiliary smooth partial wave can be defined as $\tilde{\phi}_i^a$, and they can be connected by the following relation:

$$|\phi_i^a\rangle = (1 + \hat{\mathcal{T}}^a) |\tilde{\phi}_i^a\rangle \Rightarrow \hat{\mathcal{T}}^a |\phi_i^a\rangle = |\phi_i^a\rangle - |\tilde{\phi}_i^a\rangle. \quad (\text{C.3})$$

Here a is an atom index and i denotes partial waves. Outside the augmentation sphere, the partial wave and its smooth counterpart should be identical:

$$\phi_i^a(\mathbf{r}) = \tilde{\phi}_i^a(\mathbf{r}) \quad \text{for } r > r_c^a \quad (\text{C.4})$$

Where $\phi_i^a(\mathbf{r}) = \langle \mathbf{r} | \phi_i^a \rangle$, and similar for $\tilde{\phi}_i^a$. If the smooth partial waves form a complete set inside the augmentation sphere, we can expand the smooth all-electron wavefunctions as

$$|\tilde{\Psi}_i^a\rangle = \sum_i P_{ni}^a |\tilde{\phi}_i^a\rangle \quad |\mathbf{r} - \mathbf{R}| < r_c^a \quad (\text{C.5})$$

where, P_{ni}^a are expansion coefficients, that need to be determined. The index a stands for atomic sites, i to distinguish different partial waves, and n is the principle to quantum numbers (ℓ, m) . The transformation operator connects the smooth pseudo wavefunction to true wavefunction.

$$|\Psi_n\rangle = \hat{\mathcal{T}} |\tilde{\Psi}_n\rangle = \sum_i P_{ni}^a |\psi_i^a\rangle \quad |\mathbf{r} - \mathbf{R}| < r_c^a \quad (\text{C.6})$$

Something really interesting about the above equation is that the true wavefunction has the same expansion coefficient (P_{ni}^a) as the pseudo-wavefunction. The transformation operator $\hat{\mathcal{T}}$ is required to be linear, the coefficient must be linear functionals of $|\tilde{\Psi}_n\rangle$, *i.e.*,

$$P_{ni}^a = \langle \tilde{p}_i^a | \tilde{\Psi}_n \rangle \quad (\text{C.7})$$

where $|\tilde{p}_i^a\rangle$ are some fixed functions termed smooth projector functions. As there is no overlap between the augmentation spheres, we expect the smooth all-electron wavefunction, $|\tilde{\Psi}_n^a\rangle = \sum_i |\tilde{\phi}_i^a\rangle \langle \tilde{p}_i^a | \tilde{\Psi}_n \rangle$. The projectors have to be localized within an augmentation region, so

$$\sum_i |\tilde{\phi}_i^a\rangle \langle \tilde{p}_i^a| = 1. \quad (\text{C.8})$$

This also implied that

$$\langle \tilde{p}_{i_1}^a | \tilde{\phi}_{i_2}^a \rangle = \delta_{i_1, i_2} \quad \text{for } r < r_c^a \quad (\text{C.9})$$

the projector functions should be orthonormal to the smooth partial waves inside the augmentation sphere. The choice of projectors and partial waves can be found more detailed form original work of Blöchl [1]. Using the completeness relation from Eqn. (C.8)

$$\hat{\mathcal{T}}^a = \sum_i \hat{\mathcal{T}}^a |\tilde{\phi}_i^a\rangle \langle \tilde{p}_i^a| = \sum_i \left(|\phi_i^a\rangle - |\tilde{\phi}_i^a\rangle \right) \langle \tilde{p}_i^a|. \quad (\text{C.10})$$

Remember, the operator $\hat{\mathcal{T}}^a$ operates only inside the sphere; outside sphere, it behaves like $|\phi_i^a\rangle - |\tilde{\phi}_i^a\rangle$. Thus, the total transformation operator becomes

$$\hat{\mathcal{T}} = 1 + \sum_a \sum_i \left(|\phi_i^a\rangle - |\tilde{\phi}_i^a\rangle \right) \langle \tilde{p}_i^a|. \quad (\text{C.11})$$

To summarize, we obtain the all-electron KS wavefunction $|\Psi_n(\mathbf{r})\rangle = \langle \mathbf{r} | \Psi_n \rangle$ from the transformation

$$\Psi_n(\mathbf{r}) = \tilde{\Psi}_n(\mathbf{r}) + \sum_a \sum_i \left(\phi_i^a(\mathbf{r}) - \tilde{\phi}_i^a(\mathbf{r}) \right) \langle \tilde{p}_i^a | \tilde{\psi}_n \rangle \quad (\text{C.12})$$

The equation above has three different components on the right. The first is the auxiliary wavefunction. The second term is the sum of partial waves, the last term is the sum of pseudo-partial waves that must be subtracted inside the augmentation region. To make it a simple KS wavefunction representation

$$\psi_n(\mathbf{r}) = \tilde{\psi}_n(\mathbf{r}) + \sum_a \left(\psi_n^a(\mathbf{r} - \mathbf{R}^a) - \tilde{\psi}_n^a(\mathbf{r} - \mathbf{R}^a) \right). \quad (\text{C.13})$$

The trouble with the original KS wavefunction was that they display oscillations near the nucleus and smooth behavior away from the nucleus. By decomposing the wavefunction in the manner of Eqn. (C.12), the achievement is that the original wavefunction is separated into auxiliary wavefunctions that are smooth everywhere.

C.1 PAW Pseudopotential Generation

The PAW calculation method requires a set of basis functions (partial-waves) and projector functions as well as some additional atomic data in the so called *PAW dataset*. The PAW dataset is generated using the following procedure:

- Solve the all-electron atomic problem in the DFT formalism using an exchange–correlation functional (with the scalar-relativistic approximation). It is a spherical problem and usually solved with a logarithmic grid.
- Separation of core and valence electrons. The core density is then deduced from the core electron wavefunctions. For a given radius (r_{core}), the outer density is calculated so that the core density is identical to the outer.
- Choose the PAW basis (number of partial waves and projectors).
- Generation of the pseudo partial-waves.
- Test the PAW dataset on an electronic structure calculation. Repeat the procedure if necessary to match the calculated property's agreement with experiment or with all-electron calculations.

References

1. P. E. Blöchl, Phys. Rev. B **50**, 17953 (1994).

The atompaw input file used to generate the pseudopotential for uranium in Ch. 4 is below:

```

1 U 92
2 GGA-PBE scalarrelativistic loggridv4 700
3 7 6 6 5 0 !6s2 6p6 5f3 6d1 7s2 (from Beelar (2012), ns_max np_max
   nd_max nf_max ng_max
4 6 2 1 !6d1, only empty or partially occupied shells are entered
5 5 3 3 !5f3
6 0 0 0
7 C !1s2 1
8 C !2s2 2
9 C !3s2 3
10 C !4s2 4
11 C !5s2 5
12 V !6s2 6 1
13 V !7s2 7 2
14 C !2p6 8
15 C !3p6 9
16 C !4p6 10
17 C !5p6 11
18 V !6p6 12 3
19 C !3d10 13
20 C !4d10 14
21 C !5d10 15
22 V !6d1 16 4
23 C !4f14 17
24 V !5f3 18 5
25 3
26 2.5 2.02 1.5 1.8 !rpaw, rshape, rvloc, rcore, in a.u , changesd the
   rshape for the first time below 2.0
27 n
28 y      !one additional p partial wave
29 0.00
30 n      !no additional p partial wave
31 y      !one additional d partial wave
32 0.2    !
33 n      !no additional d partial wave
34 y      !one additional f partial wave
35 3.0    !no additional f partial wave
36 n      !no additional f partial wave
37 custom rrkj besselshape !for PWscf, UPF format needs bessels
38 4 0.0 !bessel      !l quantum number, reference energy (Ry),
   bessel for simplicity
39 1.5    !1 s      ! r_c matching radius for second s partial wave
40 1.5    !2 s      ! rc for s
41 2.5    !3 p      ! rc for p
42 2.5    !4 p      ! rc for p
43 2.5    !5 d      ! rc for d, 1.3 gives very good result
44 2.5    !6 d      ! rc for d, 1.3 gives very good result, 4.0 energy
45 2.5    !7 f      ! rc for f
46 2.5    !8 f      ! rc for f
47 PWSCFOUT
48 default
49 0

```

APPENDIX D

FINITE ELEMENT METHOD IN MOOSE

This appendix discusses how a partial differential equation can be implemented in the MOOSE Framework. The strong form of the heat diffusion equation without a source term is

$$\nabla \cdot (K(T)\nabla T) = 0.$$

Multiplying by a test function (\mathcal{T}_f) and integrating over the domain Ω gives

$$\begin{aligned} \int_{\Omega} \mathcal{T}_f (\nabla \cdot \underbrace{K(T)\nabla T}_{\mathcal{G}}) &= 0 \\ \int_{\Omega} \mathcal{T}_f \nabla \cdot \mathcal{G} &= 0 \\ \int_{\Omega} \nabla \cdot (\mathcal{T}_f \mathcal{G}) - \int_{\Omega} \nabla \mathcal{T}_f \cdot \mathcal{G} &= 0 \end{aligned} \tag{D.1}$$

Using the divergence theorem,

$$\int_{\Omega} \nabla \cdot \vec{\mathbf{g}} \, dx = \int_{\partial\Omega} \vec{\mathbf{g}} \cdot \hat{\mathbf{n}} \, ds \tag{D.2}$$

Eqn. (D.1) becomes:

$$\begin{aligned} \int_{\partial\Omega} \mathcal{T}_f \mathcal{G} \cdot \hat{\mathbf{n}} \, ds - \int_{\Omega} \nabla \mathcal{T}_f \cdot \mathcal{G} \, dx &= 0 \\ \int_{\Omega} \nabla \mathcal{T}_f \cdot K(T)\nabla T \, dx - \int_{\partial\Omega} \mathcal{T}_f K(T)\nabla T \cdot \hat{\mathbf{n}} \, ds &= 0 \end{aligned}$$

Using the inner product notation, the above equation can be written as follows:

$$(\nabla \mathcal{T}_f, K \nabla T) - \langle \mathcal{T}_f, K \nabla T \cdot \hat{n} \rangle = 0 \quad (\text{D.3})$$

Each of these term inherits an existing MOOSE type to solve the problem.

$$\underbrace{(\nabla \mathcal{T}_f, K \nabla T)}_{\text{Kernel}} - \underbrace{\langle \mathcal{T}_f, K \nabla T \cdot \hat{n} \rangle}_{\text{Boundary Condition}} = 0 \quad (\text{D.4})$$

Source files containing a kernel and boundary conditions are given in Appendix E.

APPENDIX E

INPUT FILES

Input files for different software are included in this chapter. Because of the complexity and number, I have only included samples of them.

E.1 MOOSE Framework

This is the `main.C` file for MOOSE simulation. Depends on the problem, MOOSE requires a number of header files and source files.

```
1  /* this is a main app file created for the purpose of simulating
   heat conduction
2  *      This is file is created by Rafi, Sepetember 27, 2016
3  *      ****
4
5  #include "HeatCondRafiApp.h"
6  #include "MooseInit.h"
7  #include "Moose.h"
8  #include "MooseApp.h"
9  #include "AppFactory.h"
10
11 // Creat a performance log
12 PerfLog Moose::perf_log("HeatCondRafi");
13
14 //Begin the main problem.
15 int main(int argc, char *argv[])
16 {
17     // Initialize MPI, solvers and MOOSE
18     MooseInit init(argc, argv);
19
20     // Register this application's MooseApp and any it depends on
21     HeatCondRafiApp::registerApps();
22
23     // This creates dynamic memory that we're responsible for
24     // deleting
25     //MooseApp * app = AppFactory::createAppShared("HeatCondRafiApp",
26     //    argc, argv);
26     std::shared_ptr<MooseApp> app = AppFactory::createAppShared(
27     "HeatCondRafiApp", argc, argv);
28
29     //Execute the application
```

```
28     app->run();
29
30     // Free up the memory we created earlier
31     //delete app;
32
33     return 0;
34 }
```

This is a sample of source file (kernel in MOOSE) of heat transfer in U-10Mo.

```
1 // this file is edited by Rafi for temperature dependent thermal
2 // conductivity
3 #include "Tempdepk.h"
4
5 template<>
6 InputParameters validParams<Tempdepk>()
7 {
8     InputParameters params = validParams<Diffusion>();
9     params.addClassDescription("This will solve heat diffusion with
10    temperature dependent thermal conductivity");
11    return params;
12 }
13
14 Tempdepk::Tempdepk(const InputParameters & parameters) :
15     Diffusion(parameters),
16     _thermal_conductivity(getMaterialProperty<Real>("thermal_conductivity"))
17     /*be sure u use the "thermal_conductivity",
18     otherwise it will
19 not read the thermal_conductivity from the input*/
20 {
21 }
22
23 Real
24 Tempdepk::computeQpResidual()
25 {
26     //return _grad_u[_qp] * _grad_test[_i][_qp];
27     //Real _k=0.606+0.0351*_u[_qp]; // from D.E. Burkes et al./ Journal
28     // of Nuc Material 2010
29
30     return _thermal_conductivity[_qp]*Diffusion::computeQpResidual();
31 }
32
33 Real
34 Tempdepk::computeQpJacobian()
35 {
36     //Real _k=0.606+0.0351*_u[_qp];
37     //return _grad_phi[_j][_qp] * _grad_test[_i][_qp];
38
39     return _thermal_conductivity[_qp]*Diffusion::computeQpJacobian();
40 }
```

```

1 // this file was edited by Rafi for temperature dependent thermal
2 // conductivity
3 #include "TXenon.h"
4
5 template<>
6 InputParameters validParams<TXenon>()
7 {
8     InputParameters params = validParams<Diffusion>();
9     params.addClassDescription("This will solve heat diffusion with
10      temperature dependent thermal conductivity");
11     return params;
12 }
13
14 TXenon::TXenon(const InputParameters & parameters) :
15     Diffusion(parameters),
16     _thermal_conductivity(getMaterialProperty<Real>(""
17         "thermal_conductivity")) /*be sure u use the "thermal_conductivity",
18         otherwise it will
19 not read the thermal_conductivity from the input*/
20 {
21 }
22
23 Real
24 TXenon::computeQpResidual()
25 {
26     //return _grad_u[_qp] * _grad_test[_i][_qp];
27     //Real _k=0.606+0.0351*u[_qp]; // from D.E. Burkes et al./ Journal
28     // of Nuc Material 2010
29
30     /* return _thermal_conductivity[_qp]*Diffusion::computeQpResidual() +
31        380E3*_test[_i][_qp]; */
32
33 // the above one for a constant forcing function
34
35     return _thermal_conductivity[_qp]*Diffusion::computeQpResidual();
36 }
37
38 Real
39 TXenon::computeQpJacobian()
40 {
41     //Real _k=0.606+0.0351*u[_qp];
42     //return _grad_phi[_j][_qp] * _grad_test[_i][_qp];
43
44     return _thermal_conductivity[_qp]*Diffusion::computeQpJacobian() +
45        (-2*4.72984E-09*u[_qp]*2.+2.0891E-5)*_grad_u[_qp]*_grad_test[_i][
46        _qp];
47 }

```

Material source code for U-10Mo properties.

```
1 // this file was edited by Rafi January 24, 2017
2 //
3 #include "Tconductivity.h"
4
5 template<>
6 InputParameters validParams<Tconductivity>()
7 {
8     InputParameters params = validParams<Material>();
9     // we do not need to add any data from the input file
10    params.addClassDescription("This is to calculate the temperature
11        dependent thermal conductivity of U-10Mo");
12    // the "temperature" variable has to be defined in the input files
13    params.addCoupledVar("dep_variable", "The thermal conductivity is
14        calculated from temperature");
15    return params;
16 }
17
18 Tconductivity::Tconductivity(const InputParameters & parameters) :
19     Material(parameters),
20
21     // Declare material properties. This returns references that we
22     // hold onto as member variables
23     //_permeability(declareProperty<Real>("permeability")),
24     _thermal_conductivity(declareProperty<Real>("thermal_conductivity"))
25     ,
26     //_dep_variable(isCoupled("dep_variable"))
27     _dep_variable(coupledValue("dep_variable"))
28 {
29 }
30
31 void
32 Tconductivity::computeQpProperties()
33 {
34
35     // Sample the LinearInterpolation object to get the permeability for
36     // the ball size
37     //_permeability[_qp] = _permeability_interpolation.sample(
38     //    _ball_radius);
39     _thermal_conductivity[_qp]=0.606+0.0351*_dep_variable[_qp];
40 }
```

Source file for xenon material properties.

```
1 // this file was edited by Rafi February 13, 2017
2 //
3 #include "XenonT.h"
4
5 template<>
6 InputParameters validParams<XenonT>()
7 {
8     InputParameters params = validParams<Material>();
9     // we do not need to add any data from the input file
10    params.addClassDescription("This is to calculate the temperature
11        dependent thermal conductivity of Xenon");
12    // the "temperature" variable has to be defined in the input files
13    params.addCoupledVar("dep_variable", "The thermal conductivity is
14        calculated from temperature");
15    return params;
16 }
17
18
19
20 XenonT::XenonT(const InputParameters & parameters) :
21     Material(parameters),
22
23     // Declare material properties. This returns references that we
24     // hold onto as member variables
25     //_permeability(declareProperty<Real>("permeability")),
26     _thermal_conductivity(declareProperty<Real>("thermal_conductivity"))
27
28     ,
29     //_dep_variable(isCoupled("dep_variable"))
30     _dep_variable(coupledValue("dep_variable"))
31 {
32 }
33
34 void
35 XenonT::computeQpProperties()
36 {
37
38     // Sample the LinearInterpolation object to get the permeability for
39     // the ball size
40     //_permeability[_qp] = _permeability_interpolation.sample(
41     // _ball_radius);
42     //_thermal_conductivity[_qp]=0.000000001+0.0000000001*_dep_variable
43     //[_qp];
44     /*above correlation is wrong, is calculated wrong, the next equation
45      is calcuated from Robinovich et al. Thermophysical
46      sical property of Neon, Argon, Krypton, and Xenon */
47
48     _thermal_conductivity[_qp]=-4.72984E-09*_dep_variable[_qp]*
49     _dep_variable[_qp] + 2.0891E-5*_dep_variable[_qp]+ 2.83137E-05 ;
50
51
52 }
```

Source file for heat flux calculation.

```
1 #include "HeatFlux.h"
2
3
4 template<>
5 InputParameters validParams<HeatFlux>()
6 {
7     InputParameters params = validParams<AuxKernel>();
8
9     MooseEnum component("x y z");
10    // Declare the options for a MooseEnum.
11    // These options will be presented to the user in Peacock
12    // and if something other than these options is in the input file
13    // an error will be printed
14    params.addClassDescription("This is to calculate the heat flux for
15        over all material");
16    // Add a "coupling parameter" to get a variable from the input file.
17    params.addRequiredCoupledVar("field_temperature", "The temperature
18        field.");
19    params.addRequiredParam<MooseEnum>("component", component, "The
20        desired component of temperature");
21
22 HeatFlux::HeatFlux(const InputParameters & parameters) :
23     AuxKernel(parameters),
24
25     // Get the gradient of the variable
26     _temperature_gradient(coupledGradient("field_temperature")),
27
28     // Snag thermal_conductivity from the Material system.
29     // Only AuxKernels operating on Elemental Auxiliary Variables can
30     // do this
31     _t_thermal_conductivity(getMaterialProperty<Real>(
32         "thermal_conductivity")),
33     _component(getParam<MooseEnum>("component"))
34
35
36 Real
37 HeatFlux::computeValue()
38 {
39     // Access the gradient of the pressure at this quadrature point
40     // Then pull out the "component" of it we are looking for (x, y or z
41     )
42     // Note that getting a particular component of a gradient is done
43     // using the
44     // parenthesis operator
45     return _t_thermal_conductivity[_qp]*_temperature_gradient[_qp](
46         _component);
47 }
```

This source file is to calculate the gradient of the temperature.

```
1 #include "TGradient.h"
2
3
4 template<>
5 InputParameters validParams<TGradient>()
6 {
7     InputParameters params = validParams<AuxKernel>();
8
9     // Declare the options for a MooseEnum.
10    // These options will be presented to the user in Peacock
11    // and if something other than these options is in the input file
12    // an error will be printed
13    params.addClassDescription("This is to calculate the temperature
14        gradient for over all material");
15    // Add a "coupling parameter" to get a variable from the input file.
16    //params.addRequiredCoupledVar("field_temperature", "The temperature
17        field.");
18    MooseEnum component("x y z");
19
20    // Use the MooseEnum to add a parameter called "component"
21    params.addRequiredCoupledVar("field_temperature", "The Temperature
22        field");
23    params.addRequiredParam<MooseEnum>("component", component, "The
24        desired component of velocity.");
25    return params;
26 }
27
28 TGradient::TGradient(const InputParameters & parameters) :
29     AuxKernel(parameters),
30
31     // Get the gradient of the variable
32     _temperature_gradient(coupledGradient("field_temperature")),
33
34     _component(getParam<MooseEnum>("component"))
35     // Snag thermal_conductivity from the Material system.
36     // Only AuxKernels operating on Elemental Auxiliary Variables can
37     // do this
38     //_t_thermal_conductivity(getMaterialProperty<Real>("
39     //thermal_conductivity"))
40
41 {
42
43     Real
44     TGradient::computeValue()
45
46     {
47         // Access the gradient of the pressure at this quadrature point
48         // Then pull out the "component" of it we are looking for (x, y or z
49             )
50         // Note that getting a particular component of a gradient is done
51             using the
52             // parenthesis operator
53         return _temperature_gradient[_qp](_component);
54     }
55 }
```

For every source file, we need header files. The required header files are below.

Tempdepk.h

```
1 // this file created by Rafi, January 24, 2017
2 #ifndef TEMPDEPK_H
3 #define TEMPDEPK_H
4 #include "Diffusion.h"
5 class Tempdepk;
6 template<>
7 InputParameters validParams<Tempdepk>();
8
9 /**
10  * This kernel will solve a temperature dependent thermal conductivity
11  * with diffusion of temperature
12 */
13 class Tempdepk : public Diffusion
14 {
15 public:
16     Tempdepk(const InputParameters & parameters);
17 protected:
18     virtual Real computeQpResidual() override;
19     virtual Real computeQpJacobian() override;
20     // creating a moose array for material property
21     const MaterialProperty<Real> & _thermal_conductivity;
22 };
23 #endif
```

```

TXenon.h

1 / this file created by Rafi, January 24, 2017
2 #ifndef TXENON_H
3 #define TXENON_H
4
5 #include "Diffusion.h"
6
7 class TXenon;
8 template<>
9 InputParameters validParams<TXenon>();
10
11 /**
12 * This kernel will solve a temperature dependent thermal conductivity
13 * with diffusion of temperature
14 */
15 class TXenon : public Diffusion
16 {
17 public:
18     TXenon(const InputParameters & parameters);
19 protected:
20     virtual Real computeQpResidual() override;
21
22     virtual Real computeQpJacobian() override;
23 // creating a moose array for material property
24
25     const MaterialProperty<Real> & _thermal_conductivity;
26 };
27 #endif

```

```

1 // this file was created by Rafi on February 13, 2017
2
3 #ifndef TCONDUCTIVITY_H
4 #define TCONDUCTIVITY_H
5
6 #include "Material.h"
7
8 class Tconductivity;
9
10 template<>
11 InputParameters validParams<Tconductivity>();
12
13 /**
14 * Material objects inherit from Material and override
15 * computeQpProperties.
16 *
17 * Their job is to declare properties for use by other objects in the
18 * calculation such as Kernels and BoundaryConditions.
19 */
20 class Tconductivity : public Material
21 {
22 public:
23     Tconductivity(const InputParameters & parameters);
24 protected:
25     /**
26     * Necessary override. This is where the values of the properties
27     * are computed.
28     */
29     virtual void computeQpProperties() override;
30
31 private:
32     // The thermal conductivity
33     MaterialProperty<Real> & _thermal_conductivity; // for u-10 Mo
34
35     // const VariableGradient & _dep_variable; // this will get the
36     // temperature
37     //std::vector<const VariableValue> & _dep_variable;
38     //VariableValue<Real> & _dep_variable;
39     const VariableValue & _dep_variable;
40 };
41 #endif //Tconductivity

```

XenonT.h

```
1 / this file was created by Rafi on February 13, 2017
2 // The reference is Rabinovich et al.
3 // Thermophysical Properties of Neon, Argon, Krypton and Xenon// for
4 // the purpose of temperature dependent thermal conductivity for U-10
5 // Mo
6
7 #ifndef XENONT_H
8 #define XENONT_H
9
10 template<>
11 InputParameters validParams<XenonT>();
12
13 /**
14 * Material objects inherit from Material and override
15 * computeQpProperties.
16 *
17 * Their job is to declare properties for use by other objects in the
18 * calculation such as Kernels and BoundaryConditions.
19 */
20 class XenonT : public Material
21 {
22 public:
23     XenonT(const InputParameters & parameters);
24 protected:
25 /**
26 * Necessary override. This is where the values of the properties
27 * are computed.
28 */
29     virtual void computeQpProperties() override;
30 private:
31     // The thermal conductivity
32     MaterialProperty<Real> & _thermal_conductivity; // for u-10 Mo
33
34     // const VariableGradient & _dep_variable; // this will get the
35     // temperature
36     //std::vector<const VariableValue> & _dep_variable;
37     //VariableValue<Real> & _dep_variable;
38     const VariableValue & _dep_variable;
39 };
40
41 #endif //XENONT_H
```

HeatFlux.h

```
1 #ifndef HEATFLUX_H
2 #define HEATFLUX_H
3
4 #include "AuxKernel.h"
5
6 //Forward Declarations
7 class HeatFlux;
8
9 template<>
10 InputParameters validParams<HeatFlux>();
11
12 /**
13 * Constant auxiliary value
14 */
15 class HeatFlux : public AuxKernel
16 {
17 public:
18     HeatFlux(const InputParameters & parameters);
19
20     virtual ~HeatFlux() {}
21
22 protected:
23     /**
24      * AuxKernels MUST override computeValue.  computeValue() is called
25      * on
26      * every quadrature point.  For Nodal Auxiliary variables those
27      * quadrature
28      * points coincide with the nodes.
29      */
30     virtual Real computeValue() override;
31
32     /// The gradient of a coupled variable
33     const VariableGradient & _temperature_gradient;
34
35     /// Holds the permeability and viscosity from the material system
36     const MaterialProperty<Real> & _t_thermal_conductivity;
37     // const MaterialProperty<Real> & _viscosity;
38
39     int _component;
40 };
41 #endif // end of HEATFLUX_H
```

```

TGradient.h
1 #ifndef TGRADIENT_H
2 #define TGRADIENT_H
3
4 #include "AuxKernel.h"
5
6 //Forward Declarations
7 class TGradient;
8
9 template<>
10 InputParameters validParams<TGradient>();
11
12 /**
13 * Constant auxiliary value
14 */
15 class TGradient : public AuxKernel
16 {
17 public:
18     TGradient(const InputParameters & parameters);
19
20     virtual ~TGradient() {}
21
22 protected:
23 /**
24 * AuxKernels MUST override computeValue. computeValue() is called
25 on
26 * every quadrature point. For Nodal Auxiliary variables those
27 quadrature
28 * points coincide with the nodes.
29 */
30     virtual Real computeValue() override;
31
32     /// The gradient of a coupled variable
33     const VariableGradient & _temperature_gradient;
34
35     /// Holds the permeability and viscosity from the material system
36     //const MaterialProperty<Real> & _t_thermal_conductivity;
37     int _component;
38     // const MaterialProperty<Real> & _viscosity;
39 };
40 #endif // end of TGRADIENT_H

```

E.2 ATOMPAW

This is an input file for Atompaw to generate the PAW pseudopotential for electronic structure calculations on uranium.

```

1 U 92
2 GGA-PBE scalarrelativistic loggridv4 700
3 7 6 6 5 0
4 6 2 1
5 5 3 3
6 0 0 0
7 C !1s2 1
8 C !2s2 2
9 C !3s2 3
10 C !4s2 4
11 C !5s2 5
12 V !6s2 6 1
13 V !7s2 7 2
14 C !2p6 8
15 C !3p6 9
16 C !4p6 10
17 C !5p6 11
18 V !6p6 12 3
19 C !3d10 13
20 C !4d10 14
21 C !5d10 15
22 V !6d1 16 4
23 C !4f14 17
24 V !5f3 18 5
25 3
26 2.5 2.02 1.5 1.8 !rpaw, rshape, rvloc, rcore, in a.u
27 n
28 y !one additional p partial wave
29 0.00
30 n !no additional p partial wave
31 y !one additional d partial wave
32 0.2 !
33 n !no additional d partial wave
34 y !one additional f partial wave
35 3.0
36 n !no additional f partial wave
37 custom rrkj besselshape !UPF format needs bessels
38 4 0.0 !bessel !l quantum number, reference energy (Ry),
           bessel for simplicity
39 1.3 !1 s ! rc s partial wave
40 1.3 !2 s ! rc for s
41 2.5 !3 p ! rc for p
42 2.5 !4 p ! rc for p
43 1.55 !5 d ! rc for d, 1.3 gives very good result
44 1.55 !6 d ! rc for d, 1.3 gives very good result, 4.0
           energy
45 2.5 !7 f ! rc for f
46 2.5 !8 f ! rc for f
47 PWSCFOUT
48 default
49 0

```

E.3 DFT Calculation

E.3.1 SCF of a Primitive Cell

This is sample input file to calculate the self consistent field study using QUANTUMESPRESSO. It contains the lattice parameter of α -uranium.

```
1 &CONTROL
2           title = 'alphaU'
3           calculation = 'scf'
4           restart_mode = 'from_scratch'
5           outdir = '/home/iasir/quantum_espresso'
6           pseudo_dir = '/home/iasir/quantum_espresso'
7           prefix = 'alphaU'
8           verbosity = 'default'
9           tstress = .true.
10          tprnfor = .true.
11 /
12 &SYSTEM
13           ibrav = 0
14           A = 2.8383
15           at = 2
16           ntyp = 1
17           ntyp = 1
18           ecutwfc = 50
19           ecutrho = 250
20           smearing = 'methfessel-paxton'
21 /
22 &ELECTRONS
23           diagonalization = 'david'
24 /
25 &IONS
26
27 /
28 CELL_PARAMETERS {alat}
29   0.500000000000000 -1.031658697792153  0.000000000000000
30   0.500000000000000  1.031658697792153  0.000000000000000
31   0.000000000000000  0.000000000000000  1.73379271551118
32 ATOMIC_SPECIES
33   U  238.0290000000  U.GGA-PBE-paw.UPF
34
35 ATOMIC_POSITIONS {crystal}
36 U  0.0986000000000000 -0.0986000000000000 -0.250000000000000
37 U -0.0986000000000000  0.0986000000000000  0.250000000000000
38
39 K_POINTS automatic
40 20 20 26 0 0 0
```

E.3.2 Supercell of γ -Uranium

The following input is for performing a relax calculation using supercell of γ -uranium with molybdenum and xenon.

```

1 &CONTROL
2                               title  = 'supercellgammaU'
3                               calculation = 'relax'
4                               restart_mode = 'from_scratch'
5                               outdir = '/group/hammond/sysyphus/3x3/2prim-2
6                               nd/im02',
7                               pp_dir',
8                               pseudo_dir = '/group/hammond/sysyphus/
9                               prefix = 'supercell_gammaU'
10                              etot_conv_thr = 1.0D-6
11                              forc_conv_thr = 1.0D-6
12                              verbosity = 'default'
13                              tstress = .true.
14                              tprnfor = .true.
15                              nstep = 200
16 /
17 &SYSTEM
18                               ibrav = 0
19                               A = 10.35
20                               nat = 53
21                               ntyp = 3
22                               ecutwfc = 50
23                               ecutrho = 260
24                               occupations = 'smearing'
25                               degauss = 0.02
26                               smearing = 'mp'
27 /
28 &ELECTRONS
29                               diagonalization = 'david'
30                               electron_maxstep = 900
31                               mixing_beta = 0.1
32 /
33 &IONS
34 /
35 &CELL
36 /
37 CELL_PARAMETERS {alat}
38   1.00    0.00    0.00
39   0.00    1.00    0.00
40   0.00    0.00    1.00
41
42 ATOMIC_SPECIES
43   U  238.02800  U.GGA-PBE-paw.UPF
44   Xe 131.29    Xe.GGA-PBE-paw.UPF
45   Mo 95.94     Mo.GGA-PBE-paw.UPF
46
47 ATOMIC_POSITIONS (crystal)
48 U      0.0000000000  0.0000000000  0.0000000000  0  0  0
49 U      0.210984461   0.204688901   0.229195736   0  0  0
50 U      0.0000000000  0.0000000000  0.3333333333  0  0  0
51 U      0.0000000000  0.0000000000  0.6666666667  0  0  0
52 U      0.3333333333  0.0000000000  0.0000000000  0  0  0

```

53	U	0.6666666667	0.0000000000	0.0000000000	0	0	0
54	U	0.0000000000	0.3333333333	0.0000000000	0	0	0
55	U	0.0000000000	0.6666666667	0.0000000000	0	0	0
56	U	0.137231091	0.153757182	0.530873483			
57	U	0.174376372	0.129124170	0.859923969			
58	U	0.526508957	0.134953713	0.159596399			
59	U	0.862089662	0.133706169	0.175813941			
60	U	0.158683128	0.524614679	0.202129442			
61	U	0.148170903	0.848856345	0.127554382			
62	U	0.0000000000	0.3333333333	0.3333333333	0	0	0
63	U	0.0000000000	0.6666666667	0.6666666667	0	0	0
64	U	0.0000000000	0.6666666667	0.3333333333	0	0	0
65	U	0.0000000000	0.3333333333	0.6666666667	0	0	0
66	U	0.3333333333	0.0000000000	0.3333333333	0	0	0
67	U	0.6666666667	0.0000000000	0.6666666667	0	0	0
68	U	0.3333333333	0.0000000000	0.6666666667	0	0	0
69	U	0.6666666667	0.0000000000	0.3333333333	0	0	0
70	U	0.3333333333	0.3333333333	0.0000000000	0	0	0
71	U	0.6666666667	0.6666666667	0.0000000000	0	0	0
72	U	0.6666666667	0.3333333333	0.0000000000	0	0	0
73	U	0.3333333333	0.6666666667	0.0000000000	0	0	0
74	U	0.137231091	0.153757182	0.530873483			
75	U	0.174376372	0.129124170	0.859923969			
76	U	0.526508957	0.134953713	0.159596399			
77	U	0.862089662	0.133706169	0.175813941			
78	U	0.158683128	0.524614679	0.202129442			
79	U	0.148170903	0.848856345	0.127554382			
80	U	0.0000000000	0.3333333333	0.3333333333	0	0	0
81	U	0.0000000000	0.6666666667	0.6666666667	0	0	0
82	U	0.0000000000	0.6666666667	0.3333333333	0	0	0
83	U	0.0000000000	0.3333333333	0.6666666667	0	0	0
84	U	0.3333333333	0.0000000000	0.3333333333	0	0	0
85	U	0.6666666667	0.0000000000	0.6666666667	0	0	0
86	U	0.3333333333	0.0000000000	0.6666666667	0	0	0
87	U	0.6666666667	0.0000000000	0.3333333333	0	0	0
88	U	0.3333333333	0.3333333333	0.0000000000	0	0	0
89	U	0.6666666667	0.6666666667	0.0000000000	0	0	0
90	U	0.6666666667	0.3333333333	0.0000000000	0	0	0
91	U	0.3333333333	0.6666666667	0.0000000000	0	0	0
92	U	0.179014193	0.490220525	0.515819257			
93	U	0.211529991	0.769018260	0.787411348			
94	U	0.174791835	0.807115343	0.456517964			
95	U	0.138750516	0.465098823	0.842421942			
96	U	0.460277126	0.148072446	0.492479910			
97	U	0.853185555	0.205057669	0.814927365			
98	U	0.517574914	0.155283842	0.808674767			
99	U	0.797006954	0.141631469	0.505322942			
100	U	0.472193561	0.445111610	0.164972643			
101	U	0.797427656	0.818792499	0.205498630			
102	U	0.849105689	0.447077449	0.157067159			
103	U	0.477316581	0.824076376	0.198019584			
104	U	0.357811109	0.358247142	0.377740929			
105	Mo	0.317120589	0.314631326	0.680448732			
106	Mo	0.607263578	0.351682511	0.642824966			
107	U	0.340594168	0.659454747	0.325699754			
108	U	0.361075015	0.621507036	0.637398808			
109	Mo	0.660724290	0.302342735	0.343336983			
110	U	0.864625684	0.823864687	0.866239386			
111	U	0.857300550	0.828682348	0.537389462			
112	U	0.459239378	0.501675726	0.851462699			

113 U 0.787353995 0.504077862 0.849782744
114 U 0.483651729 0.821500104 0.546062842
115 U 0.525967152 0.834454416 0.872311707
116 U 0.803327765 0.439115905 0.558594712
117 U 0.678734725 0.684452016 0.648081893
118 Xe 0.649495337 0.596675850 0.354354426
119
120
121
122 !Xe 0.500000000 0.500000000 0.500000000
123
124 K_POINTS automatic
125 4 4 4 0 0 0

E.3.3 Nudged Elastic Band Calculation

The following input file is to perform nudged elastic band calculation using QUANTUMESPRESSO.

```
1 BEGIN
2 BEGIN_PATH_INPUT
3 &PATH
4   restart_mode      = 'from_scratch',
5   string_method     = 'neb',
6   nstep_path        = 100,
7   ds                = 1.00,
8   opt_scheme         = "broyden",
9   num_of_images     = 5,
10  k_max              = 0.6169D0,
11  k_min              = 0.6169D0,
12  CI_scheme          = "auto",
13  path_thr           = 0.1D0,
14 /
15 END_PATH_INPUT
16 BEGIN_ENGINE_INPUT
17 &CONTROL
18   outdir = '/group/hammond/sysyphus/3x3/2prim-2nd/neb',
19   pseudo_dir = '/group/hammond/sysyphus/pp_dir',
20   prefix = 'xe@1neb' ,
21   verbosity = 'high' ,
22   etot_conv_thr = 1e-6 ,
23   forc_conv_thr = 1e-5 ,
24   nstep = 200 ,
25   tstress = .true.,
26   tprnfor = .true.,
27   max_seconds = 1.0D+18,
28 /
29 &SYSTEM
30   ibrav = 0,
31   A = 10.35,
32   nat = 53,
33   ntyp = 3,
34   ecutwfc = 50,
35   ecutrho = 260,
36   occupations = 'smearing',
37   degauss = 0.02,
38   smearing = 'mp',
39 /
40 &ELECTRONS
41   electron_maxstep = 900,
42   conv_thr = 1e-7 ,
43   mixing_beta = 0.1 ,
44   diagonalization = 'david' ,
45 /
46 &IONS
47 /
48 ATOMIC_SPECIES
49   U 238.02800    U.GGA-PBE-paw.UPF
50   Xe 131.29      Xe.GGA-PBE-paw.UPF
51   Mo 95.94       Mo.GGA-PBE-paw.UPF
52 BEGIN_POSITIONS
53 FIRST_IMAGE
54 ATOMIC_POSITIONS (crystal)
```

55	U	0.0000000000	0.0000000000	0.0000000000	0	0	0
56	U	0.175109924	0.144562064	0.206801126			
57	U	0.0000000000	0.0000000000	0.3333333333	0	0	0
58	U	0.0000000000	0.0000000000	0.6666666667	0	0	0
59	U	0.3333333333	0.0000000000	0.0000000000	0	0	0
60	U	0.6666666667	0.0000000000	0.0000000000	0	0	0
61	U	0.0000000000	0.3333333333	0.0000000000	0	0	0
62	U	0.0000000000	0.6666666667	0.0000000000	0	0	0
63	U	0.172966137	0.162988305	0.549703444			
64	U	0.170611892	0.151612185	0.878052143			
65	U	0.495257014	0.208922221	0.160293502			
66	U	0.831518767	0.131820848	0.145403232			
67	U	0.187663248	0.516383543	0.207043480			
68	U	0.141733995	0.833501726	0.124057856			
69	U	0.0000000000	0.3333333333	0.3333333333	0	0	0
70	U	0.0000000000	0.6666666667	0.6666666667	0	0	0
71	U	0.0000000000	0.6666666667	0.3333333333	0	0	0
72	U	0.0000000000	0.3333333333	0.6666666667	0	0	0
73	U	0.3333333333	0.0000000000	0.3333333333	0	0	0
74	U	0.6666666667	0.0000000000	0.6666666667	0	0	0
75	U	0.3333333333	0.0000000000	0.6666666667	0	0	0
76	U	0.6666666667	0.0000000000	0.3333333333	0	0	0
77	U	0.3333333333	0.3333333333	0.0000000000	0	0	0
78	U	0.6666666667	0.6666666667	0.0000000000	0	0	0
79	U	0.6666666667	0.3333333333	0.0000000000	0	0	0
80	U	0.3333333333	0.6666666667	0.0000000000	0	0	0
81	U	0.151218039	0.506822556	0.548576738			
82	U	0.146390108	0.829542179	0.788362872			
83	U	0.185174494	0.843342696	0.464715498			
84	U	0.143670888	0.494112883	0.870258462			
85	U	0.521448430	0.133334423	0.501328591			
86	U	0.833500163	0.136787016	0.798434778			
87	U	0.495145627	0.121151838	0.844025002			
88	U	0.863545497	0.168786689	0.469156772			
89	U	0.509274324	0.548329765	0.145881356			
90	U	0.825440636	0.779984312	0.192980330			
91	U	0.842423236	0.466015059	0.136756583			
92	U	0.534458472	0.865141497	0.169291879			
93	U	0.310602920	0.323532531	0.315012292			
94	Mo	0.328606490	0.314883686	0.687255302			
95	Mo	0.674009341	0.305267841	0.662448637			
96	U	0.326631011	0.679870122	0.331479707			
97	U	0.371644890	0.679274954	0.665208460			
98	Mo	0.672193000	0.303810812	0.317212538			
99	U	0.820847752	0.816237464	0.833790833			
100	U	0.780071628	0.836705518	0.490628528			
101	U	0.493041587	0.450284430	0.842990907			
102	U	0.818302670	0.476570581	0.798002061			
103	U	0.497363584	0.801441831	0.487806684			
104	U	0.478662001	0.802952159	0.852807185			
105	U	0.852755368	0.505332549	0.451217549			
106	U	0.687902994	0.670557165	0.683653268			
107	Xe	0.536400212	0.492947199	0.459667944			
108	LAST_IMAGE						
109	ATOMIC_POSITIONS (crystal)						
110	U	0.0000000000	0.0000000000	0.0000000000	0	0	0
111	U	0.211003121	0.204403180	0.229059646			
112	U	0.0000000000	0.0000000000	0.3333333333	0	0	0
113	U	0.0000000000	0.0000000000	0.6666666667	0	0	0
114	U	0.3333333333	0.0000000000	0.0000000000	0	0	0

```

115 U 0.666666667 0.000000000 0.000000000 0 0 0
116 U 0.000000000 0.333333333 0.000000000 0 0 0
117 U 0.000000000 0.666666667 0.000000000 0 0 0
118 U 0.137157542 0.154100490 0.530986252
119 U 0.174212597 0.129079723 0.860099413
120 U 0.526361077 0.134914785 0.159501081
121 U 0.862023067 0.133697598 0.175888456
122 U 0.158401680 0.524202200 0.202384340
123 U 0.148244066 0.848143594 0.127034040
124 U 0.000000000 0.333333333 0.333333333 0 0 0
125 U 0.000000000 0.666666667 0.666666667 0 0 0
126 U 0.000000000 0.666666667 0.333333333 0 0 0
127 U 0.000000000 0.333333333 0.666666667 0 0 0
128 U 0.333333333 0.000000000 0.333333333 0 0 0
129 U 0.666666667 0.000000000 0.666666667 0 0 0
130 U 0.333333333 0.000000000 0.666666667 0 0 0
131 U 0.666666667 0.000000000 0.333333333 0 0 0
132 U 0.333333333 0.333333333 0.000000000 0 0 0
133 U 0.666666667 0.666666667 0.000000000 0 0 0
134 U 0.666666667 0.333333333 0.000000000 0 0 0
135 U 0.333333333 0.666666667 0.000000000 0 0 0
136 U 0.178710377 0.490990744 0.516187076
137 U 0.211424168 0.769055779 0.787371675
138 U 0.175042054 0.807911917 0.455992431
139 U 0.138797282 0.465117394 0.842521779
140 U 0.460172734 0.148226288 0.492431541
141 U 0.853214362 0.204001135 0.813615314
142 U 0.517320360 0.155236389 0.808583066
143 U 0.796831649 0.141536092 0.504982369
144 U 0.472082596 0.445170387 0.165199942
145 U 0.797246556 0.819083198 0.205717103
146 U 0.848947010 0.446752941 0.157261389
147 U 0.477337922 0.823974130 0.198045419
148 U 0.357415253 0.358227015 0.377748970
149 Mo 0.316993580 0.314763082 0.680421155
150 Mo 0.607201462 0.351778562 0.642719282
151 U 0.340550068 0.659420403 0.325593019
152 U 0.361166032 0.621614060 0.637522343
153 Mo 0.660553429 0.302407475 0.343460369
154 U 0.864645732 0.824012823 0.866480839
155 U 0.857095779 0.828386743 0.537288219
156 U 0.459295873 0.501704484 0.851504670
157 U 0.787396737 0.503369090 0.850267568
158 U 0.483789070 0.821735869 0.546285283
159 U 0.525937071 0.834449910 0.872642503
160 U 0.803265518 0.439297450 0.559004083
161 U 0.678713059 0.684639768 0.648649342
162 Xe 0.649346200 0.596837093 0.354823657
163 END_POSITIONS
164 K_POINTS automatic
165 4 4 4 0 0 0
166 CELL_PARAMETERS {alat}
167 1.00 0.00 0.00
168 0.00 1.00 0.00
169 0.00 0.00 1.00
170 END_ENGINE_INPUT
171 END

```

E.3.4 QUANTUMESPRESSO with Python.

A sample code to run distorted lattice in QUANTUMESPRESSO with Python. The following code is valid for bcc lattice only.

```

1 #! /usr/bin/python3
2
3 import os, subprocess
4 from glob import glob
5 import re
6 import matplotlib.pyplot as plt
7 import numpy as np
8
9 def matprintf(x):
10     for i in range(len(x)):
11         print ('{:16.13f} {:16.13f} {:16.13f}'.format(x[i][0],x[i]
12             ][1],x[i][2]))
13
14 d = np.array([3.42, 3.43, 3.44, 3.455, 3.45, 3.465, 3.46, 3.475,
15     3.47, 3.48, 3.445, 3.4425])
16 d = np.array(
17     ([0,0.01,-0.01,0.005,-0.005,0.0075,-0.0075,0.00625,-0.00625,0.0025,-0.0025, \
18      0.00375,-0.00375,0.00125,-0.00125,0.02,-0.02]))
19
20
21
22
23
24
25
26
27
28
29
30
31
32
33
34
35
36
37
38
39
40
41
42
43
44
45
46
47
filename = 'U_qepp_gamma.scf'
pseudo = '/home/scruffy/rafi/Desktop/rafi/quantum_espresso/
supercell_study/pp_dir'
with open(filename + str(d[i]) + '.in','w') as f:
    f.write("&control\n")
    f.write("title = 'U_gamma'\n")
    f.write("    calculation = 'relax'\n")
    f.write("    restart_mode = 'from_scratch'\n")
    f.write("    pseudo_dir = '{:s}'\n".format(pseudo))
    f.write("    outdir = '{:s}'\n".format(pseudo))
    f.write("    prefix = 'gammaU'\n")
    f.write("    etot_conv_thr = 1.0e-8\n")
    f.write("    forc_conv_thr = 1.0e-8\n")
    f.write("    tstress = .true.\n")
    f.write("    tprnfor = .true.\n")
    f.write("/\n")
    f.write(" ")
    f.write("&system\n")
    f.write("    ibrav = 0\n")

```

```

48         f.write("      A = 3.459\n")
49 #f.write("      A = {:3.10f}\n" .format(d[i]))
50         f.write("      nat = 1\n")
51         f.write("      ntyp = 1\n")
52         f.write("      ecutwfc = 50 \n")
53         f.write("      ecutrho = 250 \n")
54         f.write("      smearing = 'methfessel-paxton'\n")
55 #f.write("      smearing = 'gauss'\n")
56 #f.write("      degauss = 0.01\n")
57         f.write("/\n")
58         f.write(" ")
59         f.write("&electrons\n")
60         f.write("      diagonalization = 'david'\n")
61 #f.write("      conv_thr = 1.0e-8\n")
62 #f.write("      mixing_beta = 0.7\n")
63         f.write("/\n")
64         f.write(" ")
65         f.write("&IONS\n")
66         f.write("/\n")
67         f.write(" ")
68         f.write("&CELL\n")
69         f.write("/\n")
70         f.write("CELL_PARAMETERS {alat} \n")
71 #f.write(" -0.5    0.5    0.5 \n")
72 #f.write("  0.5   -0.5    0.5 \n")
73 #f.write("  0.5    0.5   -0.5 \n")
74
75     for j in range (len(Rprime)) :
76         f.write ('{:16.13f} {:16.13f} {:16.13f} \n'.format(
Rprime[j][0],Rprime[j][1],Rprime[j][2]))
77
78         f.write(" \n")
79         f.write("ATOMIC_SPECIES\n")
80         f.write("U 238.029 U.GGA-PBE-paw.UPF\n")
81         f.write(" \n")
82         f.write("ATOMIC_POSITIONS {crystal}\n")
83         f.write("U 0.000 0.000 0.000\n")
84         f.write(" \n")
85         f.write("K_POINTS automatic\n")
86         f.write("35 35 35 0 0 0\n")
87         command = ('mpiexec -n 8 pw.x -i ' + filename + str(d[i]) + '.in >
' + filename + str(d[i]) + '.out' )
88         print(command)
89         p = subprocess.Popen(command, shell=True)
90         p.wait()

```

BIBLIOGRAPHY

- B. D. Miller, J. Gan, D. D. Keiser, Jr, A. B. Robinson, J. F. Jue, J. W. Madden, and P. G. Medvedev, *Journal of Nuclear Materials* **458**, 115 (2015)
- B. D. Miller, J. Gan, J. Madden, J.-F. Jue, A. Robinson, and D. D. Keiser, *Journal of Nuclear Materials* **424**, 38 (2012)
- V. A. Rabinovich, A. A. Vasserman, V. I. Nedostup, and L. S. Veksler, *Thermophysical Properties of Neon, Argon, Krypton, and Xenon* (Hemisphere Publishing Corporation, New York, NY, 1987)
- A. R. Kaufmann, *Nuclear Reactor Fuel Elements: Metallurgy and Fabrication* (Interscience Publishers, New York, 1962)
- J. C. Maxwell, *A Treatise on Electricity and Magnetism*, Vol. 1 (Clarendon Press, Oxford, 1881)
- Z. Hashin and S. Shtrikman, *Journal of Applied Physics* **33**, 3125 (1962)
- A. Glaser, in *The 27th International Meeting on Reduced Enrichment for Research and Test Reactors (RERTR)* (Boston, Massachusetts, 2005)
- IAEA, *Management of High Enriched Uranium for Peaceful Purposes: Status and Trends*, TECDOC Series No. 1452 (International Atomic Energy Agency, Vienna, 2005)
- A. H. Montgomery and S. D. Sagan, *Journal of Conflict Resolution* **53**, 302 (2009)
- W. H. Donnelly, *Energy Policy* **8**, 335 (1980)
- R. Serber, *The Los Alamos Primer: The First Lectures on How to Build an Atomic Bomb* (University of California Press, 1992)
- A. Travelli, *Current Status of the RERTR Program*, Tech. Rep. CONF-801144-9/DE83017214 (Argonne National Laboratory, Illinois (USA), 1980)
- J. L. Snelgrove, G. L. Hofman, M. K. Meyer, C. L. Trybus, and T. C. Wienczek, *Nuclear Engineering and Design* **178**, 119 (1997)
- D. E. Burkes, I. J. Schwerdt, T. K. Huber, H. Breitkreutz, C. Reiter, W. Petry, J. L. Schulthess, A. M. Casella, A. J. Casella, E. C. Buck, K. N. Pool, P. J. MacFarlan, M. K. Edwards, and F. N. Smith, *Journal of Nuclear Materials* **547**, 152823 (2021)

- E. Wilson, A. Bergeron, J. Stillman, T. Heltemes, D. Jaluvka, and L. Jamison, in *Proceedings of the 2017 European Research Reactor Conference* (RRFM Rotterdam, Netherlands, 2017)
- National Academies of Sciences, Engineering, and Medicine, *Reducing the Use of Highly Enriched Uranium in Civilian Research Reactors* (National Academies Press, Washington, DC, 2016) pp. 12–19
- National Research Council, *Progress, Challenges, and Opportunities for Converting U.S. and Russian Research Reactors: A Workshop Report* (National Academies Press, Washington, DC, 2012)
- M. K. Meyer, J. Gan, J. F. Jue, D. D. Keiser, E. Perez, A. Robinson, D. M. Wachs, N. Woolstenhulme, G. L. Hofman, and Y. S. Kim, Nuclear Engineering and Technology **46**, 169 (2014)
- S. Pugh, Journal of Nuclear Materials **4**, 177 (1961)
- B. Loomis and D. Pracht, *Swelling of Uranium and Uranium Alloys on Postirradiation Annealing*, Tech. Rep. ANL-6532 (Argonne National Laboratory, Argonne, Illinois, USA, 1962)
- H. H. Chiswik, A. E. Dwight, L. T. Lloyd, M. V. Nevitt, and S. T. Zegler, *Advances in the Physical Metallurgy of Uranium and its Alloys*, Tech. Rep. A/CONF.15/P/713 (Argonne National Laboratory, Lemont, Illinois, USA, 1958)
- K. Farrell, Performance of Aluminum in Research Reactors, in *Comprehensive Nuclear Materials*, Vol. 5, edited by R. J. Konings (Elsevier, Oxford, 2012) Chap. 5, pp. 143–187
- D. W. White, A. P. Beard, and A. H. Willis, *Irradiation Behavior of Dispersion Fuels*, Tech. Rep. KAPL-1909; KAPL-P-1849 (Knolls Atomic Power Laboratory, Schenectady, New York (USA), 1957)
- H. Okamoto, Journal of Phase Equilibria and Diffusion **33**, 489 (2012)
- H. A. Saller, R. F. Dickerson, F. A. Rough, E. L. Foster, A. A. Bauer, and J. R. Lulay, *A Study of Aluminum-Uranium Alloys*, Tech. Rep. BMI-1066 (Battelle Memorial Institute, Columbus, Ohio (USA), 1956)
- L. Sannen, S. van den Berghe, and A. Leenaers, in *6th Forum on New Materials - Part B, Advances in Science and Technology*, Vol. 94 (Trans Tech Publications Ltd, 2014) pp. 43–54
- M. K. Meyer, T. C. Wiencek, S. L. Hayes, and G. L. Hofman, Journal of Nuclear Materials **278**, 358 (2000)
- G. L. Hofman, R. F. Domagala, and G. L. Copeland, Journal of Nuclear Materials **150**, 238 (1987)

- S. van den Berghe, A. Leenaers, E. Koonen, and L. Sannen, in *Advances in Science and Technology*, Vol. 73 (Trans Tech Publications Ltd, 2011) pp. 78–90
- G. Donzé and G. Cabane, *Journal of Nuclear Materials* **1**, 364 (1959)
- F. Giraud-Heraud and J. Guillaumin, *Acta Metallurgica* **21**, 1243 (1973)
- D. A. Lopes, T. A. G. Restivo, and A. F. Padilha, *Journal of Nuclear Materials* **440**, 304 (2013)
- H. A. Saller, F. Rough, and A. Bauer, *Transformation Kinetics of Uranium-Molybdenum Alloys*, Tech. Rep. BMI-957 (Battelle Memorial Institute, Columbus, Ohio (USA), 1954)
- W. A. Bostrom and E. K. Haltzman, *The Metastable Gamma Phase in Uranium Base Molybdenum Alloys*, Tech. Rep. WAPD-T-415 (Westinghouse Electric Corporation, Bettis Plant, Pittsburgh (USA), 1956)
- R. Prabhakaran, *JOM* **69**, 2529 (2017)
- W. Williams, A. Robinson, and B. Rabin, *JOM* **69**, 2546 (2017)
- H. Okamoto, *Journal of Phase Equilibria and Diffusion* **33**, 497 (2012)
- T. F. Wimett, *Fast Burst Reactors in the USA*, Tech. Rep. LA-DC-6786; SM-62/53; CONF-650 (Los Alamos Scientific Laboratory, Los Alamos, New Mexico (USA), 1965)
- J. Mihalczo, *Static and Dynamic Measurements with the Army Pulse Radiation Facility Reactor*, Tech. Rep. ORNL-TM-2330 (Oak Ridge National Laboratory, Tennessee (USA), 1969)
- L. Bonzon and J. Snyder, *Sandia Pulsed Reactor II (SPR II): Experimenter's Manual*, Tech. Rep. SLA-73-551 (Sandia Laboratories, Albuquerque, New Mexico(USA), 1973)
- J. A. Horak, J. A. Reuscher, and D. J. Sasmor, *Operating Experience with Uranium-Molybdenum Fuel in Pulsed Reactors*, Tech. Rep. SLA-73-5559; CONF-730801-5 (Sandia Laboratories, Albuquerque, New Mexico(USA), 1973)
- R. Matthews, J. Phillips, K. Henry, R. Allardice, D. Donaldson, and H. Tilbe, *Performance and operation of the Dounreay fast reactor*, Tech. Rep. A/CONF.28/P/130 (United Kingdom Atomic Energy Authority, Caithness, Scotland (United Kingdom), 1964)
- S. A. Cottrell, E. Edmonds, P. Higginson, and W. Oldfield, *Development and Performance of Dounreay Fast Reactor Metal Fuel*, Tech. Rep. A/CONF.28/P/150 (United Kingdom Atomic Energy Authority. Industrial Group. Dounreay, 1964)

IAEA, *Development Status of Metallic, Dispersion and Non-Oxide Advanced and Alternative Fuels for Power and Research Reactors*, TECDOC Series No. 1374 (International Atomic Energy Agency, Vienna, 2003)

- A. Leenaers, S. Van den Berghe, E. Koonen, C. Jarousse, F. Huet, M. Trotabas, M. Boyard, S. Guillot, L. Sannen, and M. Verwerft, *Journal of Nuclear Materials* **335**, 39 (2004)
- J.-F. Jue, D. D. Keiser, C. R. Breckenridge, G. A. Moore, and M. K. Meyer, *Journal of Nuclear Materials* **448**, 250 (2014)
- S. Van den Berghe, W. Van Renterghem, and A. Leenaers, *Journal of Nuclear Materials* **375**, 340 (2008)
- D. Olander, *Journal of Nuclear Materials* **383**, 201 (2009)
- A. Guay, *Uranium Swelling in N-Reactor (PT-NR-4, Sup. A, Report No. 1)*, Tech. Rep. RL-NRD-550 (General Electric, Hanford Atomic Products, Richland, Washington (USA), 1965)
- J. Gan, D. D. Keiser, D. M. Wachs, A. B. Robinson, B. D. Miller, and T. R. Allen, *Journal of Nuclear Materials* **396**, 234 (2010)
- D. R. Hartree, in *Proceedings of the Cambridge Philosophical Society*, Vol. 24 (Cambridge University Press, 1928) p. 89
- V. Fock, *Zeitschrift für Physik* **61**, 126 (1930)
- L. H. Thomas, in *Proceedings of the Cambridge Philosophical Society*, Vol. 23 (Cambridge University Press, 1927) pp. 542–548
- E. Fermi, *Rend. Accad. Naz. Lincei* **6**, 602 (1927)
- P. Hohenberg and W. Kohn, *Physical Review* **136**, B864 (1964)
- C. Herring, *Physical Review* **57**, 1169 (1940)
- J. C. Phillips and L. Kleinman, *Physical Review* **116**, 287 (1959)
- D. R. Hamann, M. Schlüter, and C. Chiang, *Physical Review Letters* **43**, 1494 (1979)
- N. Troullier and J. L. Martins, *Physical Review B: Condensed Matter and Materials Physics* **43**, 1993 (1991)
- D. Vanderbilt, *Physical Review B: Condensed Matter and Materials Physics* **41**, 7892 (1990)
- G. Kresse and D. Joubert, *Physical Review B: Condensed Matter and Materials Physics* **59**, 1758 (1999)

- P. E. Blöchl, Physical Review B: Condensed Matter and Materials Physics **50**, 17953 (1994)
- J. H. Kittel, B. R. T. Frost, J. P. Mustelier, K. Q. Bagley, G. C. Crittenden, and J. Van Dievoet, Journal of Nuclear Materials **204**, 1 (1993)
- H. Okamoto, M. E. Schlesinger, and E. M. Mueller, eds., Mo (molybdenum) binary alloy phase diagrams, in *Alloy Phase Diagrams*, ASM Handbook, Vol. 3 (ASM International, 2016) pp. 489–498
- A. Berche, N. Dupin, C. Guénau, C. Rado, B. Sundman, and J. C. Dumas, Journal of Nuclear Materials **411**, 131 (2011)
- D. D. Keiser, J.-F. Jue, A. B. Robinson, P. Medvedev, J. Gan, B. D. Miller, D. M. Wachs, G. A. Moore, C. R. Clark, M. K. Meyer, and M. R. Finlay, Journal of Nuclear Materials **425**, 156 (2012)
- G. L. Hofman, M. R. Finlay, and Y. S. Kim, in *Proceedings of the 26th International Meeting on Reduced Enrichment for Research and Test Reactors (RERTR)* (Vienna, Austria, 2004) pp. 7–12
- D. E. Burkes, A. M. Casella, A. J. Casella, E. C. Buck, K. N. Pool, P. J. MacFarlan, M. K. Edwards, and F. N. Smith, Journal of Nuclear Materials **464**, 331 (2015)
- V. V. Rondinella and T. Wiss, Materials Today **13**, 24 (2010)
- S. Ishimoto, M. Hirai, K. Ito, and Y. Korei, Journal of Nuclear Science and Technology **31**, 796 (1994)
- K. Kang, K. Song, S. Lee, and S. Kim, International Journal of Thermophysics **28**, 2188 (2007)
- J. Gan, D. Keiser, B. Miller, A. Robinson, D. Wachs, and M. Meyer, Journal of Nuclear Materials **464**, 1 (2015)
- A. Blades, W. Fleming, and H. Thode, Canadian Journal of Chemistry **34**, 233 (1956)
- J. Petruska, H. Thode, and R. Tomlinson, Canadian Journal of Physics **33**, 693 (1955)
- Y. S. Kim and G. L. Hofman, Journal of Nuclear Materials **419**, 291 (2011)
- J. Gan, D. D. Keiser, B. D. Miller, A. B. Robinson, J.-F. Jue, P. Medvedev, and D. M. Wachs, Journal of Nuclear Materials **424**, 43 (2012)
- P. B. Johnson and D. J. Mazey, Journal of Nuclear Materials **93–94**, 721 (1980)
- P. B. Johnson and D. J. Mazey, Journal of Nuclear Materials **91**, 41 (1980)

- J. H. Evans, Journal of Nuclear Materials **119**, 180 (1983)
- D. J. Mazey and J. H. Evans, Journal of Nuclear Materials **138**, 16 (1986)
- J. H. Evans and D. J. Mazey, Journal of Nuclear Materials **138**, 176 (1986)
- P. B. Johnson, K. J. Stevens, and R. W. Thomson, Nuclear Instruments and Methods in Physics Research Section B: Beam Interactions with Materials and Atoms **62**, 218 (1991)
- P. B. Johnson and D. J. Mazey, Journal of Nuclear Materials **218**, 273 (1995)
- F. E. Lawson and P. B. Johnson, Journal of Nuclear Materials **252**, 34 (1998)
- N. M. Ghoniem, D. Walgraef, and S. J. Zinkle, Journal of Computer-Aided Materials Design **8**, 1 (2001)
- P. B. Johnson and F. Lawson, Nuclear Instruments and Methods in Physics Research Section B: Beam Interactions with Materials and Atoms **243**, 325 (2006)
- J. Gan, D. D. Keiser, Jr., B. D. Miller, A. B. Robinson, D. M. Wachs, and M. K. Meyer, Journal of Nuclear Materials **464**, 1 (2015)
- K. Bakker, International Journal of Heat and Mass Transfer **40**, 3503 (1997)
- J. B. MacEwan, R. L. Stoute, and M. J. F. Notley, Journal of Nuclear Materials **24**, 109 (1967)
- L. A. Goldsmith and J. A. M. Douglas, Journal of Nuclear Materials **47**, 31 (1973)
- M. F. DeVries, Journal of Heat Transfer **111**, 281 (1989)
- A. L. Loeb, Journal of the American Ceramic Society **37**, 96 (1954)
- M. E. Cunningham and K. L. Peddicord, International Journal of Heat and Mass Transfer **24**, 1081 (1981)
- D. Y. Tzou, International Journal of Heat and Mass Transfer **34**, 1839 (1991)
- T. H. Bauer, International Journal of Heat and Mass Transfer **36**, 4181 (1993)
- S. Hu, A. M. Casella, C. A. Lavender, D. J. Senor, and D. E. Burkes, Journal of Nuclear Materials **462**, 64 (2015)
- Trellis Pro (csimsoft, LLC., American Fork, Utah, 2012–2017)
- D. E. Burkes, C. A. Papesch, A. P. Maddison, T. Hartmann, and F. J. Rice, Journal of Nuclear Materials **403**, 160 (2010)
- G. W. Greenwood, A. J. E. Foreman, and D. E. Rimmer, Journal of Nuclear Materials **1**, 305 (1959)

- H. Trinkaus, *Radiation Effects* **78**, 189 (1983)
- H. Xiao, C. Long, X. Tian, and S. Li, *Materials and Design* **74**, 55 (2015)
- L. E. Thomas, in *Fundamental Aspects of Inert Gases in Solids* (Springer, New York, 1991) pp. 431–441
- M. Ross and A. K. McMahan, *Physical Review B: Condensed Matter and Materials Physics* **21**, 1658 (1980)
- J. Zheng, Q. F. Chen, Y. J. Gu, Z. Y. Chen, and C. J. Li, *Journal of Chemical Physics* **141**, 124 (2014)
- C. Wilke, *Journal of Chemical Physics* **18**, 517 (1950)
- W. G. Vincenti and C. H. Kruger, *Introduction to Physical Gas Dynamics* (John Wiley and Sons, New York, 1965)
- H. Alkandry, I. Boyd, and A. Martin, in *51st AIAA Aerospace Sciences Meeting including the New Horizons Forum and Aerospace Exposition* (2013) p. 303
- D. Gaston, C. Newman, G. Hansen, and D. Lebrun-Grandie, *Nuclear Engineering and Design* **239**, 1768 (2009)
- C. R. Clark, G. C. Knighton, M. K. Meyer, and G. L. Hofman, in *2003 International Meeting on Reduced Enrichment for Research and Test Reactors*, Vol. 1 (Chicago, Illinois, 2003)
- D. S. Smith, A. Alzina, J. Bourret, B. Nait-Ali, F. Pennec, N. Tessier-Doyen, K. Otsu, H. Matsubara, P. Elser, and U. T. Gonzenbach, *Journal of Materials Research* **28**, 2260 (2013)
- B. Schulz, *High Temperatures – High Pressures* **13**, 649 (1981)
- Y. S. Kim, G. Hofman, and J. Cheon, *Journal of Nuclear Materials* **436**, 14 (2013)
- T. H. Bauer and J. W. Holland, *Nuclear Technology* **110**, 407 (1995)
- K. L. Peddicord, M. E. Cunningham, and A. Tripathi, *Transactions of the American Nuclear Society* **28**, 548 (1978)
- K. Bakker, H. Kwast, and E. H. P. Cordfunke, *Journal of Nuclear Materials* **226**, 128 (1995)
- P. Söderlind, O. Eriksson, B. Johansson, J. M. Wills, and A. M. Boring, *Nature* **374**, 524 (1995)
- A. C. Lawson, C. E. Olsen, J. W. Richardson, M. H. Mueller, and G. H. Lander, *Acta Crystallographica B: Structural Science* **44**, 89 (1988)

- J. Akella, S. Weir, J. M. Wills, and P. Söderlind, *Journal of Physics: Condensed Matter* **9**, L549 (1997)
- G. H. Lander, *Science* **301**, 1057 (2003)
- A. J. Freeman and G. H. Lander, *Handbook on the Physics and Chemistry of the Actinides*, Vol. 1,2 (North-Holland, Amsterdam, 1984)
- J. M. Wills and O. Eriksson, *Physical Review B: Condensed Matter and Materials Physics* **45**, 13879 (1992)
- O. Eriksson, P. Söderlind, J. M. Wills, and A. M. Boring, *Physica C: Superconductivity* **190**, 5 (1993)
- P. Söderlind, O. Eriksson, B. Johansson, and J. M. Wills, *Physical Review B: Condensed Matter and Materials Physics* **50**, 7291 (1994)
- J. P. Crocombette, F. Jollet, L. Thien Nga, and T. Petit, *Physical Review B: Condensed Matter and Materials Physics* **64**, 104107 (2001)
- P. Söderlind, *Physical Review B: Condensed Matter and Materials Physics* **66**, 085113 (2002)
- A. C. Lawson, B. Martinez, J. A. Roberts, B. I. Bennett, and J. W. Richardson, Jr., *Philosophical Magazine B* **80**, 53 (2000)
- M. D. Jones, J. C. Boettger, R. C. Albers, and D. J. Singh, *Physical Review B: Condensed Matter and Materials Physics* **61**, 4644 (2000)
- C. D. Taylor, *Physical Review B: Condensed Matter and Materials Physics* **77**, 094119 (2008)
- P. E. Blöchl, *Physical Review B: Condensed Matter and Materials Physics* **50**, 17953 (1994)
- J. P. Perdew, J. A. Chevary, S. H. Vosko, K. A. Jackson, M. R. Pederson, D. J. Singh, and C. Fiolhais, *Physical Review B: Condensed Matter and Materials Physics* **46**, 6671 (1992)
- J. P. Perdew, J. A. Chevary, S. H. Vosko, K. A. Jackson, M. R. Pederson, D. J. Singh, and C. Fiolhais, *Physical Review B: Condensed Matter and Materials Physics* **48**, 4978 (1993)
- C. S. Barrett, M. H. Mueller, and R. L. Hitterman, *Physical Review* **129**, 625 (1963)
- S. Xiang, H. Huang, and L. Hsiung, *Journal of Nuclear Materials* **375**, 113 (2008)
- J. P. Perdew, K. Burke, and M. Ernzerhof, *Physical Review Letters* **77**, 3865 (1996)
- J. P. Perdew, K. Burke, and M. Ernzerhof, *Physical Review Letters* **78**, 1396 (1997)

- J. H. Li, Q. B. Ren, C. H. Lu, L. Lu, Y. Dai, and B. X. Liu, *Journal of Alloys and Compounds* **516**, 139 (2012)
- J. P. Perdew and Y. Wang, *Physical Review B: Condensed Matter and Materials Physics* **45**, 13244 (1992)
- B. Beeler, C. Deo, M. Baskes, and M. Okuniewski, *Journal of Nuclear Materials* **433**, 143 (2013)
- QUANTUM ESPRESSO, PS library,
<http://www.quantum-espresso.org/pseudopotentials> (2019)
- A. Dal Corso, *Computational Materials Science* **95**, 337 (2014)
- P. Giannozzi, S. Baroni, N. Bonini, M. Calandra, R. Car, C. Cavazzoni, D. Ceresoli, G. L. Chiarotti, M. Cococcioni, I. Dabo, A. Dal Corso, S. de Gironcoli, S. Fabris, G. Fratesi, R. Gebauer, U. Gerstmann, C. Gougaussis, A. Kokalj, M. Lazzeri, L. Martin-Samos, N. Marzari, F. Mauri, R. Mazzarello, S. Paolini, A. Pasquarello, L. Paulatto, C. Sbraccia, S. Scandolo, G. Sclauzero, A. P. Seitsonen, A. Smogunov, P. Umari, and R. M. Wentzcovitch, *Journal of Physics: Condensed Matter* **21**, 395502 (2009), <http://www.quantum-espresso.org/>
- N. A. W. Holzwarth, A. R. Tackett, and G. E. Matthews, *Computer Physics Communications* **135**, 329 (2001)
- A. R. Tackett, N. A. W. Holzwarth, and G. E. Matthews, *Computer Physics Communications* **135**, 348 (2001)
- P. Söderlind, B. Sadigh, V. Lordi, A. Landa, and P. E. A. Turchi, *Journal of Nuclear Materials* **444**, 356 (2014)
- N. Iché-Tarrat and C. J. Marsden, *Journal of Physical Chemistry A* **112**, 7632 (2008)
- A. M. Rappe, K. M. Rabe, E. Kaxiras, and J. D. Joannopoulos, *Physical Review B: Condensed Matter and Materials Physics* **41**, 1227 (1990)
- Naval Research Laboratories, Structure of Crystals, <http://aflowlib.duke.edu/users/egossett/lattice/> (2015)
- H. J. Monkhorst and J. D. Pack, *Physical Review B: Condensed Matter and Materials Physics* **13**, 5188 (1976)
- M. Methfessel and A. T. Paxton, *Physical Review B: Condensed Matter and Materials Physics* **40**, 3616 (1989)
- P. Ravindran, L. Fast, P. A. Korzhavyi, B. Johansson, J. Wills, and O. Eriksson, *Journal of Applied Physics* **84**, 4891 (1998)
- O. Beckstein, J. E. Klepeis, G. L. W. Hart, and O. Pankratov, *Physical Review B: Condensed Matter and Materials Physics* **63**, 134112 (2001)

- G. H. Lander, E. S. Fisher, and S. D. Bader, *Advances in Physics* **43**, 1 (1994)
- T. Le Bihan, S. Heathman, M. Idiri, G. H. Lander, J. M. Wills, A. C. Lawson, and A. Lindbaum, *Physical Review B: Condensed Matter and Materials Physics* **67**, 134102 (2003)
- G. Kresse and J. Hafner, *Physical Review B: Condensed Matter and Materials Physics* **47**, 558 (1993)
- G. Kresse and J. Furthmüller, *Computational Materials Science* **6**, 15 (1996)
- G. Kresse and J. Furthmüller, *Physical Review B: Condensed Matter and Materials Physics* **54**, 11169 (1996)
- F. D. Murnaghan, *Proceedings of the National Academy of Sciences of the United States of America* **30**, 244 (1944)
- R. Q. Hood, L. H. Yang, and J. A. Moriarty, *Physical Review B: Condensed Matter and Materials Physics* **78**, 024116 (2008)
- C.-S. Yoo, H. Cynn, and P. Söderlind, *Physical Review B: Condensed Matter and Materials Physics* **57**, 10359 (1998)
- E. S. Fisher and H. J. McSkimin, *Journal of Applied Physics* **29**, 1473 (1958)
- A. S. Wilson and R. E. Rundle, *Acta Crystallographica* **2**, 126 (1949)
- H. L. Yakel, *Review of X-ray Diffraction Studies in Uranium Alloys*, Tech. Rep. CONF-740205-9 (Oak Ridge National Laboratory, 1973)
- I. Grenthe, J. Drozdynski, T. Fujino, E. C. Buck, T. E. Albrecht-Schmitt, and S. F. Wolf, *The Chemistry of the Actinide and Transactinide Elements*, Vol. 1 (Springer, Dordrecht, 2006) pp. 253–698
- N.-T. H. Kim-Ngan and L. Havela, *Journal of Science: Advanced Materials and Devices* **1**, 121 (2016)
- M. Born, *Proceedings of the Cambridge Philosophical Society* **36**, 160 (1940)
- M. Born and K. Huang, *Dynamical Theory of Crystal Lattices* (Clarendon Press, 1954)
- F. Mouhat and F.-X. Coudert, *Physical Review B: Condensed Matter and Materials Physics* **90**, 224104 (2014)
- P. Söderlind, *Advances in Physics* **47**, 959 (1998)
- C. W. Tucker, Jr., *An Approximate Crystal Structure for the Beta Phase of Uranium*, Tech. Rep. KAPL-388 (Knolls Atomic Power Laboratory, 1950)
- C. W. Tucker, *Acta Crystallographica* **4**, 425 (1951)

- J. Donohue and H. Einspahr, *Acta Crystallographica B: Structural Science* **27**, 1740 (1971)
- J. Donohue, *Structures of the Elements* (John Wiley and Sons, New York, 1974) pp. 134–148
- D. C. Wallace, *Thermodynamics of Crystals* (Courier Corporation, 1998)
- A. R. M. Iasir and K. D. Hammond, *Computational Materials Science* **171**, 109221 (2020)
- V. P. Sinha, P. V. Hegde, G. J. Prasad, G. K. Dey, and H. S. Kamath, *Journal of Alloys and Compounds* **506**, 253 (2010)
- H. L. Yakel, *Journal of Nuclear Materials* **33**, 286 (1969)
- V. P. Sinha, P. V. Hegde, G. J. Prasad, G. K. Dey, and H. S. Kamath, *Journal of Alloys and Compounds* **491**, 753 (2010)
- A. E. Dwight, *Journal of Nuclear Materials* **2**, 81 (1960)
- K. Tangri and G. Williams, *Journal of Nuclear Materials* **4**, 226 (1961)
- A. Berche, N. Dupin, C. Guéneau, C. Rado, B. Sundman, and J. C. Dumas, *Journal of Nuclear Materials* **411**, 131 (2011)
- X. Zhang, Y. F. Cui, G. L. Xu, W. J. Zhu, H. S. Liu, B. Y. Yin, and Z. P. Jin, *Journal of Nuclear Materials* **402**, 15 (2010)
- E. L. Losada and J. E. Garcés, *Journal of Nuclear Materials* **518**, 380 (2019)
- A. Landa, P. Söderlind, and P. E. A. Turchi, *Journal of Nuclear Materials* **414**, 132 (2011)
- P. R. Alonso and G. H. Rubiolo, *Modelling and Simulation in Materials Science and Engineering* **15**, 263 (2007)
- A. Castellano, F. Bottin, B. Dorado, and J. Bouchet, *Physical Review B: Condensed Matter and Materials Physics* **101**, 184111 (2020)
- A. R. M. Iasir, N. J. Peters, and K. D. Hammond, *Journal of Nuclear Materials* **508**, 159 (2018)
- J. Rest, Y. S. Kim, G. L. Hofman, M. K. Meyer, and S. L. Hayes, *U-Mo Fuels Handbook. Version 1.0*, Tech. Rep. ANL-09/31 (Argonne National Lab. (ANL), Argonne, IL (United States), 2006)
- R. W. Grimes and C. R. A. Catlow, *Philosophical Transactions of the Royal Society A: Mathematical, Physical, and Engineering Sciences* **335**, 609 (1991)

- D. A. Andersson, B. P. Uberuaga, P. V. Nerikar, C. Unal, and C. R. Stanek, Physical Review B: Condensed Matter and Materials Physics **84**, 054105 (2011)
- Y. Yun, H. Kim, H. Kim, and K. Park, Journal of Nuclear Materials **378**, 40 (2008)
- J. C. Carter, E. J. Driscoll, and T. S. Elleman, Physica Status Solidi A: Applications and Materials Science **14**, 673 (1972)
- H. Matzke, Nuclear Applications **2**, 131 (1966)
- J. R. MacEwan and W. H. Stevens, Journal of Nuclear Materials **11**, 77 (1964)
- K. Une, I. Tanabe, and M. Oguma, Journal of Nuclear Materials **150**, 93 (1987)
- C. R. A. Catlow, Proceedings of the Royal Society of London Series A, Mathematical and Physical Sciences **364**, 473 (1978)
- R. A. Jackson, A. D. Murray, J. H. Harding, and C. R. A. Catlow, Philosophical Magazine A **53**, 27 (1986)
- R. W. Grimes, C. R. A. Catlow, and A. M. Stoneham, Journal of the American Ceramic Society **72**, 1856 (1989)
- R. G. J. Ball and R. W. Grimes, Journal of the Chemical Society, Faraday Transactions **86**, 1257 (1990)
- T. Petit, G. Jomard, C. Lemaignan, B. Bigot, and A. Pasturel, Journal of Nuclear Materials **275**, 119 (1999)
- J.-P. Crocombette, Journal of Nuclear Materials **305**, 29 (2002)
- M. Freyss, N. Vergnet, and T. Petit, Journal of Nuclear Materials **352**, 144 (2006)
- G. Neumann and C. Tuijn, *Self-Diffusion and Impurity Diffusion in Pure Metals: Handbook of Experimental Data* (Elsevier, 2008) Chap. 10, pp. 333–348
- A. Paul and S. Divinski, *Handbook of Solid State Diffusion: Volume 2: Diffusion Analysis in Material Applications* (Elsevier, 2017) Chap. 8, pp. 339–372
- H. Matzke, Diffusion processes in nuclear fuels, in *Diffusion Processes in Nuclear Materials*, edited by R. P. Agarwala (North-Holland, 1992) pp. 9–69
- Y. Adda and A. Kirianenko, Journal of Nuclear Materials **1**, 120 (1959)
- N. L. Peterson and S. J. Rothman, Physical Review **136**, A842 (1964)
- S. J. Rothman, L. T. Lloyd, R. Weil, and A. L. Harkness, *Self-Diffusion in gamma Uranium*, Tech. Rep. ANL-5971 (Argonne National Lab., Lemont, Ill., 1959)
- S. J. Rothman, Journal of Nuclear Materials **3**, 77 (1961)

- Y. Adda and A. Kirianenko, Journal of Nuclear Materials **6**, 130 (1962)
- R. Resnick and L. L. Seigle, Journal of Nuclear Materials **5**, 5 (1962)
- S. J. Rothman, J. Gray, Jr, J. P. Hughes, and A. L. Harkness, Journal of Nuclear Materials **3**, 72 (1961)
- Y. Liu, D. Yu, Y. Du, G. Sheng, Z. Long, J. Wang, and L. Zhang, Calphad **37**, 49 (2012)
- D. E. Smirnova, A. Y. Kuksin, S. V. Starikov, and V. V. Stegailov, Physics of Metals and Metallography **116**, 445 (2015)
- J. B. Adams, S. M. Foiles, and W. G. Wolfer, Journal of Materials Research **4**, 102 (1989)
- P. E. Blöchl, E. Smargiassi, R. Car, D. B. Laks, W. Andreoni, and S. T. Pantelides, Physical Review Letters **70**, 2435 (1993)
- P. E. Blöchl, C. G. Van de Walle, and S. T. Pantelides, Physical Review Letters **64**, 1401 (1990)
- W. Frank, U. Breier, C. Elsässer, and M. Fähnle, Physical Review Letters **77**, 518 (1996)
- A. Janotti, M. Krčmar, C. L. Fu, and R. C. Reed, Physical Review Letters **92**, 085901 (2004)
- M. Krčmar, C. L. Fu, A. Janotti, and R. C. Reed, Acta Materialia **53**, 2369 (2005)
- V. Milman, M. C. Payne, V. Heine, R. J. Needs, J. S. Lin, and M. H. Lee, Physical Review Letters **70**, 2928 (1993)
- N. Sandberg, B. Magyari-Köpe, and T. R. Mattsson, Physical Review Letters **89**, 065901 (2002)
- A. B. Lidiard, Philosophical Magazine Series 7 **46**, 1218 (1955)
- A. B. Lidiard, Philosophical Magazine A **5**, 1171 (1960)
- A. D. Leclaire and A. B. Lidiard, Philosophical Magazine A **1**, 518 (1956)
- A. D. Le Claire, Philosophical Magazine A **21**, 819 (1970)
- H. Mehrer, *Diffusion in Solids: Fundamentals, Methods, Materials, Diffusion-Controlled Processes*, Vol. 155 (Springer Science & Business Media, 2007) pp. 116–122
- G. H. Vineyard and G. J. Dienes, Physical Review **93**, 265 (1954)
- G. H. Vineyard, Journal of Physics and Chemistry of Solids **3**, 121 (1957)

- H. Eyring, *Journal of Chemical Physics* **3**, 107 (1935)
- M. G. Evans and M. Polanyi, *Transactions of the Faraday Society* **31**, 875 (1935)
- K. Heinola and T. Ahlgren, *Journal of Applied Physics* **107**, 113531 (2010)
- R. W. Balluffi and P. S. Ho, *Diffusion* (American Society for Metals, Metals Park, Ohio, 1973) p. 83
- C. Wolverton, *Acta Materialia* **55**, 5867 (2007)
- P. Soderlind, *Advances in Physics* **47**, 959 (1998)
- Y.-Y. Ye, Y. Chen, K.-M. Ho, B. N. Harmon, and P.-A. Lindgård, *Physical Review Letters* **58**, 1769 (1987)
- J. M. Sanchez and D. De Fontaine, *Physical Review Letters* **35**, 227 (1975)
- B. Beeler, B. Good, S. Rashkeev, C. Deo, M. Baskes, and M. Okuniewski, *Journal of Physics: Condensed Matter* **22**, 505703 (2010)
- G. Henkelman, B. P. Uberuaga, and H. Jónsson, *Journal of Chemical Physics* **113**, 9901 (2000)
- G. Henkelman and H. Jónsson, *Journal of Chemical Physics* **113**, 9978 (2000)
- H. Matter, J. Winter, and W. Triftshäuser, *Journal of Nuclear Materials* **88**, 273 (1980)
- K. R. Lund, K. G. Lynn, M. H. Weber, and M. A. Okuniewski, *Journal of Physics: Conference Series* **443**, 012021 (2013)
- P. Olsson, T. P. C. Klaver, and C. Domain, *Physical Review B: Condensed Matter and Materials Physics* **81**, 054102 (2010)
- T. Ohnuma, N. Soneda, and M. Iwasawa, *Acta Materialia* **57**, 5947 (2009)
- E. Vincent, C. Becquart, and C. Domain, *Nuclear Instruments and Methods in Physics Research Section B: Beam Interactions with Materials and Atoms* **228**, 137 (2005)
- X.-S. Kong, X. Wu, Y.-W. You, C. Liu, Q. Fang, J.-L. Chen, G.-N. Luo, and Z. Wang, *Acta Materialia* **66**, 172 (2014)
- J. Burke, *Journal of the Less-Common Metals* **28**, 441 (1972)
- M. G. Bell, H. W. Kugel, R. Kaita, L. E. Zakharov, H. Schneider, B. P. LeBlanc, D. Mansfield, R. E. Bell, R. Maingi, S. Ding, S. M. Kaye, S. F. Paul, S. P. Gerhardt, J. M. Canik, J. C. Hosea, G. Taylor, and the NSTX Research Team, *Plasma Physics and Controlled Fusion* **51**, 124054 (2009)

- S. V. Mirnov, V. B. Lazarev, S. M. Sotnikov, T-11M Team, V. A. Evtikhin, I. E. Lyublinski, and A. V. Vertkov, *Fusion Engineering and Design* **65**, 455 (2003)
- J. Sánchez, F. L. Tabarés, D. Tafalla, J. A. Ferreira, I. García-Cortés, C. Hidalgo, F. Medina, M. A. Ochando, M. A. Pedrosa, and The TJ-II Team, *Journal of Nuclear Materials* **390**, 852 (2009)
- A. Tuccillo, A. Alekseyev, B. Angelini, S. Annibaldi, M. Apicella, G. Apruzzese, J. Berrino, E. Barbato, A. Bertocchi, A. Biancalani, W. Bin, A. Botrugno, G. Bracco, S. Briguglio, A. Bruschi, P. Buratti, G. Calabro, A. Cardinali, C. Castaldo, C. Centioli, R. Cesario, L. Chen, S. Cirant, V. Cocilovo, F. Crisanti, R. D. Angelis, U. de Angelis, L. D. Matteo, C. D. Troia, B. Esposito, G. Fogaccia, D. Frigione, L. Gabellieri, F. Gandini, E. Giovannozzi, G. Granucci, F. Gravanti, G. Grossetti, G. Grossi, F. Iannone, H. Kroegler, V. Lazarev, E. Lazzaro, I. Lyublinski, G. Maddaluno, M. Marinucci, D. Marocco, J. Martin-Solis, G. Mazzitelli, C. Mazzotta, V. Mellera, F. Mirizzi, S. Mirnov, G. Monari, A. Moro, V. Muzzini, S. Nowak, F. Orsitto, L. Panaccione, D. Pacella, M. Panella, F. Pegoraro, V. Pericoli-Ridolfini, S. Podda, S. Ratynskaia, G. Ravera, A. Romano, A. Rufoloni, A. Simonetto, P. Smeulders, C. Sozzi, E. Sternini, B. Tilia, O. Tudisco, A. Vertkov, V. Vitale, G. Vlad, R. Zagórski, M. Zerbini, and F. Zonca, *Nucl. Fusion* **49**, 104013 (2009)
- G. Xu, B. Wan, J. Li, X. Gong, J. Hu, J. Shan, H. Li, D. Mansfield, D. Humphreys, V. Naulin, and East team and international collaborators, *Nucl. Fusion* **51**, 072001 (2011)
- S. Munaretto, S. D. Bello, P. Innocente, M. Agostini, F. Auriemma, S. Barison, A. Canton, L. Carraro, G. D. Masi, S. Fiameni, P. Scarin, and D. Terranova, *Nucl. Fusion* **52**, 023012 (2012)
- J. P. Allain and C. N. Taylor, *Physics of Plasmas* **19**, 056126 (2012)
- S. Erents, G. McCracken, and P. Goldsmith, *Journal of Physics D: Applied Physics* **4**, 672 (1971)
- J. Hartley, B. Gore, and J. Young, *Lithium Needs and Resources* , 337 (1978)
- C. E. Kessel, D. Andruczyk, J. P. Blanchard, T. Bohm, A. Davis, K. Hollis, P. W. Humrickhouse, M. Hvasta, M. Jaworski, J. Jun, Y. Katoh, A. Khodak, J. Klein, E. Kolemen, G. Larsen, R. Majeski, B. J. Merrill, N. B. Morley, G. H. Neilson, B. Pint, M. E. Rensink, T. D. Rognlien, A. F. Rowcliffe, S. Smolentsev, M. S. Tillack, L. M. Waganer, G. M. Wallace, P. Wilson, and S.-J. Yoon, *Fusion Science and Technology* **75**, 886 (2019)
- K. D. Hammond, *Materials Research Express* **4**, 104002 (2017)
- H. Jónsson, G. Mills, and K. W. Jacobsen, in *Classical and Quantum Dynamics in Condensed Phase Simulations*, edited by B. J. Berne, G. Ciccotti, and D. F. Coker (World Scientific, Singapore, 1998) Chap. 16, pp. 385–405

- R. Benedek, L. Yang, C. Woodward, and B. Min, Physical Review B: Condensed Matter and Materials Physics **45**, 2607 (1992)
- R. Pawellek, M. Fahnle, C. Elsasser, K. M. Ho, and C. T. Chan, Journal of Physics: Condensed Matter **3**, 2451 (1991)
- W. Frank, U. Breier, C. Elsässer, and M. Fähnle, Physical Review B: Condensed Matter and Materials Physics **48**, 7676 (1993)
- P. Ma and S. Dudarev, Physical Review Materials **3**, 063601 (2019)
- P. Ma and S. L. Dudarev, Physical Review Materials **3**, 013605 (2019)
- P. Ehrnhar, P. Jung, H. Schultz, and H. Ullmaier, in *Atomic Defects in Metals*, Vol. 25, edited by H. Ullmaier (Springer-Verlag Berlin Heidelberg, 1991)
- C. S. Becquart and C. Domain, Physical Review Letters **97**, 196402 (2006)
- T. Seletskaia, Y. Ossetsky, R. E. Stoller, and G. M. Stocks, Physical Review Letters **94**, 046403 (2005)
- K. D. Hammond, D. Maroudas, and B. D. Wirth, Scientific Reports **10**, 2192 (2020)
- M. Samaras, Materials Today **12**, 46 (2009)
- C. Fu and F. Willaime, Physical Review B: Condensed Matter and Materials Physics **72**, 064117 (2005)
- T. Seletskaia, Y. Ossetsky, R. E. Stoller, and G. M. Stocks, Physical Review B: Condensed Matter and Materials Physics **78**, 134103 (2008)
- L.-X. Liao, X. Zhang, C.-L. Ren, Z.-D. Zhang, H.-F. Huang, G.-H. Ma, and P. Huai, Journal of Applied Physics **127**, 175903 (2020)
- L. Yang, R. Chen, S. Peng, X. Long, Z. Wu, F. Gao, and X. Zu, Science China: Physics, Mechanics, and Astronomy **54**, 827 (2011)
- L. Yang, S. M. Peng, X. G. Long, F. Gao, H. L. Heinisch, R. J. Kurtz, and X. T. Zu, Journal of Physics: Condensed Matter **23**, 035701 (2011)
- X. Gonze, B. Amadon, G. Antonius, F. Arnardi, L. Baguet, J.-M. Beuken, J. Bieder, F. Bottin, J. Bouchet, E. Bousquet, N. Brouwer, F. Bruneval, G. Brunin, T. Cavignac, J.-B. Charraud, W. Chen, M. Côté, S. Cottenier, J. Denier, G. Geneste, P. Ghosez, M. Giantomassi, Y. Gillet, O. Gingras, D. R. Hamann, G. Hautier, X. He, N. Helbig, N. Holzwarth, Y. Jia, F. Jollet, W. Lafargue-Dit-Hauret, K. Lejaeghere, M. A. Marques, A. Martin, C. Martins, H. P. Miranda, F. Naccarato, K. Persson, G. Petretto, V. Planes, Y. Pouillon, S. Prokhorenko, F. Ricci, G.-M. Rignanese, A. H. Romero, M. M. Schmitt, M. Torrent, M. J. van Setten, B. Van Troeye, M. J. Verstraete, G. Zerah, and J. W. Zwanziger, Computer Physics Communications **248**, 107042 (2020)

A. H. Romero, D. C. Allan, B. Amadon, G. Antonius, T. Applencourt, L. Baguet, J. Bieder, F. Bottin, J. Bouchet, E. Bousquet, F. Bruneval, G. Brunin, D. Caliste, M. Côté, J. Denier, C. Dreyer, P. Ghosez, M. Giantomassi, Y. Gillet, O. Gingras, D. R. Hamann, G. Hautier, F. Jollet, G. Jomard, A. Martin, H. P. C. Miranda, F. Naccarato, G. Petretto, N. A. Pike, V. Planes, S. Prokhorenko, T. Rangel, F. Ricci, G.-M. Rignanese, M. Royo, M. Stengel, M. Torrent, M. J. van Setten, B. V. Troeye, M. J. Verstraete, J. Wiktor, J. W. Zwanziger, and X. Gonze, Journal of Chemical Physics **152**, 124102 (2020)

F. Sefta, K. D. Hammond, N. Juslin, and B. D. Wirth, Nuclear Fusion **53**, 073015 (2013).

VITA

Abu Rafi Mohammad Iasir was born in Chattagram (Chittagong), Bangladesh. He received his BSc. in Chemical Engineering from Bangladesh University of Engineering and Technology in 2012. In 2013, he moved to Mizzou and received an M.S. in Nuclear Engineering under the supervision of Dr. Gary Solbrekken in 2015.